Title: Tracing oncogene-driven remodeling of the intestinal stem cell niche

Authors: Min Kyu Yum[1,2,9], Seungmin Han[1,2,9], Juergen Fink[2,10], Szu-Hsien (Sam) Wu[4,10], Catherine Dabrowska[2,3,10], Teodora Trendafilova[2,10], Roxana Mustata[2], Lemonia Chatzeli[1,2], Roberta Azzarelli[2,5], Irina Pshenichnaya[2], Eunmin Lee[6], Frances England[2,3], Jong Kyoung Kim[6], Daniel E. Stange[7], Anna Philpott[2,5], Joo-Hyeon Lee[2,3], Bon-Kyoung Koo[2,4,11*] and Benjamin D. Simons[1,2,8,11*]

Affiliations

[1] Wellcome Trust/Cancer Research UK Gurdon Institute, University of Cambridge, Cambridge CB2 1QN, UK.

[2] Wellcome Trust/Medical Research Council Cambridge Stem Cell Institute, Jeffrey Cheah Biomedical Centre, University of Cambridge, Cambridge CB2 0AW, UK.

[3] Department of Physiology, Development, and Neuroscience, University of Cambridge, Cambridge CB2 3EL, UK.

[4] Institute of Molecular Biotechnology of the Austrian Academy of Sciences (IMBA), Vienna Biocenter (VBC), Dr. Bohr-Gasse 3, 1030 Vienna, Austria.

[5] Department of Oncology, University of Cambridge, Hutchison/MRC Research Centre, Cambridge Biomedical Campus, Cambridge CB2 0XZ, UK.

[6] Department of New Biology, DGIST, Daegu, 42988, Republic of Korea.

[7] Department of Visceral, Thoracic and Vascular Surgery, University Hospital Carl Gustav Carus, Medical Faculty, Technische Universität Dresden, Fetscherstr. 74, 01307 Dresden, Germany.

[8] Department of Applied Mathematics and Theoretical Physics, Centre for Mathematical Sciences, University of Cambridge, Wilberforce Road, Cambridge CB3 0WA, UK.

[9] These authors contributed equally

[10] These authors contributed equally

[11] These authors contributed equally

*To whom correspondence should be addressed.

Benjamin D. Simons (B.D.S.) bds10@cam.ac.uk

Bon-Kyoung Koo (B.-K.K.) bonkyoung.koo@imba.oeaw.ac.at

Abstract

Interactions between tumor cells and the surrounding microenvironment contribute to tumor progression, metastasis and recurrence[1-4]. Although mosaic analyses in *Drosophila* have advanced our understanding of such cellular interactions during tumor initiation[5-8], parallel approaches have remained challenging to engineer in mammalian systems. Here, we present an oncogene-associated, multicolor reporter mouse model, the Red2Onco system, that allows differential tracing of mutant and wild-type cells in the same tissue. Applied to the small intestine, we show that oncogene-expressing mutant crypts alter the cellular organization of neighboring wild-type crypts, driving accelerated clonal drift. Crypts expressing oncogenic KRAS or PI3K secrete BMP ligands that suppress local stem cell activity, while induced changes in PDGFR^{lo} CD81^{+} stromal cells by crypts with oncogenic PI3K alter the Wnt signaling environment. Together, these results show how oncogene-driven paracrine remodeling creates a niche environment that is detrimental to the maintenance of wild-type tissue, promoting field transformation dominated by oncogenic clones.

MAIN

The tumor microenvironment (TME) encompasses a complex, heterogeneous ecosystem comprising mutant and wild-type epithelial cells, as well as other cell types including endothelial, immune and mesenchymal cells[1-3]. From the earliest phase of tumor initiation through to its subsequent progression and transformation, the TME adapts and responds to signals from constituent tumor cells[4]. However, despite extensive evidence for the role of the TME in tumorigenesis, relatively little is known about the response of non-malignant (wild-type) cells to neighboring tumor cells, and the channels of cellular communication through which these effects are mediated.

To date, much of our understanding of the cellular and clonal interactions between epithelial cells has been informed by studies in *Drosophila*, where wild-type cells have been shown to eliminate cells that are less "fit" in a process known as "cell competition"[5,6]. Conversely, tumor cells bearing mutations in genes such as *Myc*, *Ras* or *Apc* can become "super-competitors", eliminating their wild-type neighbors[7,8]. In mammals, increasing emphasis has been placed on cell competition during both normal and tumor development[9]. Oncogenic mutant cells drive aberrant signaling within both mutant cells and the TME[10]. In particular, it has been proposed that mutant cells may affect stromal cells, remodeling the TME and influencing the behavior of neighboring wild-type cells[11]. Indeed, studies in the colon have suggested that transformed intestinal crypts may have profound paracrine effects on neighboring wild-type crypts[12]. Such paracrine signaling effects may occur through direct interaction between mutant and wild-type cells, or may be indirect, mediated by remodeling of the surrounding niche environment (**Fig. 1a**).

Cell labeling strategies have been devised to study changes in epithelial cell fate that arise during the earliest phases of tumor development[13-15]. In studies based on transgenic mouse models, the clonal induction of oncogenic mutations has been coupled to the activation of a fluorescent reporter gene, allowing the fate behavior of mutant cells and their progeny to be traced over time, either from the analysis of fixed samples[16,17] or by using intravital live-imaging strategies[18]. At the same time, studies based on genome editing[19,20] or genetic barcoding[21] have been used to investigate the clonal dynamics of tumor cells in mouse xenograft models of human cancers. Although these methods have provided insight into the factors that drive field cancerization during tumor initiation, it has been difficult to assess how neighboring wild-type cells react to and influence tumor growth. To study the origin and effect of crosstalk between mutant and wild-type cells, and to understand how oncogenic mutations mutually influence cell fate behavior, strategies must be developed that allow wild-type and mutant clones to be studied in parallel within the same native tissue.

To develop such an approach in mouse, previous studies have made use of mosaic genetic labelling, where the interaction between wild-type and mutant clones can be studied at the clonal level. These include mosaic analysis with gain- and loss-of-function, such as Mosaic Analysis with Double Markers (MADM)[22] and inducible, fluorescent and functional genetic mosaic (ifgMosaic) systems[23]. However, the relatively low efficiency of interchromosomal recombination and the challenging allele design present considerable barriers.

Here, we introduce a robust mosaic mammalian genetic model with tunable, inducible fluorescent labeling, based on the fully-characterized and widely used multicolor Confetti reporter system[24] with a simple, single insertion step utilizing the CRISPR/Cas9 endonuclease. By coupling the

expression of a red fluorescent reporter gene to an oncogene of interest, oncogene-expressing (red) clones can be discriminated from wild-type (non-red) neighboring clones. To illustrate the utility of the Red2Onco system, we applied it to study oncogene activation in the lining of the mouse small intestine. Using a combination of clonal analysis, proliferation kinetics and biophysical modeling, we show that the activation of select oncogenes perturbs dynamics and fate behavior both in mutant clones and in wild-type clones in neighboring crypts. Exploiting the design of the Red2Onco system as a platform for comparative single-cell transcriptomics, we further show how oncogene activation drives a wide range of gene expression changes in both mutant (red) and neighboring wild-type (non-red) epithelial cells, as well as in non-epithelial cells in the surrounding environment. While providing insight into the mechanisms, both direct and indirect, that enable oncogene-expressing clones to influence the fate behavior of wild-type stem cells in neighboring crypts, these studies illustrate how the Red2Onco system can be used more widely as a platform to probe oncogene-driven mechanisms of cell-cell communication and cell competition.

RESULTS

Red2Onco system: an oncogene-associated multicolor reporter

To differentially label oncogenic mutant and wild-type cells *in vivo* in the same tissue, we adapted the *Confetti* mouse line[24], based on the *Brainbow-2.1* cassette (**Fig. 1b**), to include an additional cDNA cassette following the *tdimer2 red fluorescent protein* (*RFP*) cDNA in the original *Confetti* allele. In this inducible genetic labeling system, termed Red2Onco, a 2A peptide sequence between *RFP* and an oncogenic cDNA allows co-expression of the oncogene in an RFP-labeled, clone-specific manner. Upon tamoxifen treatment and Cre activation using the *Villin-CreERT2* line, the *R26R-Red2Onco* construct recombines in a stochastic manner to express one of four fluorescent proteins, resulting in mosaic labeling with distinct Confetti colors but where only RFP-labeled clones co-express the oncogenic cDNA (**Fig. 1b,c and Supplementary Video1**).

To illustrate the utility of the Red2Onco system, we developed lines for RFP-specific co-expression of the intracellular domain of *Notch1* (*Red2-Notch1ICD*), $Kras^{G12D}$ (*Red2-*$Kras^{G12D}$) or $PIK3CA^{H1047R}$ (*Red2-*$PIK3CA^{H1047R}$). We first confirmed that the expression of RFP overlapped tightly with gene expression (NOTCH1ICD) or downstream activation (p-ERK for $KRAS^{G12D}$ and p-AKT for $PIK3CA^{H1047R}$) upon Cre-mediated clonal labeling (**Extended Data Fig.1a**). The allele behaved efficiently as a stochastic multicolor Cre-reporter system, as previously reported for the Confetti system[24]. Consistent with studies based on the original *Confetti* construct, yellow (EYFP), red (RFP) and cyan (mCFP) labeling was induced in approximately equal proportions, while green (nuclear GFP) cells were observed only infrequently (**Extended Data Fig.1b**).

To confirm the functionality of the gene perturbations, we further tested whether RFP+ clones showed signs of a corresponding phenotype. Both *Kras*^{G12D} [25-27] and *PIK3CA*^{H1047R} [28,29] have been previously implicated in driving hyperplasia in the small intestinal epithelium. Consistently, we found that RFP+ crypts co-expressing *Kras*^{G12D} or *PIK3CA*^{H1047R} showed evidence of increased cell proliferation compared to control RFP+ crypts from *Confetti* mice (**Extended Data Fig.1c**). It has also been shown that Notch signaling is involved in the regulation of intestinal progenitor cell fate, where it suppresses secretory cell lineage differentiation[30]. Consistently, we found that the expression of *Notch1ICD* blocks secretory cell differentiation in RFP+ clones (**Extended Data Fig.1d,e**). Together, these results indicate that the chosen genes are expressed and functional in RFP-labeled clones of the Red2Onco system.

We then used several inducible Cre driver mouse lines, including *R26R-CreERT2*, *Sftpc-CreERT2* and *Krt5-CreERT2*, to confirm the viability of the Red2Onco system in various organs, both in the context of adult tissue maintenance and development. Consistent with previous reports, we found that expression of *Kras*^{G12D} induced clonal outgrowth in the skin interfollicular epidermis[31], and lung epithelium[32] (**Extended Data Fig.1f**). Moreover, expression of *Notch1ICD* also induced rapid expansion of mutant clones in the stomach corpus glands[33] (**Extended Data Fig.1f**), while activation of the Akt pathway by *PIK3CA*^{H1047R} expression led to an initial survival advantage for mutant clones in the esophageal squamous epithelium[34] (**Extended Data Fig.1f**). Finally, embryonic activation of KRAS^{G12D} led to large-scale clonal outgrowth and acinar cell expansion during embryonic pancreas development[35] (**Extended Data Fig.1g**). Notably, the Red2Onco system provides a set of *Confetti* variant alleles that allow cross-comparison and functional characterization of normal and mutant clones in the same animal, as detailed below.

Mutations drive non-neutral clone expansion in the mouse intestinal crypt

By design, the Red2Onco system is tailored to comparative analyses: when induced at low (clonal) induction frequency, the system allows comparison of the dynamics of "isolated" mutant and wild-type clones, where the latter are distant from the former. In this case, wild-type clones serve as an optimal internal control. More importantly, if there were crosstalk acting between mutant and wild-type cells, any bias in fate behavior could be detected by comparing the properties (size, gene expression pattern and cellular organization) of wild-type (non-red) clones with respect to their distance from mutant (red) clones (**Extended Data Fig. 1h**). Moreover, since the Red2Onco system is based on the original design of the *Confetti* allele, the *R26R-Confetti* line serves as a further control for wild-type clones for any *Red2Onco* alleles, so providing a vehicle to assess potential systemic effects following oncogene activation. Therefore, to test the utility and power of the Red2Onco system as a means to detect cellular crosstalk, we turned to the quantitative analysis of mutant and wild-type clones in the gut, placing emphasis on the small intestinal epithelium.

In mammals, the small intestine is composed of glands – crypts of Lieberkühn – that form invaginations into the stromal tissue, as well as villi structures that protrude into the gut lumen[36]. Crypts and villi are lined by a columnar epithelium composed of multipotent stem cells, lineage-restricted progenitor cells and specialized populations of terminally differentiated absorptive cells and secretory lineages including goblet cells, enteroendocrine cells, Paneth cells and other minor populations. Previously, lineage tracing studies in the mouse have associated stem cell function with a minority population of crypt-base columnar (CBC) cells that lie interspersed among large,

secretory Paneth cells[37]. As intestinal stem cells (ISCs) divide, neighbors become displaced from the niche and enter into a differentiation program. Through this process of continuous ISC loss by differentiation and replacement, ISC-derived clones stochastically expand and contract, leading to neutral drift of clones around the circumference of the crypt until the clone is lost or the crypt becomes monoclonally fixed. Through the quantitative statistical analysis of clone sizes, static lineage tracing and intravital imaging studies have defined the functional identity and fate behavior of ISCs both in homeostasis[18,38,39] and following oncogene activation[16,17].

Previously, it has been shown that, alongside WNT, mutations in the RAS-MAPK and PI3K-AKT pathways represent key drivers of colorectal cancer[14,40,41]. In contrast to WNT, activation of RAS signaling does not lead to obvious changes in tissue architecture, leading to the assumption that mutations in Wnt signaling are likely to represent the first oncogenic hit. However, with KRAS mutations found recently to be abundant in ageing human intestinal epithelium[11,42], as well as in patients with Crohn's disease[43-45], this raises the question of whether mutations in RAS-MAPK or PI3K-AKT signaling could function as drivers of early mutant clone expansion.

To chart the clonal dynamics of labeled mutant and wild-type cells, clones induced using the Red2Onco system were visualized and quantified. Based on the reported behavior of ISCs and their progeny under normal conditions, clones were quantified according to their circumferential span at the "+4 row position", representing the border of the niche domain. Statistical analysis of the detailed cellular arrangements of clones at the crypt base confirmed that such measures were representative of ISC clone sizes (**Extended Data Fig. 2a-d**). To investigate the effect of altered gene expression on intra-crypt clonal competition, we first performed lineage tracing with *Villin-*

CreERT2; *R26R-Red2Onco* mice induced at clonal induction frequency, using a low dosage of tamoxifen (0.2 mg/20 g body weight). At this induction frequency, on average, each crypt plays host to less than one labeled ISC-derived clone (**Extended Data Fig. 2e**).

To assess the effect of the mutations, we compared the clone size distributions of isolated mutant (red) and wild-type (non-red) clones over a 21-day time course in the small intestine (**Extended Data Fig. 2f**). Within just 7 days post-induction, mutant clones already showed a clear difference to their wild-type counterparts, with evidence of biased drift for all three mutants (**Extended Data Fig. 2g,h**). Although both mutant and wild-type clones showed a characteristically broad distribution of sizes, both the average size of mutant clones and the frequency of monoclonal (fixed) crypts increased more steeply than for wild-type (**Extended Data Fig. 2i,j**, see **Supplementary Table 1** for statistical analyses). These findings echoed the results of previous studies of the mouse small intestine based on the clonal activation of KRAS using a conventional reporter construct[16,17]. A quantitative comparison of isolated, wild-type (non-red) clones in the Red2Onco system with (red and non-red) clones from the *Confetti* control (**Extended Data Fig. 3a-c**) indicated that there were no systemic effects on clonal dynamics due to the modified *Confetti* construct.

To resolve the dynamics of mutant clone expansion, we turned to an existing stochastic modeling-based scheme whose validity has been tested extensively in previous studies[38,39]. Within this framework, the dynamics of ISC-derived clones are modeled as a one-dimensional system of N "effective" ISCs that line the crypt circumference at the base. ISC loss (at rate λ) is correlated with the duplication of a neighbor, leading to neutral drift of clone size until the clone is altogether lost from the base or the crypt becomes fixed in one Confetti color. Intravital live-imaging studies show

that this model represents a caricature of a more complex dynamics, with ISCs moving reversibly between "states" biased for renewal or primed towards differentiation according to their position within the niche[18]. However, once clones span the axis of the crypt in a representative manner, their subsequent lateral dynamics around the crypt circumference become indistinguishable from the minimal one-dimensional scheme (see **Supplementary Theory**). Applied to the *Confetti* control, taking from the literature[39] an effective stem cell number for the proximal small intestine of *N=5*, a quantitative fit of the model to the clone data obtains a loss-replacement rate of $\lambda = 0.9$ per week, similar to previous work (**Extended Data Fig. 3a**)[39].

Following oncogene expression, mutant cells may experience a survival advantage over their neighbors, leading to a biased drift of clones around the base. Such a bias may be "active", with mutant clones promoting the differentiation and loss of wild-type neighbors, or it may be "passive", with an increase in proliferation or "sensitivity" to niche factors enabling cells to outcompete their wild-type neighbors. In either case, the resulting clonal dynamics can be mapped to a modified one-dimensional model in which the ISC loss-replacement rate acquires a bias $0 \leq \delta \leq 1$, with mutant ISCs replacing their wild-type neighbors at rate $\lambda(1+\delta)$, while wild-type ISCs replace their mutant neighbors at rate $\lambda(1-\delta)$. Within this framework, taking an effective stem cell number of *N=5*, we find that the biased drift model predicts accurately the time evolution of the clone size distributions with λ = 2.4 per week and δ = 0.71 for $Kras^{G12D}$ (similar to that reported in previous studies[16,17]), λ = 1.9 per week and δ = 0.64 for $PIK3CA^{H1047R}$, and λ = 1.1 per week and δ = 0.36 for *Notch1ICD*. Notably, $Kras^{G12D}$ and $PIK3CA^{H1047R}$ mutant ISCs experience a substantial survival advantage over wild-type neighbors, while for *Notch1ICD* the survival advantage is comparatively small (**Extended Data Fig. 3d-f**).

Active competition through apoptotic elimination of less-fit cells by surrounding cells is well-documented in *Drosophila* and the mouse epiblast[6]. However, immunodetection of cleaved caspase-3 in the intestinal crypts of *R26R-Red2Onco* mice showed no evidence of increased apoptosis either in mutant cells or their surrounding non-labeled neighbors (**Extended Data Fig. 3g**), suggesting that active competition does not operate in the intestinal models studied here. By contrast, a 2-hour EdU pulse applied to *Villin-CreERT2*; *R26R-Red2Onco* mice 2 weeks after tamoxifen injection showed an increased number of EdU+ CBCs at the crypt base in mutant clones from all three *Red2Onco* mice as compared to the *Confetti* control (**Extended Data Fig. 3h,i**). Together, these results suggest that an increase in proliferation rate may confer a passive advantage, allowing mutant cells to outcompete their wild-type neighbors and driving biased clonal drift.

Oncogene-induced short-range perturbation of neighboring wild-type crypts

Having established the effect of genetic perturbations on the clonal dynamics of mutant ISCs, we then exploited the design of the Red2Onco system to study the potential effect of mutant clones on the dynamics and fate behavior of wild-type clones in neighboring crypts. We first performed lineage tracing with *Villin-CreERT2*; *R26R-Red2Onco* mice induced at near-clonal induction frequency using a medium dosage of tamoxifen (2 mg/20 g body weight). At this level of induction, more than 30% of the crypts contained labeled cells. Thus, if there were any paracrine effects of mutant cells on wild-type clones, they should be easily detected by analyzing the abundance of fixed wild-type crypts (i.e. monoclonally labeled in non-red Confetti colors). Unexpectedly, we found that the frequency of fixed wild-type crypts in *Red2-Kras*^{G12D} and *Red2-PIK3CA*^{H1047R} mice was increased compared to wild-type crypts in *R26R-Confetti* control animals, whereas the

frequency of fixed wild-type crypts from *Red2-Notch1ICD* mice remained similar to controls (**Extended Data Fig. 4a,b**). These results suggested that mutant cells in *Red2-Kras*^{G12D} and *Red2-PIK3CA*^{H1047R} crypts mediate changes in the clonal dynamics of wild-type cells in neighboring crypts.

To further dissect this phenotype, we used a clonal dosage of tamoxifen (0.2 mg/20 g body weight) to compare the dynamics of wild-type (non-red) clones in crypts either neighboring (proximate) or remote (3 crypt diameters or more apart) from crypts containing a mutant (red) clone (**Fig. 2a**). Strikingly, we found that when proximate to mutant crypts, wild-type clones from *Red2-Kras*^{G12D} and *Red2-PIK3CA*^{H1047R} mice showed evidence of accelerated clonal drift, greatly exceeding that of either remote wild-type crypts or clones quantified from *Confetti* controls (**Fig. 2b,c**). These qualitative observations were corroborated by clone size quantification, which showed a significant increase in the corresponding average clone size and fixation rate (**Fig. 2d,e**, see **Supplementary Table 1** for statistical analyses). These results suggest that following oncogene activation, direct and/or indirect signals from mutant clones significantly perturb the clonal dynamics of wild-type cells in neighboring crypts.

Given the apparent differences in the drift dynamics of clones in wild-type crypts neighboring mutant crypts, we performed a more detailed characterization of their dynamics. We partitioned the clonal data from wild-type crypts bordering mutant crypts into two classes, “inner” and “outer”, depending on whether the clone was positioned towards or further from the neighboring mutant clone-containing crypt (**Extended Data Fig. 4c**). For inner clones, we considered their geometric center (based on the row +4 assignment) to be located closer to the mutant crypt than to their crypt

center, while for outer clones it was the opposite. Notably, the measured clone size distributions (and corresponding averages) of both inner and outer wild-type clones were found to be comparable, suggesting that accelerated clone dynamics took place within the context of neutral competition (**Extended Data Fig. 4d,e**, see **Supplementary Table 1** for statistical analyses).

To make a further quantitative assessment of the dynamics of WT clones in crypts neighboring mutant crypts we noted that, prior to fixation, neutral clone dynamics is predicted to enter into a scaling regime in which the chance of finding a clone of angular size θ larger than some multiple of the average $\langle\theta\rangle$ at a time, t, post-induction is given by $C(\theta,t) = f(\theta/\langle\theta\rangle)$, where the scaling function $f(x) = e^{-\pi x^2/4}$ and $\langle\theta\rangle/360^{\circ} = \sqrt{\pi\lambda t/N^2}$ depends only on the composite "drift rate" $\Lambda \equiv \lambda/N^2$ (see Supplementary Theory)[38]. This provides an opportunity to make an unbiased assessment both of the neutrality and the rate of accelerated clonal drift in the neighboring crypts. Comparison of the cumulative clone size distribution showed convergence of the clone size distribution onto the predicted scaling form in both Confetti control and mutant conditions (**Fig. 3a**). Further, from a fit to the average clone size $\langle\theta\rangle$, we found a drift rate Λ that was approximately 1.9 times larger in the two mutant conditions compared to the Confetti control (**Fig. 3b**, **Extended Data Fig. 4f** and Supplementary Theory).

To resolve the origin of accelerated drift, we considered three hypotheses: (a) the rate of ISC loss and replacement, λ, is increased; (b) the effective ISC number, N, is decreased; and (c) both of these effects occur (**Fig. 3c**). We first crossed *Lgr5-EGFP-IRES-CreERT2* (Lgr5-EGFP reporter) mice with *R26R-Red2Onco* mice, and sought independent evidence for whether the wild-type ISC

loss-replacement rate is influenced by proximity to mutant crypts. Notably, measurements of the ISC proliferation rate based on EdU incorporation within EGFP+ ISC showed comparable values (**Fig. 3d,e**), independent of the proximity of wild-type crypts to mutant crypts, consistent with an unchanged rate of ISC loss-replacement.

We then estimated the total number of ISCs based on *Lgr5* expression. Two weeks after tamoxifen treatment, when the majority of mutant crypts were already fixed, we found that the number of EGFP+ cells was decreased by 20% in wild-type crypts neighboring mutant crypts (**Fig. 3f,g**). Similar results were found based on the expression of *Olfm4*, another marker of ISCs (**Extended Data Fig. 5a**). Together, these findings suggest that the near two-fold acceleration in drift rate, $\Lambda \equiv \lambda/N^2$, is associated with around a 25% reduction in the effective stem cell number of crypts neighboring crypts mutant for $Kras^{G12D}$ or $PIK3CA^{H1047R}$.

Alongside a reduction in the number of Lgr5+ cells, we also found that the presence of fixed mutant crypts reduces the physical size (indexed by the lateral cross-sectional area) of neighboring wild-type crypts when compared to those further away (**Extended Data Fig. 5b-d**). We therefore questioned whether this reduction in size might be mediated by mechanical influences. In common with previous reports[25-27], we found that crypts expressing $Kras^{G12D}$ are expanded in size, suggesting that resulting mechanical stresses may deform and thereby diminish the size of neighboring crypts. As a possible indicator of mechanical stress, we scored the circularity of wild-type crypts as a function of the distance from mutant crypts (**Extended Data Fig. 5e,f**). However, we found that wild-type crypts neighboring mutant crypts were geometrically and statistically indistinguishable from those that were remote.

Next, we challenged our near-clonal induction (2 mg/20 g body weight) samples to further test whether the perturbation of wild-type clones by neighboring mutant crypts is mediated by paracrine signaling. We hypothesized that, if the effect is mediated by paracrine factors from mutant cells, it should scale with the multiplicity of neighboring mutant crypts (**Extended Data Fig. 5g**). Intriguingly, we found that, when proximate to multiple mutant crypts, wild-type clones from *Red2-Kras*^{G12D} and *Red2-PIK3CA*^{H1047R} mice showed evidence of both an increased rate of clonal drift and crypt fixation as compared to clones bordering just a single mutant crypt (**Extended Data Fig. 5h-j**). We then examined whether the number of ISCs and the physical size of wild-type crypts were also affected by the multiplicity of neighboring mutant crypts. Notably, both measures were found to be smaller than that of wild-type clones neighboring a single mutant crypt (**Extended Data Fig. 5k-m**). These results support the role of paracrine signaling in mediating the crosstalk between mutant and wild-type crypts.

Lastly, we questioned whether mutation-induced changes promote accelerated mutant field expansion. Notably, when induced at higher frequency (2 mg/20 g body weight), we found that, in contrast to *Confetti* and *Red2-Notch1ICD* conditions, the fraction of WT (non-red) crypts steadily diminished in *Red2-Kras*^{G12D} and *Red2-PIK3CA*^{H1047R} mice at the expense of mutant (red) crypts (**Fig. 3h,i**). To explore the basis of such field change, we used the abundance of "cojoined" crypts (see **Fig. 3j**) to estimate the relative frequency of crypt fission and fusion. Following Bruens et al.[46], we reasoned that, when studied at clonal density, cojoined crypts bearing the same Confetti color were likely to be in the process of fissioning, while those in which only one half of the crypt was labelled were likely to be undergoing crypt fusion. Based on this assessment, we found that

crypts mutant for *Kras*^{G12D} and *PIK3CA*^{H1047R} showed elevated (2-3 fold) rates of fission and fusion as compared to the *Confetti* control (**Fig. 3k**), suggesting that the deleterious effects of the mutant on neighboring wild-type crypts may contribute towards driving field transformation.

Comparative single-cell transcriptomic analysis identifies oncogene-driven changes in signalling pathways

Although clonal analysis using the Red2Onco system provides functional evidence for the existence of cellular crosstalk, it does not reveal the molecular pathways or cell types that could mediate such interaction. Indeed, such effects could involve direct signaling between mutant and wild-type epithelial cells communicated through the exchange of paracrine factors and/or indirect signaling through alterations to the shared stromal niche. To define the mechanisms that mediate cellular crosstalk, we exploited the design of the Red2Onco system for comparative single-cell transcriptomics. In particular, the expression of distinct fluorescent reporters allows mutant and wild-type epithelial cells to be profiled in parallel from the same tissue sample using fluorescence-activated cell sorting (FACS). Moreover, the Red2Onco system also allows the analysis of transcriptional changes in the shared stromal niche and immune system, providing a viable strategy to study potential pathways for cellular crosstalk in a complex tissue environment (**Fig. 4a**).

To collect mutant and wild-type cells from neighboring crypts, we developed a strategy based on mosaic labeling. In this approach, *Villin-CreERT2*; *R26R-Red2Onco* mice (*Kras*^{G12D} or *PIK3CA*^{H1047R} mutation) were induced using a high dosage of tamoxifen (4 mg/20 g body weight). The majority of crypts (>56% for *Red2-Kras*^{G12D} and >54% for *Red2-PIK3CA*^{H1047R}) were found to be monoclonal for mutant oncogene expression by 2 weeks post-induction at this level, while

almost all of the remaining (wild-type) crypts, 94% for *Red2-Kras*^{G12D} and 92% for *Red2-PIK3CA*^{H1047R}, neighbored mutant crypts. Following the dissociation of intestinal tissue, individual mutant (RFP) and wild-type (YFP) epithelial cells were then sorted by FACS (**Extended Data Fig. 6a**, R5 and R6 gates) and profiled alongside neighboring stromal tissue (**Extended Data Fig. 6a**, R7 and R8 gates) using the single-cell 10X Genomics platform. By combining these results with single-cell RNA-seq data for cells collected from control *Confetti* animals, mutation-driven differential changes in gene expression could be resolved in both epithelial (RFP+ mutant cells and YFP+ wild-type cells in neighboring crypts), stromal and immune cells (**Fig. 4a and see Methods**). The biological replicates for each condition (2 for *Confetti*, 3 for *Red2-Kras*^{G12D} and 2 for *Red2-PIK3CA*^{H1047R} models) overlapped well with each other, implying a high level of reproducibility between replicates and providing confidence in the statistical reliability of our analysis (**Extended Data Fig. 6b**).

Initially, epithelial cells from the three different models – *Red2-Kras*^{G12D}, *Red2-PIK3CA*^{H1047R} and the *Confetti* control – were clustered based on expression patterns of marker genes for distinct cell types (**Fig. 4b, Extended Data Fig. 6c,d and Supplementary Table 2**). All major epithelial cell types were detected in ratios comparable to those in previous reports[47-51]. Despite transcriptional changes induced by oncogene expression, all mutant and wild-type cells from the three conditions overlapped within distinct cell clusters without any batch correction, confirming that batch effects between different samples were not significant (**Fig. 4c and see Methods**). Importantly, the overlap of mutant and wild-type cells within the same cluster groups provided the basis for comparative analysis between different conditions.

As a representative measure to estimate broad epithelial changes, we first examined the relative proportions of each cell type for mutant and wild-type cells in *Red2-Kras*^{G12D} and *Red2-PIK3CA*^{H1047R} mice compared to the *Confetti* control, enabling the potential influence of oncogene activation on cell lineage specification to be determined. Indeed, significant changes in proportions were observed in all mutant (RFP+) cell types from *Red2-Kras*^{G12D} and *Red2-PIK3CA*^{H1047R} mice compared to the *Confetti* control (**Fig. 4d and Extended Data Fig. 6e**). Notably, the proportion of mutant (RFP+) Lgr5+ stem cells in both *Red2-Kras*^{G12D} and *Red2-PIK3CA*^{H1047R} mice was significantly decreased (**Fig. 4d**). By contrast, the proportion of mutant (RFP+) goblet cells was increased in both *Red2-Kras*^{G12D} and *Red2-PIK3CA*^{H1047R} mice compared to the *Confetti* control, consistent with a previous report[26]. In *Red2-PIK3CA*^{H1047R} animals, an increase in the proportion of mutant (RFP+) enterocytes was also observed. Wild-type (YFP+) cells in *Red2-Kras*^{G12D} and *Red2-PIK3CA*^{H1047R} animals showed changes in the proportions of specific cell types including stem cells, enterocyte progenitor cells, goblet cells and enterocytes (**Fig. 4e and Extended Data Fig. 6f**). Of note, as with the mutant (RFP+) cells, the wild-type (YFP+) population contained a lower proportion of stem cells and transit-amplifying (TA) cells in both *Red2-Kras*^{G12D} and *Red2-PIK3CA*^{H1047R} animals (**Fig. 4e**), which was consistent with the reduced number of effective ISCs predicted by the biophysical modeling of the clonal data (**Fig. 3a,b**). The reduction in the Lgr5+ stem cell fraction in both mutant (RFP+) cells and wild-type (YFP+) cells was further confirmed by immunohistochemistry (**Extended Data Fig. 6g-i**) and FACS (**Extended Data Fig. 6j,k**). Interestingly, while both mutant and neighboring wild-type crypts show a fractional decrease of stem cell number, the absolute number of mutant stem cells in both *Red2-Kras*^{G12D} and *Red2-PIK3CA*^{H1047R} mice remained comparable to the *Confetti* and remote wild-type controls (**Extended Data Fig. 6h,i**).

We then questioned whether changes in the fraction of stem and progenitor cells in both *Red2Onco* models were accompanied by changes in their molecular characteristics. We first defined lineage specific genes (2497 genes for Enterocyte, 4660 genes for enteroendocrine cells, 4941 genes for goblet cells, 2494 genes for Paneth cells, 3416 genes for Tuft cells) as molecular signatures of fate priming, using single-cell RNA-seq data from a previous study[48] (**Supplementary Table 3**). We then calculated the priming score towards differentiated sub-lineages for individual wild-type (YFP+) and mutant (RFP+) stem cells and TA cells as immediate progenitors in the *Red2Onco* and *Confetti* animals (**see Methods**). Wild-type (YFP+) stem and TA cells in *Red2-Kras*^{G12D} and *Red2-PIK3CA*^{H1047R} mice showed an enhanced degree of differentiation towards the secretory (**Fig. 4f, Supplementary Table 3**) and absorptive lineages (**Fig. 4g**) compared to those in *Confetti* animals. Furthermore, this same pattern was also observed in mutant (RFP+) stem and TA cells in both *Red2Onco* models (**Extended Data Fig. 7a,b and Supplementary Table 3**). With realtime qPCR analysis, we confirmed that the differentiation lineage markers for goblet cells, *Clca1*, and absorptive cells, *Fabp1* and *Alpi*, were elevated in both mutant (RFP+) and wild-type (YFP+) cells from *Red2-Kras*^{G12D} and *Red2-PIK3CA*^{H1047R} mice, compared to those in the *Confetti* control (**Extended Data Fig. 7c**). To find experimental support for biased differentiation of stem and progenitor cells in wild-type crypts neighboring mutant crypts in *Red2-Kras*^{G12D} and *Red2-PIK3CA*^{H1047R} animals, we first estimated directly the number of goblet cells based on Muc2 expression by immunostaining. Two weeks after tamoxifen treatment (2mg/ 20g body weight, semi-clonal dosage), when the majority of mutant crypts were fixed, we found that the number of Muc2+ cells was increased in wild-type crypts neighboring mutant crypts in *Red2-Kras*^{G12D} mice, but not in *Red2-PIK3CA*^{H1047R} mice, as compared to that of the *Confetti* and remote wild-type

control (**Extended Data Fig. 7d,e**). We then conducted RNA *in situ* hybridization with *Fabp1*, a marker for enterocyte differentiation (**Extended Data Fig. 7f**). We found that *Fabp1* expression is more abundant in the lower portion of the crypt, not only in crypts expressing mutant PI3K, but also in neighboring wild-type crypts (**Extended Data Fig. 7g-j**). These results suggest the priming of neighboring wild-type and mutant stem cells toward differentiation as a potential driver of the reduced stem cell fraction in mutant crypts and their neighboring wild-type crypts in both *Red2-Kras*^{G12D} and *Red2-PIK3CA*^{H1047R} mice.

To further probe the potential molecular mechanisms underlying biased differentiation triggered by oncogene-expressing clones, we first assessed the activities of major pathways that are known to regulate ISC potential and sub-lineage specification including the WNT, BMP and NOTCH pathways[2,36]. We defined associated gene sets based on the literature and the MSigDB data base (**see Supplementary Table 3 and Methods**) and performed gene set enrichment analysis on both mutant and wild-type epithelial cells from the *Red2Onco* models compared to epithelial cells from the *Confetti* control (**see Methods**) (**Fig. 4h,i and Extended Data Fig. 7k,l**). These data revealed higher BMP signaling activity in both mutant and wild-type cells of *Red2-Kras*^{G12D} and *Red2-PIK3CA*^{H1047R} animals compared to the *Confetti* control (left panels of **Fig. 4h,i**). Lower WNT signaling activity was observed in both mutant and wild-type cells of *Red2-PIK3CA*^{H1047R}, but not *Red2-Kras*^{G12D}, animals compared to the *Confetti* control (right panels of **Fig. 4h,i**). By contrast, NOTCH signaling activity was reduced in mutant cells, but not in wild-type cells, of both *Red2-Kras*^{G12D} and *Red2-PIK3CA*^{H1047R} animals (**Extended Data Fig. 7k,l**). Based on these findings, we focused on the changes in BMP and WNT signaling to trace the basis of inter-crypt cellular crosstalk.

Mutant clones drive niche remodelling

Single-cell transcriptomic analysis of the epithelial cell population showed that not only oncogene-expressing clones but also wild-type stem cells in neighboring crypts have an altered stem cell expression profile, with characteristic changes in BMP and WNT pathways depending on the oncogene. Based on this observation, we examined direct (epithelial-to-epithelial) and indirect (*via* mesenchymal or immune cell) routes of communication that could potentially affect BMP and WNT pathways in the *Red2Onco* mice. In particular, we considered not only epithelial cells, but also non-epithelial cells including mesenchymal and immune cells from our single-cell transcriptome data (**Fig. 4a**). Mesenchymal and immune cells from the *Confetti* control, *Red2-Kras*^{G12D} and *Red2-PIK3CA*^{H1047R} animals at the 2-week time-point were segregated into 7 clusters, respectively, based on their unique expression signatures (**Fig. 5a,b and Extended Data Fig. 7m,n and Supplementary Table 4**). Three clusters (labeled as STC, short for "stromal cell") show marked expression of well-known secreted factors for intestinal stromal cells (**Extended Data Fig. 7o**)[52,53]. Notably, *Bmp4* was highly expressed in STC1, whereas STC2 expressed WNT pathway-modulating factors such as *Wnt5a* and *Rspo3*, as well as the BMP antagonist, *Grem1* (**Extended Data Fig. 7o**). These results suggested a possible involvement of STC1 and STC2 in the regulation of the BMP and WNT pathways.

We then searched for expression changes occurring in mutant epithelial cells, mesenchymal cells or immune cells in secreted factors that can modulate the BMP and WNT pathways. From the list of secreted factors (**Supplementary Table 5**), we noticed an increase in the expression of BMP pathway agonists, such as *Bmp2* and *Bmp7*, found mainly in mutant secretory epithelial cells (e.g.

Paneth, goblet and tuft cells) in *Red2-Kras*^{G12D} and *Red2-PIK3CA*^{H1047R} mice compared to the *Confetti* control (**Fig. 5c**). At the same time, we also detected an increase in the expression of WNT pathway antagonists, such as *Sfrp2* and *Sfrp4*, in the STC2 population, as well as a decrease in the expression of WNT pathway agonists, such as *Rspo3*, in STC2 in the *Red2-PIK3CA*^{H1047R} model (**Fig. 5d**). We also checked that receptors upstream of the BMP or WNT pathway were expressed in mutant and wild-type ISCs in all models (**Extended Data Fig. 8a,b**). The difference between *Red2-Kras*^{G12D} and *Red2-PIK3CA*^{H1047R} animals in terms of WNT pathway modulation may explain the cell fate bias toward the secretory lineage in *Red2-Kras*^{G12D} mice and the absorptive lineage in *Red2-PIK3CA*^{H1047R} mice (**Fig. 4d-g and Extended Data Fig. 7a,b**), consistent with previous findings[36,54].

The changes in ligand expression in mesenchymal cells raised the possibility that the niche environment may become altered upon oncogene activation. Thus, to gain an overview of environmental changes, we examined the composition of cell types in the mesenchymal and immune populations (**Extended Data Fig. 8c,d**). Among the mesenchymal cell populations, we could find evidence for a statistically significant change in the proportions of STC2, myofibroblasts, interstitial cells, endothelial cells and glial cells in *Red2-Kras*^{G12D} and *Red2-PIK3CA*^{H1047R} mice (**Extended Data Fig. 8c**). Moreover, among immune cell populations, there was also evidence for a statistically significant change in the proportions of dendritic cells, monocytes, plasma cells and T cells (**Extended Data Fig. 8d**). In addition to the compositional changes, we further examined whether mesenchymal and immune cells underwent transcriptional alteration. Gene expression changes in mesenchymal and immune cells were quantified by two independent methods (**see Methods**). Both methods indicated that the stromal STC2 as well as

monocyte population in the *Red2-PIK3CA*^{H1047R} model experienced statistically significant alterations compared to other cell types (**Fig. 5e,f and Extended Data Fig. 8e-g**). We also found that the STC2 population in the *Red2-PIK3CA*^{H1047R} model not only expresses WNT pathway antagonists, including *Sfrp2* and *Sfrp4* (**Fig. 5d**), but also shows an increase in transcripts for genes known to reorganize the extracellular matrix, such as *Fn1*, *Mmp2* and collagens (*Col6a2* and *Col5a2*) (**Fig. 5g,h and Supplementary Table 4**). From monocytes, we did not observe changes of WNT and BMP agonists or antagonists (**Supplementary Table 4**).

Together, these results reveal pathways for cellular crosstalk between mutant and wild-type cells in neighboring crypts (**Fig. 5i**). Epithelial oncogene expression of either mutant KRAS or PI3K stimulates an increase in BMP signaling pathway, with PI3K activation also resulting in an additional decrease in WNT signaling pathway. These common and distinct niche changes driven by oncogene activation contribute to a reduction in the ISC fraction and increased differentiation, with a fate bias toward the secretory lineage in *Red2-Kras*^{G12D} mice and the absorptive lineage in *Red2-PIK3CA*^{H1047R} mice.

Functional validation of pathways involved in oncogene-driven niche remodeling

To find further experimental support for the conclusions from our scRNA-seq analysis, we first sought direct evidence for BMP and WNT pathway activity in mutant crypts and their neighboring wild-type crypts in *Red2-Kras*^{G12D} and *Red2-PIK3CA*^{H1047R} mice. To this end, we first performed *in situ* hybridizations for *Axin2* and *Id1*, which are the most well-accepted downstream target genes of WNT and BMP pathways, respectively (**Fig. 6a-d**). As expected from our single-cell analysis, we observed decreased expression of *Axin2* in mutant crypts and neighbouring wild-type crypts

543 only in *Red2-PIK3CA*^{H1047R} mice, but not in *Red2-Kras*^{G12D} mice (**Fig. 6a,b**). By contrast, again
544 as predicted, *Id1* expression was found to be increased in mutant crypts and neighbouring wild-
545 type crypts in both *Red2-Kras*^{G12D} and *Red2-PIK3CA*^{H1047R} mice compared to that of the *Confetti*
546 control (**Fig. 6c,d**). Furthermore, these results were consistent with realtime qPCR analysis
547 (**Extended Data Fig. 8h,i**), confirming that WNT activity was decreased only in cells from *Red2-*
548 *PIK3CA*^{H1047R} mice, while BMP activity was increased in cells from both *Red2-Kras*^{G12D} and *Red2-*
549 *PIK3CA*^{H1047R} mice.
550
551 We then sought to challenge further our hypothesis that mutant epithelial cells from both *Red2-*
552 *Kras*^{G12D} and *Red2-PIK3CA*^{H1047R} mice are the source of the BMP ligands, BMP2 and BMP7,
553 while STC2 cells in *Red2-PIK3CA*^{H1047R} mice function as WNT-inhibitory niche cells by secreting
554 more WNT inhibitors, SFRP2 and SFRP4 and less WNT agonist, RSPO3. Previous reports have
555 shown that BMP2 is potent BMP ligand mainly secreted from intestinal epithelial cells[55-57].
556 Consistent with the scRNA-seq analysis (**Fig. 5c**), using *in situ* hybridisation, we observed
557 increased expression of *Bmp2* in mutant crypt epithelial cells of *Red2-Kras*^{G12D} and *Red2-*
558 *PIK3CA*^{H1047R} mice, compared to wild-type epithelial cells of *Red2-Kras*^{G12D} and *Red2-*
559 *PIK3CA*^{H1047R} mice, as well as the *Confetti* control (**Fig. 6e,f**). In addition, our realtime qPCR
560 analysis confirmed increased mRNA expression of *Bmp2* and *Bmp7* only in mutant epithelial cells
561 of both Red2 systems compared to the *Confetti* control (**Extended Data Fig. 8j**).
562
563 It has been proposed that oncogenic mutant cells still show a striking dependency on the niche
564 factors if they are not direct upstream ligands of the signalling activated by the mutation[58-60]. When
565 we established mutant (RFP+) organoids using sorted RFP+ cells, we not only observed an

increased expression of *Bmp2* and *Bmp7* mRNA (**Extended Data Fig. 8k**), but also that mutant organoids were much more sensitive to Noggin withdrawal (**Extended Data Fig. 8l**), suggesting the secreted BMP ligands may act on mutant cells in an autocrine manner. To further validate the activity of BMP ligands secreted from mutant epithelial cells, we generated conditioned media by culturing mutant organoids in Noggin-deprived medium (ER) (**Extended Data Fig. 8m**). When we treated the conditioned media to wild-type organoids, expression of BMP target genes such as *Id1* increased, which could be blocked by BMP type 1 receptor inhibitor, LDN193189 (**Extended Data Fig. 8n**). These results suggest that BMP ligands, secreted from mutant epithelial cells, are indeed functional. Nevertheless, from our scRNA-seq data, we also observed expression changes of Bmp ligands in the mesenchymal cells (**Supplementary Table 5**). Together, these results show that mutant epithelial BMP ligands, potentially together with mesenchymal BMP ligands, influence the crypt microenvironment.

Recently, PDGFRA^{lo} CD81+ stromal cells were identified as an important source of R-spondin and Gremlin1, which are a WNT agonist and a BMP antagonist, respectively[61]. We also found that the STC2 population, which showed high Wnt agonist (*Rspo3*) expression (**Extended Data Fig. 7o**), also expressed high levels of *Grem1* as well as *Cd81* compared to other mesenchymal cells (**Fig. 6g**). Regarding altered expression of secreted WNT modulators (*Sfrp2*, *Sfrp4* and *Rspo3*) in *Red2-PIK3CA*^{H1047R} mice, we conducted multiplexed *in situ* hybridisation of the STC2 population to validate our hypothesis on its contribution to reduced WNT activity in *Red2-PIK3CA*^{H1047R} mice. As shown by McCarthy et al., we could locate STC2 cells adjacent to the intestinal crypt base by using *Grem1* or *Cd81* as a marker (**Fig. 6h and Extended Data Fig. 9a**). We also observed that the expression of *Sfrp2* was increased in *Grem1*+ STC2 cells, located in the base region between

wild-type and mutant crypts of *Red2-PIK3CA*^{H1047R} mice, as compared to that of *Red2-Kras*^{G12D} mice and the *Confetti* control (**Extended Data Fig. 9a,b**). Consistent with the predicted changes in STC2 (**Fig. 5d**), when we checked expression of *Rspo3*, a critical WNT agonist in the crypt microenvironment, we found levels reduced in *Cd81*+ STC2 cells in *Red2-PIK3CA*^{H1047R} mice compared to *Red2-Kras*^{G12D} mice and the *Confetti* control (**Fig. 6h,i**). Moreover, consistent with the scRNA-seq analysis, we did not observe any changes in the expression of *Sfrp2* or *Rspo3* in *Red2-Kras*^{G12D} mice. Finally, we examined the expression change of STC2 by performing realtime qPCR. As in McCarthy et al., we isolated STC2 as the population of PDGFRA^{lo} CD81+ cells from the *Confetti* control as well as *Red2-Kras*^{G12D} and *Red2-PIK3CA*^{H1047R} mice using FACS (**Extended Data Fig. 9c,d**). Consistent with the scRNA-seq analysis (**Extended Data Fig. 9e**), realtime qPCR analysis confirmed that the expression of *Rspo3* was decreased in STC2 cells sorted from *Red2-PIK3CA*^{H1047R} mice compared to those from the *Confetti* control (**Extended Data Fig. 9f,g**). The expression of secreted WNT antagonists such as *Sfrp2* and *Sfrp4* was also increased in STC2 cells from *Red2-PIK3CA*^{H1047R} mice compared to the control (**Extended Data Fig. 9f,g**). Together, these results confirm the alterations of STC2 cells upon epithelial oncogene expression in *Red2-PIK3CA*^{H1047R} mice predicted by our scRNA-seq analysis.

We then examined whether oncogene-driven changes of STC2 compromises its niche function. We co-cultured Lgr5-EGFP+ ISCs with PDGFRA^{lo} CD81- STC1 cells or PDGFRA^{lo} CD81+ STC2 cells isolated from wild-type and *Red2-PIK3CA*^{H1047R} intestine at 2 weeks post-induction (4 mg/20 g body weight) (**Fig. 6j**). As expected, we found that the STC2 population from the wild-type control could support organoid formation even in growth factor-deprived conditions (-Nog Rspo^{low}), whereas the STC1 population could not, confirming the niche function of PDGFRA^{lo}

CD81+ STC2, as reported[49] (**Fig. 6k, l**). Interestingly, the STC2 population sorted from *Red2-PIK3CA*^{H1047R} intestine showed significantly reduced capacity to support organoid formation, compared to those of the *Confetti* control. These results suggest that STC2 is indeed an important niche component, as reported, and oncogenic PI3K activation in epithelial cells is likely to impede its niche function.

Based on the evidences for the oncogene-associated niche changes, we turned to the organoid culture system, which allows functional outcomes of different niche conditions to be validated directly. We tested two conditions: (1) withdrawal of Noggin from the full culture media (-Nog), which mimics a BMP-rich environment in *Red2-Kras*^{G12D}, and (2) withdrawal of Noggin in R-spondin reduced media (-Nog Rspo^{low}), which mimics the BMP-rich and Wnt-deprived environment in *Red2-PIK3CA*^{H1047R} (**Extended Data Fig. 9h**). Both conditions led to the formation of organoid structures with reduced organoid budding over 5 days as compared to control (**Extended Data Fig. 9i**). Notably, realtime qPCR analysis of lineage markers suggested that, although both conditions can reduce significantly the stem cell proportion (*Lgr5* and *Olfm4*), -Nog condition drives more goblet cell differentiation (*Clca1*), while -Nog Rspo^{low} condition drives more enterocyte differentiation (*Alpi* and *Aldh1a1*), as observed *in vivo* (**Extended Data Fig. 9j**). Expression of proliferation markers, such as *Mki67* and *Ccnb2*, were not increased in either condition, while well-known BMP targets *Id1* and *Ttr* were significantly induced (**Extended Data Fig. 9j**). We then directly confirmed the reduction of stem cell number by analysing Lgr5-EGFP reporter organoids (**Extended Data Fig. 9k**), as well as their activity using an organoid formation assay (**Extended Data Fig. 9l-n**), under both conditions. These results suggested that intestinal stem cells are very sensitive to BMP and R-spondin ligands so that only moderate

changes, such as withdrawal of Noggin, or reduction of R-spondin, can induce differentiation and reduce stem cell maintenance in organoid culture, as observed *in vivo*.

Finally, to further challenge our hypothesis that BMP and WNT signaling are involved in the crosstalk between wild-type and mutant clones *in vivo*, we utilised inhibitors that can block either reception of BMP ligands (LDN193189, BMP type I receptor blocking agent) or secretion of WNT ligands (LGK974, Porcupine inhibitor). We found that administration of LDN193189 and LGK974 to the *Red2Onco* mice could suppress BMP and WNT signalling, respectively (**Extended Data Fig. 10a,b**). In addition, LDN193189 rescues the accelerated clonal drift of wild-type clones neighboring mutant crypts, whereas LGK974 accelerates the drift still further (**Fig. 6m**). These qualitative observations were supported by clone size quantification, which showed a clear rescue of the increased clone size (**Fig. 6n**) and fixation rate (**Fig. 6o**) of neighboring wild-type clones after LDN193189 administration in both *Red2-Kras*^{G12D} and *Red2-PIK3CA*^{H1047R} animals. When compared to remote clones, it was apparent that the BMP gradient mediated effect is completely abolished by LDN193189 (**Fig. 6n,o**), while LGK974 administration still showed the trends with dramatically increased clone fixation rate (**Fig. 6n,o**). Notably, we also observed delayed fixation of mutant clones under LDN193189 treatment, suggesting that the unlabelled wild-type cells in the same crypt have competed more efficiently against the red mutants when the BMP effect was abolished (**Extended Data Fig. 10c,d**). We also confirmed that the phenotypes from both Red2 systems are largely recapitulated in *LSL-Kras*^{G12D} and *Pik3ca*$^{Lat\text{-}H1047R}$ mice expressing the respective oncogenes under the endogenous promoter (**Extended Data Fig. 10e-l**). Taken together, these results suggest that the increased BMP ligands and Wnt antagonist play an

important role in mediating the crosstalk between wild-type and mutant clones in *Red2-Kras*^{G12D} and *Red2-PIK3CA*^{H1047R} intestine.

DISCUSSION

Multicolor reporter mouse lines, such as the *MADM*, *Confetti* and *ifgMosaic* mouse models, have provided versatile systems to gather information on the functional fate behavior and clonal dynamics of targeted cell populations, particularly in situations where clone dispersion may limit single-color approaches due to clone misassignment[22-24]. Further, at higher mosaic levels of induction, they have provided the means to quantitatively study the large-scale dynamics of cell populations, with applications particularly in the context of developmental dynamics[62]. However, to date, the mosaicism of the multicolor reporter systems has not been utilized to study cell-cell communication between tumor cells and neighboring cells within the same animal. Here, we have developed a new lineage tracing strategy based on the multicolor *Confetti* reporter construct, the *Red2Onco* mouse model, to study in parallel the dynamics and fate behavior of wild-type and oncogene-expressing cells. This model provides a basis to quantify the functional and molecular changes that take place in both mutant and neighboring wild-type cells following the expression of mutant oncogenes, as well as the response of the wider tumor microenvironment.

Using the small intestine as a model system, we have shown how the Red2Onco system provides a platform to study changes in the fate behavior of epithelial cells and, through comparative gene expression profiling, identify candidate mechanisms of cellular crosstalk. As well as establishing the increased survival advantage of clones expressing different oncogenes, our results provide direct evidence for cellular crosstalk through which mutant epithelial cells influence the cellular organization and clonal dynamics of neighboring wild-type crypts. Further, using scRNA-seq analysis and organoid culture, we have determined candidate signaling pathways that mediate inter-crypt cellular crosstalk and that involve mesenchymal cells that belong to the shared niche.

Conventional lineage tracing techniques based on genetic recombination have proved useful in studying clone behavior in a cell- or tissue-specific manner by activation of a conditional reporter gene. Inducible Cre-labeling systems enable the temporal control of recombination, providing access to cell lineage relationships and fate behavior. Based on this design, several studies have combined this reporter system with oncogenic activation to study tumorigenic mutant clone behavior[16,17]. However, because of the stochastic character of the inducible Cre-driven excision of loxP sites, the frequency at which recombination occurs at both the reporter and oncogene locus is uncertain, making the clone data vulnerable to misinterpretation. Here, by using the viral 2A peptide, the expression of the fluorescent protein is correlated with high fidelity with the expression of the downstream gene of interest. Thus, the Red2Onco system is suitable for the precise analysis of oncogene-driven cell behavior.

Local cell displacement provides one mechanism for the elimination of “loser” cells in epithelial tissues. This type of competition has been observed in a variety of settings, including the *Drosophila* ovary[63] and intestine[64], as well as in the mouse esophagus[65], epidermis[66] and intestine[16,17] following the clonal acquisition of oncogenic mutations. In these cases, cell competition by mutant epithelial stem cells is mediated by the differentiation of neighboring wild-type stem cells, leading to their displacement from the niche. Our findings show that competition within the niche may not be limited to local cell interactions mediated by direct physical contact but, through paracrine signals, may occur over a longer range, affecting cells in neighboring niche domains. In this context, alterations of the niche signaling environment, resulting from direct changes in the gene expression signature of mutant cells or mediated indirectly through the

response of neighboring stromal and immune cells, may influence the renewal capacity of wild-type stem cells belonging to the same or a nearby niche. Such behavior echoes recent studies of the mouse intestinal epithelium that show that blockade of Wnt ligand secretion dramatically perturbs the size and dynamics of the stem cell compartment[67,68], providing further evidence that secreted niche factors can be one of the critical regulators of clonal dynamics in the niche. Indeed, alongside the two oncogenes considered here, mutants with Wnt activation caused by *Apc* loss also show a paracrine remodeling effect by secreting Wnt inhibitory factors (data not shown), suggesting that niche remodeling might be a general feature of tumorigenic mutants.

Together with two recent reports[61,69], our work implies an essential role of the PDGFRA^{lo} stromal cell population in maintaining ISCs at the crypt base and the BMP/Wnt gradient along the intestinal crypt-villus axis. Previous studies have established the central role of BMP and WNT signaling in controlling the balance between proliferation and differentiation of ISCs, and maintaining intestinal homeostasis[36,70-73]. BMP signaling inhibits the stem cell potential of ISC via Smad-mediated transcriptional repression of stem cell signature genes[74], whereas WNT signaling maintains self-renewal activity of ISCs[72]. While BMP ligands are mainly secreted from differentiated epithelial cells, as well as intra-villus and inter-crypt stromal cells[55-57,71], WNT ligands are expressed at the crypt base from multiple epithelial and non-epithelial sources[52,75-78]. In this context, a recent study[61] identified the PDGFRA^{lo} stromal cell population that is present just below the crypt base and secretes Grem1, a BMP antagonist, contributing a further mechanism to control the BMP/Wnt gradient, a finding consistent with our analysis. Another recent work[69] suggested an important role of the PDGFRA^{lo} stromal cell population in intestinal regeneration and tumorigenesis, with conclusions that echo the current findings showing the effects of

remodeling of the PDGFRA^{lo} STC2 population under the activation of mutant PI3K. Furthermore, our work also highlights that the alteration of PDGFRA^{lo} STC2 cells may depend sensitively on oncogene type, as exemplified by the changes in *Red2-PIK3CA*^{H1047R} mice, but not in *Red2-Kras*^{G12D} mice. Importantly, this STC2 population seems to be distinct population from Foxl1+ telocytes (**Extended Data Fig. 9g**). Taken together, these findings suggest that PDGFRA^{lo} stromal cells may function as a key signaling center among resident stromal and immune cells in the context of intestinal homeostasis, regeneration, and cancer.

In summary, the Red2Onco system offers a singular opportunity to study whether and how oncogene-expressing tumorigenic cells influence, and are influenced by, neighboring wild-type cells. Such strategies are essential for elucidating the possible non-cell autonomous effects of mutant cells on their microenvironment. When combined with modern strategies for single-cell expression profiling, the Red2Onco system offers the potential to characterize both the existence and nature of cell competition, especially in epithelial tissue types, and the candidate molecular mechanisms and pathways that effect cellular crosstalk.

REFERENCES

1 Hanahan, D. & Weinberg, R. A. Hallmarks of cancer: the next generation. *Cell* **144**, 646-674, doi:10.1016/j.cell.2011.02.013 (2011).

2 Medema, J. P. & Vermeulen, L. Microenvironmental regulation of stem cells in intestinal homeostasis and cancer. *Nature* **474**, 318-326, doi:10.1038/nature10212 (2011).

3 Hanahan, D. & Coussens, L. M. Accessories to the crime: functions of cells recruited to the tumor microenvironment. *Cancer Cell* **21**, 309-322, doi:10.1016/j.ccr.2012.02.022 (2012).

4 Quail, D. F. & Joyce, J. A. Microenvironmental regulation of tumor progression and metastasis. *Nat Med* **19**, 1423-1437, doi:10.1038/nm.3394 (2013).

5 Moreno, E. & Rhiner, C. Darwin's multicellularity: from neurotrophic theories and cell competition to fitness fingerprints. *Curr Opin Cell Biol* **31**, 16-22, doi:10.1016/j.ceb.2014.06.011 (2014).

6 Claveria, C. & Torres, M. Cell Competition: Mechanisms and Physiological Roles. *Annu Rev Cell Dev Biol* **32**, 411-439, doi:10.1146/annurev-cellbio-111315-125142 (2016).

7 Amoyel, M. & Bach, E. A. Cell competition: how to eliminate your neighbours. *Development* **141**, 988-1000, doi:10.1242/dev.079129 (2014).

8 Di Gregorio, A., Bowling, S. & Rodriguez, Tristan A. Cell Competition and Its Role in the Regulation of Cell Fitness from Development to Cancer. *Developmental Cell* **38**, 621-634, doi:10.1016/j.devcel.2016.08.012 (2016).

9 Maruyama, T. & Fujita, Y. Cell competition in mammals - novel homeostatic machinery for embryonic development and cancer prevention. *Curr Opin Cell Biol* **48**, 106-112, doi:10.1016/j.ceb.2017.06.007 (2017).

10 Egeblad, M., Nakasone, E. S. & Werb, Z. Tumors as organs: complex tissues that interface with the entire organism. *Dev Cell* **18**, 884-901, doi:10.1016/j.devcel.2010.05.012 (2010).

11 Curtius, K., Wright, N. A. & Graham, T. A. An evolutionary perspective on field cancerization. *Nat Rev Cancer* **18**, 19-32, doi:10.1038/nrc.2017.102 (2018).

12 Bjerknes, M. & Cheng, H. Colossal crypts bordering colon adenomas in Apc(Min) mice express full-length Apc. *Am J Pathol* **154**, 1831-1834, doi:10.1016/S0002-9440(10)65439-9 (1999).

13 Blanpain, C. & Simons, B. D. Unravelling stem cell dynamics by lineage tracing. *Nat Rev Mol Cell Biol* **14**, 489-502, doi:10.1038/nrm3625 (2013).

14 Vermeulen, L. & Snippert, H. J. Stem cell dynamics in homeostasis and cancer of the intestine. *Nat Rev Cancer* **14**, 468-480, doi:10.1038/nrc3744 (2014).

15 Baron, C. S. & van Oudenaarden, A. Unravelling cellular relationships during development and regeneration using genetic lineage tracing. *Nat Rev Mol Cell Biol* **20**, 753-765, doi:10.1038/s41580-019-0186-3 (2019).

16 Vermeulen, L. *et al.* Defining stem cell dynamics in models of intestinal tumor initiation. *Science* **342**, 995-998, doi:10.1126/science.1243148 (2013).

17 Snippert, H. J., Schepers, A. G., van Es, J. H., Simons, B. D. & Clevers, H. Biased competition between Lgr5 intestinal stem cells driven by oncogenic mutation induces clonal expansion. *EMBO Rep* **15**, 62-69, doi:10.1002/embr.201337799 (2014).

18 Ritsma, L. *et al.* Intestinal crypt homeostasis revealed at single-stem-cell level by in vivo live imaging. *Nature* **507**, 362-365, doi:10.1038/nature12972 (2014).

19 Cortina, C. *et al.* A genome editing approach to study cancer stem cells in human tumors. *EMBO Mol Med* **9**, 869-879, doi:10.15252/emmm.201707550 (2017).

20 Shimokawa, M. *et al.* Visualization and targeting of LGR5(+) human colon cancer stem cells. *Nature* **545**, 187-192, doi:10.1038/nature22081 (2017).

21 Merino, D. *et al.* Barcoding reveals complex clonal behavior in patient-derived xenografts of metastatic triple negative breast cancer. *Nat Commun* **10**, 766, doi:10.1038/s41467-019-08595-2 (2019).

22 Zong, H., Espinosa, J. S., Su, H. H., Muzumdar, M. D. & Luo, L. Mosaic analysis with double markers in mice. *Cell* **121**, 479-492, doi:10.1016/j.cell.2005.02.012 (2005).

23 Pontes-Quero, S. *et al.* Dual ifgMosaic: A Versatile Method for Multispectral and Combinatorial Mosaic Gene-Function Analysis. *Cell* **170**, 800-814 e818, doi:10.1016/j.cell.2017.07.031 (2017).

24 Snippert, H. J. *et al.* Intestinal crypt homeostasis results from neutral competition between symmetrically dividing Lgr5 stem cells. *Cell* **143**, 134-144, doi:10.1016/j.cell.2010.09.016 (2010).

25 Haigis, K. M. *et al.* Differential effects of oncogenic K-Ras and N-Ras on proliferation, differentiation and tumor progression in the colon. *Nat Genet* **40**, 600-608, doi:10.1038/ng.115 (2008).

26 Feng, Y. *et al.* Mutant KRAS promotes hyperplasia and alters differentiation in the colon epithelium but does not expand the presumptive stem cell pool. *Gastroenterology* **141**, 1003-1013 e1001-1010, doi:10.1053/j.gastro.2011.05.007 (2011).

27 Poulin, E. J. *et al.* Tissue-Specific Oncogenic Activity of KRAS(A146T). *Cancer Discov* **9**, 738-755, doi:10.1158/2159-8290.CD-18-1220 (2019).

28 Sheng, H., Shao, J., Townsend, C. M., Jr. & Evers, B. M. Phosphatidylinositol 3-kinase mediates proliferative signals in intestinal epithelial cells. *Gut* **52**, 1472-1478, doi:10.1136/gut.52.10.1472 (2003).

29 He, X. C. *et al.* PTEN-deficient intestinal stem cells initiate intestinal polyposis. *Nat Genet* **39**, 189-198, doi:10.1038/ng1928 (2007).

30 Stanger, B. Z., Datar, R., Murtaugh, L. C. & Melton, D. A. Direct regulation of intestinal fate by Notch. *Proc Natl Acad Sci U S A* **102**, 12443-12448, doi:10.1073/pnas.0505690102 (2005).

31 Mukhopadhyay, A., Krishnaswami, S. R. & Yu, B. D. Activated Kras alters epidermal homeostasis of mouse skin, resulting in redundant skin and defective hair cycling. *J Invest Dermatol* **131**, 311-319, doi:10.1038/jid.2010.296 (2011).

32 Jackson, E. L. *et al.* Analysis of lung tumor initiation and progression using conditional expression of oncogenic K-ras. *Genes Dev* **15**, 3243-3248, doi:10.1101/gad.943001 (2001).

33 Kim, T. H. & Shivdasani, R. A. Notch signaling in stomach epithelial stem cell homeostasis. *J Exp Med* **208**, 677-688, doi:10.1084/jem.20101737 (2011).

34 Ying, Z., Sandoval, M. & Beronja, S. Oncogenic activation of PI3K induces progenitor cell differentiation to suppress epidermal growth. *Nat Cell Biol* **20**, 1256-1266, doi:10.1038/s41556-018-0218-9 (2018).

35 Hingorani, S. R. *et al.* Preinvasive and invasive ductal pancreatic cancer and its early detection in the mouse. *Cancer Cell* **4**, 437-450, doi:10.1016/s1535-6108(03)00309-x (2003).

36 Gehart, H. & Clevers, H. Tales from the crypt: new insights into intestinal stem cells. *Nat Rev Gastroenterol Hepatol* **16**, 19-34, doi:10.1038/s41575-018-0081-y (2019).

37 Barker, N. *et al.* Identification of stem cells in small intestine and colon by marker gene Lgr5. *Nature* **449**, 1003-1007, doi:10.1038/nature06196 (2007).

38 Lopez-Garcia, C., Klein, A. M., Simons, B. D. & Winton, D. J. Intestinal stem cell replacement follows a pattern of neutral drift. *Science* **330**, 822-825, doi:10.1126/science.1196236 (2010).

39 Kozar, S. *et al.* Continuous clonal labeling reveals small numbers of functional stem cells in intestinal crypts and adenomas. *Cell Stem Cell* **13**, 626-633, doi:10.1016/j.stem.2013.08.001 (2013).

40 Fearon, E. R. Molecular genetics of colorectal cancer. *Annu Rev Pathol* **6**, 479-507, doi:10.1146/annurev-pathol-011110-130235 (2011).

41 Cancer Genome Atlas, N. Comprehensive molecular characterization of human colon and rectal cancer. *Nature* **487**, 330-337, doi:10.1038/nature11252 (2012).

42 Nicholson, A. M. *et al.* Fixation and Spread of Somatic Mutations in Adult Human Colonic Epithelium. *Cell Stem Cell* **22**, 909-918 e908, doi:10.1016/j.stem.2018.04.020 (2018).

43 Holzmann, K. *et al.* Comparative analysis of histology, DNA content, p53 and Ki-ras mutations in colectomy specimens with long-standing ulcerative colitis. *Int J Cancer* **76**, 1-6, doi:10.1002/(sici)1097-0215(19980330)76:1<1::aid-ijc1>3.0.co;2-4 (1998).

44 Leedham, S. J. *et al.* Clonality, founder mutations, and field cancerization in human ulcerative colitis-associated neoplasia. *Gastroenterology* **136**, 542-550 e546, doi:10.1053/j.gastro.2008.10.086 (2009).

45 Galandiuk, S. *et al.* Field cancerization in the intestinal epithelium of patients with Crohn's ileocolitis. *Gastroenterology* **142**, 855-864 e858, doi:10.1053/j.gastro.2011.12.004 (2012).

46 Bruens, L., Ellenbroek, S. I. J., van Rheenen, J. & Snippert, H. J. In Vivo Imaging Reveals Existence of Crypt Fission and Fusion in Adult Mouse Intestine. *Gastroenterology* **153**, 674-677 e673, doi:10.1053/j.gastro.2017.05.019 (2017).

47 Grun, D. *et al.* Single-cell messenger RNA sequencing reveals rare intestinal cell types. *Nature* **525**, 251-255, doi:10.1038/nature14966 (2015).

48 Haber, A. L. *et al.* A single-cell survey of the small intestinal epithelium. *Nature* **551**, 333-339, doi:10.1038/nature24489 (2017).

49 Biton, M. *et al.* T Helper Cell Cytokines Modulate Intestinal Stem Cell Renewal and Differentiation. *Cell* **175**, 1307-1320 e1322, doi:10.1016/j.cell.2018.10.008 (2018).

50 Ayyaz, A. *et al.* Single-cell transcriptomes of the regenerating intestine reveal a revival stem cell. *Nature* **569**, 121-125, doi:10.1038/s41586-019-1154-y (2019).

51 Cheng, C. W. *et al.* Ketone Body Signaling Mediates Intestinal Stem Cell Homeostasis and Adaptation to Diet. *Cell* **178**, 1115-1131 e1115, doi:10.1016/j.cell.2019.07.048 (2019).

52 Stzepourginski, I. *et al.* CD34+ mesenchymal cells are a major component of the intestinal stem cells niche at homeostasis and after injury. *Proc Natl Acad Sci U S A* **114**, E506-E513, doi:10.1073/pnas.1620059114 (2017).

53 Greicius, G. *et al.* PDGFRalpha(+) pericryptal stromal cells are the critical source of Wnts and RSPO3 for murine intestinal stem cells in vivo. *Proc Natl Acad Sci U S A* **115**, E3173-E3181, doi:10.1073/pnas.1713510115 (2018).

54 Pinto, D., Gregorieff, A., Begthel, H. & Clevers, H. Canonical Wnt signals are essential for homeostasis of the intestinal epithelium. *Genes Dev* **17**, 1709-1713, doi:10.1101/gad.267103 (2003).

55 Hardwick, J. C. *et al.* Bone morphogenetic protein 2 is expressed by, and acts upon, mature epithelial cells in the colon. *Gastroenterology* **126**, 111-121, doi:10.1053/j.gastro.2003.10.067 (2004).

56 Batts, L. E., Polk, D. B., Dubois, R. N. & Kulessa, H. Bmp signaling is required for intestinal growth and morphogenesis. *Dev Dyn* **235**, 1563-1570, doi:10.1002/dvdy.20741 (2006).

57 Thorne, C. A. *et al.* Enteroid Monolayers Reveal an Autonomous WNT and BMP Circuit Controlling Intestinal Epithelial Growth and Organization. *Dev Cell* **44**, 624-633 e624, doi:10.1016/j.devcel.2018.01.024 (2018).

58 Drost, J. *et al.* Sequential cancer mutations in cultured human intestinal stem cells. *Nature* **521**, 43-47, doi:10.1038/nature14415 (2015).

59 Matano, M. *et al.* Modeling colorectal cancer using CRISPR-Cas9-mediated engineering of human intestinal organoids. *Nat Med* **21**, 256-262, doi:10.1038/nm.3802 (2015).

60 Fujii, M. *et al.* A Colorectal Tumor Organoid Library Demonstrates Progressive Loss of Niche Factor Requirements during Tumorigenesis. *Cell Stem Cell* **18**, 827-838, doi:10.1016/j.stem.2016.04.003 (2016).

61 McCarthy, N. *et al.* Distinct Mesenchymal Cell Populations Generate the Essential Intestinal BMP Signaling Gradient. *Cell Stem Cell* **26**, 391-402 e395, doi:10.1016/j.stem.2020.01.008 (2020).

62 Rulands, S. *et al.* Universality of clone dynamics during tissue development. *Nat Phys* **14**, 469-474, doi:10.1038/s41567-018-0055-6 (2018).

63 Jin, Z. *et al.* Differentiation-defective stem cells outcompete normal stem cells for niche occupancy in the Drosophila ovary. *Cell Stem Cell* **2**, 39-49, doi:10.1016/j.stem.2007.10.021 (2008).

64 Kolahgar, G. *et al.* Cell Competition Modifies Adult Stem Cell and Tissue Population Dynamics in a JAK-STAT-Dependent Manner. *Dev Cell* **34**, 297-309, doi:10.1016/j.devcel.2015.06.010 (2015).

65 Alcolea, M. P. *et al.* Differentiation imbalance in single oesophageal progenitor cells causes clonal immortalization and field change. *Nat Cell Biol* **16**, 615-622, doi:10.1038/ncb2963 (2014).

66 Ellis, S. J. *et al.* Distinct modes of cell competition shape mammalian tissue morphogenesis. *Nature* **569**, 497-502, doi:10.1038/s41586-019-1199-y (2019).

67 Yan, K. S. *et al.* Non-equivalence of Wnt and R-spondin ligands during Lgr5(+) intestinal stem-cell self-renewal. *Nature* **545**, 238-242, doi:10.1038/nature22313 (2017).

68 Huels, D. J. *et al.* Wnt ligands influence tumour initiation by controlling the number of intestinal stem cells. *Nat Commun* **9**, 1132, doi:10.1038/s41467-018-03426-2 (2018).

69 Roulis, M. *et al.* Paracrine orchestration of intestinal tumorigenesis by a mesenchymal niche. *Nature* **580**, 524-529, doi:10.1038/s41586-020-2166-3 (2020).

70 Korinek, V. *et al.* Depletion of epithelial stem-cell compartments in the small intestine of mice lacking Tcf-4. *Nat Genet* **19**, 379-383, doi:10.1038/1270 (1998).

71 Haramis, A. P. *et al.* De novo crypt formation and juvenile polyposis on BMP inhibition in mouse intestine. *Science* **303**, 1684-1686, doi:10.1126/science.1093587 (2004).

72 van Es, J. H. *et al.* A critical role for the Wnt effector Tcf4 in adult intestinal homeostatic self-renewal. *Mol Cell Biol* **32**, 1918-1927, doi:10.1128/MCB.06288-11 (2012).

73 Davis, H. *et al.* Aberrant epithelial GREM1 expression initiates colonic tumorigenesis from cells outside the stem cell niche. *Nat Med* **21**, 62-70, doi:10.1038/nm.3750 (2015).

74 Qi, Z. *et al.* BMP restricts stemness of intestinal Lgr5(+) stem cells by directly suppressing their signature genes. *Nat Commun* **8**, 13824, doi:10.1038/ncomms13824 (2017).

75 Sato, T. *et al.* Paneth cells constitute the niche for Lgr5 stem cells in intestinal crypts. *Nature* **469**, 415-418, doi:10.1038/nature09637 (2011).

76 Farin, H. F., Van Es, J. H. & Clevers, H. Redundant sources of Wnt regulate intestinal stem cells and promote formation of Paneth cells. *Gastroenterology* **143**, 1518-1529 e1517, doi:10.1053/j.gastro.2012.08.031 (2012).

77 Degirmenci, B., Valenta, T., Dimitrieva, S., Hausmann, G. & Basler, K. GLI1-expressing mesenchymal cells form the essential Wnt-secreting niche for colon stem cells. *Nature* **558**, 449-453, doi:10.1038/s41586-018-0190-3 (2018).

78 Shoshkes-Carmel, M. *et al.* Subepithelial telocytes are an important source of Wnts that supports intestinal crypts. *Nature* **557**, 242-246, doi:10.1038/s41586-018-0084-4 (2018).

Methods

Mice

All inducible Cre lines (*R26R-CreERT2*: JAX006965, *Villin-CreERT2*: JAX020282, *Lgr5-EGFP-IRES-CreERT2*: JAX008875, *Sftpc-CreERT2*: JAX028054, *Krt5-CreERT2:* JAX02915), the *R26R-Confetti* line (JAX017492) and *LSL-Kras*^{G12D} (JAX008179) line were obtained from The Jackson Laboratory. *Pik3ca*$^{Lat\text{-}H1047R}$ line was donated by W.A Phillips[79]. *Red2Onco* targeting vectors were generated by gene synthesis. Oncogene sequences were obtained from Addgene (*Notch1ICD:* Addgene plasmid #15079[80], *Kras*^{G12D}: Addgene plasmid #11549[81], *PIK3CA*^{H1047R}: Addgene plasmid #12524[82]). Mice were created by inserting the *Red2Onco* cassette into the *tdimer2* locus in ES cells obtained from *R26R-Confetti* mice using CRISPR-Cas9 nickase-mediated homologous recombination. Insertion of the oncogenic sequence was confirmed by long-range PCR. Specific genotyping primers were designed outside of the homology arms and were used in combination with primers within the knock-in cassette. Strategy development and targeting vector generation for *Red2Onco* targeting vectors was performed with the help of the Wellcome Trust–Medical Research Council Cambridge Stem Cell Institute Advanced Vector Design and Recombineering facility. Subsequent modifications to the resulting vectors were implemented by In-Fusion cloning (Takara).

Animal treatments

All experiments were approved by the UK Medical Research Council and University of Cambridge local ethical review committees and conducted according to Home Office project license PPL70/8296. To perform lineage tracing, tamoxifen (Sigma, T5648) dissolved in corn oil was injected intraperitoneally into 8–12-week old mice. As indicated, the dose of tamoxifen used for

each experiment was determined based on recombination efficiency. For the clonal analysis, it is crucial that crypts are marked at clonal density so that labelled cells can be identified reliably as the output of an individual labelled cell. Titration experiments indicated this can be achieved by tamoxifen dose of 0.2 mg/20 g mouse body weight. Tamoxifen and chemical inhibitors (LDN193189, BMP type I receptor blocking agent, Selleckchem, S2618; LGK974, Porcupine inhibitor, Cayman Chemical, 14072) were concomitantly administered as indicated (**Fig. 6m**). LGK974 and LDN193189 were administered every 48 h through oral gavage, in a concentration of 5 mg/kg (LGK974) or 3mg/kg (LDN193189) in a vehicle of 0.5% Tween-80/0.5% methylcellulose. Chemical-treated mice did not show any loss of body weight or physical activity, demonstrating that they had no severe toxic side effects.

All mice were group housed under specific pathogen-free conditions and had not previously undergone any procedures. Experiments were carried out with male and female animals, except for single-cell transcriptomic analysis, where only females were used. No gender-specific differences were observed. All procedures were performed according to UK Home Office regulations and local animal welfare committee guidelines.

Intestine preparation

Mice were euthanized by cervical dislocation and the intestine collected by dissection. The small intestine was cut longitudinally and subsequently placed on a piece of cold PBS soaked 3M paper, using forceps to flatten the tissue before fixation in 4% paraformaldehyde at 4 °C O/N (~18 h) with shaking. After fixation the intestine was washed for 3 x 6 h with PBS at 4 °C with shaking.

Tissue clearing and immunofluorescence

CUBIC clearings were performed as previously described[83]. Briefly, fixed tissue was dissected into small fragments (~2 cm) and transferred into 10 mL CUBIC R1a solution (10% urea, 5% N,N,N',N'-tetrakis(2-hydroxypropyl) ethyl-enediamine, 10% Triton X-100 and 25 mM NaCl in distilled water) in a 15 mL conical tube and incubated for 2 days at 37 °C with shaking. All subsequent incubation steps were then performed at 4 °C on a rotor. The fragments were incubated with blocking and permeabilization solution consisting of 5% DMSO, 0.5% Triton-X-100 and 2% Normal donkey serum (NDS) in PBS O/N. The following day, the solution was replaced with primary antibody for cleaved caspase-3 (1:200; Cell Signaling Technology, 9661), OLFM4 (1:100; Cell Signaling Technology, 39141), p-ERK (1:100; Cell Signaling Technology, 4370), p-AKT (1:100; Cell Signaling Technology, 4060) or $KRAS^{G12D}$ (1:100; Cell Signaling Technology, 14429) diluted in blocking solution (1% DMSO, 0.5% Triton-X-100 and 2% NDS in PBS), and the whole mount was incubated for 3 days. The samples were then washed 6 times with fresh PBS over a 24 h period before incubating with secondary antibody (1:500; donkey anti-rabbit or anti-mouse, Invitrogen) diluted in blocking solution for 3 days. The samples were then washed 6 times with PBS and incubated with 2 µg/mL DAPI in PBS for 24 h. The samples were then transferred into 10 mL CUBIC R2 solution (50% sucrose, 25% urea, 10% 2,20,20'-nitrilotrie-thanol and 0.1% Triton X-100 in distilled water) in a 15 mL conical tube and incubated for 2 days at room temperature with shaking. To match the refractive index, samples were transferred into an Eppendorf tube containing 1 mL RapiClear 1.52 (Sunjin Lab) and incubated O/N at 4 °C. Samples were then mounted in a 0.25 mm i-spacer (Sunjin Lab) for confocal imaging.

Proliferation assay

To measure cell proliferation *in vivo*, 1 mg of 5-ethynyl-2´-deoxyuridine (EdU) (Life Technologies, A10044) was dissolved in 200 µL of PBS and injected into each mouse. Tissues were collected after 2 h and a Click-iT EdU Alexa Fluor 647 Imaging Kit (Thermo Fisher, C10340) was used to detect EdU+ cells.

Immunohistochemistry on near-native sections.

Organs were dissected, fixed and embedded in 4% low melt agarose as previously described[84] for generation of 100 µm-thick near-native sections using the LAICA VT 1000S Vibratome. The sections were removed from any remaining agarose using forceps and subsequently transferred to a 12-well plate into wells containing blocking and permeabilization solution (5% DMSO, 0.5% Triton-X-100 and 2% NDS in PBS) to be incubated O/N (~18 h) at 4 °C with shaking. The following day, the blocking and permeabilization solution was replaced with primary antibody for CPA1 (1:200; R&D systems, AF2765), β-catenin (1:200; Santa Cruz, sc-7199), SPC (1:300; Millipore, AB3786), LYZ (1:200; DAKO, A009902-2) or MUC2 (1:200; Abcam, ab90007) diluted in blocking solution (1% DMSO, 0.5% Triton-X-100 and 2% NDS in PBS) and the section incubated for 72 h at 4 °C. Sections were subsequently washed and incubated with secondary antibody (1:500; donkey anti-rabbit or goat AF647, Invitrogen) and DAPI diluted in blocking solution (1% DMSO, 0.5% Triton-X-100 and 2% NDS in PBS) for 48 h at room temperature with shaking. After washing for 3 x 2 h with PBS, sections were carefully transferred from wells to microscope slides using a brush before mounting in RapiClear 1.52 (Sunjin Lab).

Immunohistochemistry on paraffin sections.

Immunohistochemistry was performed according to standard protocols. Briefly, the intestine was dissected and fixed in 4% PFA O/N at 4 °C before paraffin embedding. Paraffin-embedded sections (5 μm) were rehydrated, and the epitopes were exposed using Tris/ethylenediaminetetraacetic acid (EDTA) buffer. Sections were then incubated in blocking solution (2% donkey or goat serum, 5% DMSO and 0.5% Triton-X-100 in PBS) at room temperature for 2 h. Primary antibody for NOTCH1 (1:100; Abcam, ab52627) was diluted in blocking solution (1% DMSO, 0.5% Triton-X-100 and 2% normal goat serum in PBS) and the sections were incubated in this for 24 h at 4 °C. Sections were subsequently washed and incubated with secondary antibody (1:500; Goat anti-rabbit HRP, Perkin Elmer) and DAPI diluted in blocking solution (1% DMSO, 0.5% Triton-X-100 and 2% normal goat serum in PBS) for 2 h at room temperature with shaking. The TSA kits, TSA Plus Cyanine 5 System (Perkin Elmer, NEL752001KT) were used for visualization.

In situ hybridization in cryo sections

RNA staining was performed with an RNAscope Multiplex Reagent Kit V2 (ACDBio, 323100) following the manufacturer's protocols. Collected tissues was fixed with 4% PFA, cryoprotected in OCT and sectioned at 16um. Briefly, the sections were pre-treated with Protease IV for 15 min. ACD designed and synthetized probes were used to detect transcripts of interest. Up to two probes were hybridised simultaneously. The RNAscope assay was followed by a regular immunostaining protocol with antibodies for RFP (1:50; SICGEN, AB8181-200), $KRAS^{G12D}$ (1:250; Cell Signaling Technology, 14429), or p-AKT (1:50; Cell Signaling Technology, 4060). Sections were subsequently washed and incubated with secondary antibody (1:500; Horse anti-rabbit, Vector Lab or Donkey anti-goat HRP, GeneTex) and mounted with Prolong Gold antifade reagent

supplemented with DAPI. Probes for *Fabp1* (Cat No. 562831), *Axin2* (Cat No. 400331), *Id1* (Cat No. 312221), *Bmp2* (Cat No. 406661-C2), *Grem1* (Cat No. 314741-C3), *Sfrp2* (Cat No. 576891-C2), *Cd81* (Cat No. 556971), *Rspo3* (Cat No. 402011-C3) were purchased from ACDBio. The TSA kits, TSA Plus Cyanine 5 (Perkin Elmer, NEL745001KT), TSA Plus Fluorescein (Perkin Elmer, NEL751001KT) and TSA Plus TMR (Perkin Elmer, NEL752001KT) were used for visualization. The multiplexed staining was performed with the help of the Wellcome Trust–Medical Research Council Cambridge Stem Cell Institute Histology facility.

Single cell sorting for sequencing

Intestinal cell dissociation was performed as previously described with a few modifications to deplete villi further and enrich for intestinal crypts[48,85]. Briefly, the proximal half of small intestines were carefully washed with cold PBS and villi were scraped off using a cover slip. The remaining tissue with crypts and lamina propria were then cut into 2 mm fragments and incubated in 10 mL Gentle Cell Dissociation Reagent (STEMCELL technologies) at 4 °C for 30 min. The fragments were then shaken vigorously and the supernatant was collected as the first fraction in a new conical tube. The remaining fragments were further incubated in fresh Gentle Cell Dissociation Reagent and a new fraction was collected every 30 min. The first and second fractions were discarded since they might contain some debris and villi. The third to fifth fractions contained the majority of the intestinal crypts. The crypt-enriched fractions were then washed with 10 mL of cold PBS and filtered through a 100 μm cell strainer (Falcon). The crypts were then further dissociated into single cells by incubation with TrypLE Express enzyme (GIBCO) at 37 °C for 5 min. The cells were filtered through a 40 μm cell strainer (Falcon). Remaining fragments with lamina propria were further digested with dissociation solution (2.5 mg/mL Liberase TL, Sigma;

10 U/mL DNAse, Promega) at 37 °C for 1 h. To aid dissociation, we gently mixed tissue pieces by pipetting up and down every 10 min. After 20 min, supernatants were harvested and 1 volume of DMEM containing 10% fetal bovine serum (FBS, Sigma Aldrich) was added while adding 5 mL of fresh dissociation mix to the remaining tissue pieces. This step was repeated 3 times for a total time of 1 h. After completion of the 3 cycles, the remaining intestinal fragments were mechanically disaggregated on a 100 μm mesh using a syringe plunger. The cell suspension was filtered through a 40 μm cell strainer into a 15 mL tube. The tube and filters were washed twice with 1 mL of 2% FBS in PBS and the cell suspension was then centrifuged at 300 *g* for 5 min. The supernatant was removed and the cell pellets were resuspended in 100 μL of antibody mix (2% FBS; 1:125 CD45 (30-F11)-APC, BD Biosciences; 1:125 EPCAM (G8.8)-PE-Cy7, BioLegend) and incubated for 1 h on ice. Both epithelial and lamina propria cells were then washed with 3 mL of 2% FBS in PBS and filtered once more if clumps were observed. After centrifugation at 300 *g* for 5 min, the cell pellets were resuspended in 1 mL of 2% FBS and 10 U/mL DNAse in PBS for sorting. The MOFLO system (Beckman Coulter) of the Wellcome Trust-Medical Research Council Cambridge Stem Cell Institute Flow Cytometry Facility was used for sorting and data were analyzed with FlowJo software (BD).

Library preparation and sequencing of RNA from single cells

scRNA-seq libraries were generated using 10X Genomics kits at the CRUK-CI Genomics Core Facility of the CRUK Cambridge Institute. Since we wished to achieve statistically significant results across the wide range of intestinal cell types, for each biological replicate, cells sorted from gates R5, R6, R7 and R8 (**Extended Data Fig. 6a**) were pooled in equal ratios (RFP+ epithelial cell: YFP+ epithelial cell: mesenchymal cell: immune cells = 1: 1: 1: 1) and loaded into one

channel of a 10X Chromium microfluidics chip to package them into one library. Thus, as a result of this enrichment, the relative proportions of epithelial cells, immune cells and mesenchymal cells are not expected to reflect the *in vivo* ratios found in the small intestine. In our experiments, 7 biological replicates (2 for the *Confetti*, 3 for the *Red2-Kras*^{G12D} and 2 for the *Red2-PIK3CA*^{H1047R} models) were used to make 7 libraries in total. The libraries were sequenced on an Illumina HiSeq 4000 in the core facility above.

Intestinal organoid culture and imaging

Intestinal epithelial organoids were established as previously described[75]. Briefly, we freshly isolated crypts from mouse small intestine and mixed the crypts with 20 µl of Matrigel (Corning). After Matrigel polymerization, the crypts were cultured in ENR medium composed of advanced Dulbecco's modified Eagle's medium/F12 supplemented with penicillin/streptomycin, 10 mM HEPES, Glutamax, N2 (Life Technologies), B27 (Life Technologies) and 1 mM N-acetylcysteine (Sigma), 50 ng/ml murine recombinant epidermal growth factor (EGF; Peprotech), R-spondin1 (conditioned medium from 293T-HA-RspoI-Fc cells, 10% final volume), and 100 ng/ml Noggin (Peprotech) for 3 days to generate organoids. Organoids were then treated with either Noggin-deprived medium (-Nog) or Noggin-deprived and R-spondin reduced medium (-Nog Rspo^{low}) (R-spondin1, 1% final volume) for 2 days (**Extended Data Fig. 9h-k**). For organoid formation assay (**Extended Data Fig. 9l-m**), organoids were collected 2 days after treatment and then dissociated into single cell with TrypLE (Thermo Fisher Scientific) for 5 min at 37 °C. The dissociated cells were filtered through a 40 µm cell strainer (Falcon). 2×10^4 collected cells were mixed with 20 µl of Matrigel and seeded in each well of 48-well plate. After 20 min of solidification at 37 °C, 250 µl of WENR medium was added. ENR was supplemented with Wnt3a (conditioned medium from

Wnt3a L-cells, 50% final volume), 10 μM Y-27632 (ROCK inhibitor, STEMCELL Technologies) to make the WENR medium. Organoids were imaged and counted using an EVOS M7000 microscope (Thermo Scientific).

To obtain organoids from *Confetti* or *Red2Onco* mice, RFP+ cells were sorted from *Villin-CreERT2;R26R-Confetti* or *Red2Onco* mice at 2w post-tamoxifen administration. 1×10^5 sorted cells were pelleted in 20 μl of Matrigel. After solidification at 37 °C, 250 μl of WENR medium was added. After 7 days, organoids were supplemented with Noggin-deprived medium (-Nog) to generate conditioned medium. The conditioned medium was harvested after 7 days of culture. The medium was centrifuged at 1000 *g* for 5 min at 4°C, the supernatant was then filtered through 0.22mm filter (Sartorius). Wild-type organoids were then treated with either conditioned medium from *R26R-Confetti* or *Red2Onco* mice for 6 h with or without LDN193189, BMP type I receptor blocking agent (Selleckchem, S2618, 1 μM) to assess the effect of the conditioned medium on activation of BMP signalling.

RNA isolation and quantitative PCR

Organoids were harvested by dissolving Matrigel with ice-cold PBS. Following centrifugation at 300 *g* for 5 min at 4°C, the supernatant was removed and the pelleted organoids were resuspended in 350 uL of RLT buffer (QIAGEN). Total RNA was isolated using RNeasy Mini Kit (QIAGEN) according to the manufacturer's instructions. Equivalent quantities of total RNA were reverse-transcribed to synthesize cDNA using SuperScript cDNA synthesis kit (Life Technology). Quantitative PCR was performed using Power SYBR Green PCR Master Mix (Thermo). Primer sequences are as follows:

Lgr5: F- CGGGACCTTGAAGATTTCCT, R- GATTCGGATCAGCCAGCTAC

Olfm4: F- CGAGACTATCGGATTCGCTATG, R- TTGTAGGCAGCCAGAGGGAG

Id1: F- ATCGCATCTTGTGTCGCTGAG, R- AGTCTCTGGAGGCTGAAAGGT

Ttr: F- AGCCCTTTGCCTCTGGGAAGAC, R- TGCGATGGTGTAGTGGCGATGG

Chga: F- GTCTCCAGACACTCAGGGCT, R- ATGACAAAAGGGGACACCAA

Clca1: F- TCTTGTGTAGATGCCATCATTTTT, R- CCAATGTCACAGCCCTCATA

Lyz: F- ATGGAATGGCTGGCTACTATGGAG, R- CTCACCACCCTCTTTGCACATTG

Alpi: F- AGGATCCATCTGTCCTTTGG, R- ACGTTGTATGTCTTGGACAG

Aldh1a1: F- TGTCGGATTTAGGAGGCTGC, R- GCATTGGAAAATTCCAGGGGATG

Mki67: F- CCAGCTGCCTGTAGTGTCAA, R- TCTTGAGGCTCGCCTTGATG

Ccnb2: F- GCCAAGAGCCATGTGACTATC, R- CAGAGCTGGTACTTTGGTGTTC

Axin2: F- GCTCCAGAAGATCACAAAGAGC, R- AGCTTTGAGCCTTCAGCATC

Ascl2: F- GCCTGACCAAATGCCAAGTG, R- ATTTCCAAGTCCTGATGCTGC

Bmp2: F- GAAGTTCCTCCACGGCTTC, R- AGATCTGTACCGCAGGCACT

Bmp7: F- ACGGACAGGGCTTCTCCTAC, R- ATGGTGGTATCGAGGGTGGAA

Cd81: F- ACACCTTCTACGTGGGCATC, R- TGCTTCACATCCTTGGCGAT

Grem1: F- TGGAGAGGAGGTGCTTGAGT, R- AACTTCTTGGGCTTGCAGAA

Frzb: F- TGCAAATGTAAGCCTGTCAGAGC, R- TCCACAACGGCGGTCACATC

Rspo3: F- ATGCACTTGCGACTGATTTCT, R- GCAGCCTTGACTGACATTAGGAT

Sfrp2: F- CGTGGGCTCTTCCTCTTCG, R- ATGTTCTGGTACTCGATGCCG

Sfrp4: F- GTGGCGTTCAAGGATGATGCTTC, R- TTACTGCGACTGGTGCGACTG

Pdgfra: F- GCAGTTGCCTTACGACTCCAGA, R- GGTTTGAGCATCTTCACAGCCAC

Foxl1: F- TCATCATGGATCGCTTCCCG, R- CCTCTTCCTGCGCCGATAAT

Actin: F- AAATCGTGCGTGACATCAAA, R- AAGGAAGGCTGGAAAAGAGC

In vitro coculture

As described above, lamina propria was isolated from mouse small intestine. The cells were resuspended in 100 µL of antibody mix (2% FBS; 1:125 CD45 (30-F11)-APC, BD Biosciences; 1:125 EPCAM (G8.8)-PE-Cy7, BioLegend; 1:125 PDGFRA (APA5)-BV421, Biolegend; 1:125 CD81 (Eat-2)-PE, BioLegend) and incubated for 1h on ice. The cells were then washed with 3 mL of 2% FBS in PBS and filtered once more. After centrifugation at 300 *g* for 5 min, the cell pellets were resuspended in 1 mL of 2% FBS and 10 U/mL DNAse in PBS for sorting. 8×10^4 sorted STC1 (CD81- $PDGFRA^{lo}$ EPCAM- CD45-) or STC2 cells (CD81+ $PDGFRA^{lo}$ EPCAM- CD45-) were cultured in 48-well plate in 20 µl of Matrigel together with 3×10^4 EGFP+ ISCs sorted from *Lgr5-EGFP-IRES-CreERT2* mice. Niche factor-reduced medium (-Nog $Rspo^{low}$, described above) was supplemented to test supporting function of the mesenchymal cells on organoid formation. Organoids were imaged using an EVOS M7000 microscope (Thermo Scientific).

Confocal imaging and quantification

Mouse small intestine samples were prepared for confocal microscopy as described above. Confocal imaging was performed with a Leica SP5 TCS confocal microscope. The argon laser intensity was set to 20% and Z-step size was set to 2 µm. Laser scanning frequency was set to 400 Hz and the frame average was set to 3. Section images were processed and analyzed using ImageJ. Intestinal crypt bottoms were visualized under the confocal microscope and clone sizes were quantified at the niche border[18] (Z-step 8-10; 16-20 µm upward from the crypt base). To perform

reliable and consistent measurements, we set z-stack positions for each crypt by considering the first z-plane showing any epithelial cell as the z=0 position of individual crypts. The central angle of the clonal circular sector (**Extended Data Fig. 2f**) was determined by 3 points (P1: clone starting point, Pc: crypt center, P3: clone end point) on the crypt circumference. Only RFP+ clones (wild-type in *Confetti* mice, mutant in *Red2Onco* mice) or YFP+ clones (wild-type) were quantified. Wild-type clones in *Red2Onco* mice were grouped with respect to their proximity to crypts containing mutant clones (**Fig. 2**). Wild-type (YFP+) clones distant (3 crypt diameters or more) from crypts containing mutant clones were considered to be "remote" while YFP+ clones neighboring fixed mutant (RFP+) crypts were considered to be "proximate". In **Extended Data Fig. 4**, proximate wild-type clonal data from **Fig. 2** were reanalyzed and partitioned into two groups, "inner" and "outer", depending on whether the geometric center of the clones was positioned in the crypt half nearest to or furthest from the mutant crypt (**Extended Data Fig. 4c**). For quantification of crypt base columnar cells, either the nuclear morphology (**Extended Data Fig. 3i, 5a**) or overlap with Lgr5-GFP was used (**Fig. 3e,g**). Three-dimensional representations were created using Image J. The number of cells per crypt was counted in Z-stacks.

Crypt size and circularity measurement

As indicated in **Extended Data Fig. 5b**, for analysis of the circularity and area of individual crypts, thresholded images were generated by ImageJ. The regions of interest were then analyzed using the "Analyze Particles" function in ImageJ to obtain outlined images and measures of location, size and circularity of individual crypts. Circularity was defined as $4\pi \times (\text{area}/\text{perimeter}^2)$ so that unity represents a perfect circle and a figure <1 indicates a degree of distortion. For these analyses, the particle size was set to a lower limit of 400 pixels. The size limit corresponds to circular

particles of approximately 20 μm in diameter and was chosen to exclude cells in the lamina propria from the analysis.

Intestinal clonal dynamics in Red2Onco mice

To address the influence of oncogene expression on the clonal dynamics of mutant and wild-type crypts, we use an established statistical modeling approach used previously to study stem cell dynamics of the intestinal crypt under normal and perturbed conditions[17,38]. In this approach, quantitative features of the clonal data, including the time evolution of the average clone size (scored as fraction of the crypt circumference) and crypt fixation frequency, are fit against a statistical modeling scheme based on a minimal number of adjustable parameters. Best fit parameters are then obtained using a standard least-squares fitting approach. Details of the modeling framework, its justification, and the implementation of the statistical analysis are presented in the **Supplementary Theory**.

Single-cell RNA-seq data analysis

Data processing for scRNA-seq

The raw sequencing data from the 10X Genomics platform were processed using CellRanger (v2.1.1). CellRanger aligned reads, filtered empty dropouts and counted unique molecular identifiers (UMIs) to generate a count matrix. We used Ensembl GRCm38/mm10 (release 92) appended with the sequences for *tdimer2* (RFP) and *EYFP* as the reference genome for the read alignment. The filtration of empty droplets was also checked with the R package DropletUtils (v1.2.2). To filter out low quality cells, cells with less than 100 genes were removed. In addition, cells with mitochondrial proportions above 15% were also discarded from further analysis. Genes

expressed in less than 3 cells were removed. Basic statistics and QC metrics for all samples are included in Table S2. EYFP+ cells were considered to be wild-type epithelial cells in the intestinal crypts of *Confetti*, *Red2-Kras*^{G12D} and *Red2-PIK3CA*^{H1047R} animals, whereas EPCAM+ and EYFP- cells were considered to be mutant epithelial cells in the intestinal crypt. UMIs were normalised by a deconvolution method using the R package scran (v1.12.1)[86].

Dimension reduction and data visualisation

PCA combined with technical noise modeling was applied to the normalised data for dimension reduction, which was implemented by the denoisePCA() function in the R package scran. This denoise PCA doesn't strictly require explicit feature selection, such as highly variable genes. The data were then projected using two-dimensional Uniform Manifold Approximation and Projection (UMAP) or t-Distributed Stochastic Neighbor Embedding (t-SNE) with default parameter setting. The 7 biological replicates for the three conditions overlapped well with each other, implying a high level of reproducibility between replicates and statistical reliability of our analysis. The high reproducibility confirmed batch effects between different samples and conditions were negligible and batch effect correction was not necessary for further analysis (**Extended Data Fig. 6b**).

Data clustering and cluster annotation

Based on expression of marker genes such as *Epcam*, *Vim* and *Ptprc* (*Cd45*), all cells were split into three major categories of epithelial cells, mesenchymal cells and immune cells. For each category, we then performed clustering using a graph-based method. First, a shared nearest-neighbor graph was constructed using k nearest-neighbors of each cell (buildSNNGraph function in the R package scran). k was set to 6 for epithelial cells and to 10 for mesenchymal and immune

cells. In this graph, two cells were connected by an edge if they shared nearest-neighbors, with the edge weight determined by the highest average rank of the shared neighbors. Then the Walktrap method from the R package igraph (v1.2.4.1) (with steps = 4 as the default option) was used to identify densely connected communities that were considered to be cell clusters.

Cell clusters were annotated based on differentially expressed genes and known marker genes for cell types. To annotate epithelial cells of the intestinal crypts, we referred to marker genes for cell types used in a previous study[48]. If a few neighboring clusters in the dimension reduction spaces shared key expression patterns, they were merged into one cell type manually. Thus, we classified 33 clusters into 8 epithelial cell types (**Extended Data Fig. 6c,d**). As a result, we confirmed that the fractions of individual cell types in the *Confetti* control were comparable to those in previous reports[48,50,514]. The fractions were as follows: 29.6% for stem cells; 30.2% for TA cells, 11% for enterocyte progenitors; 5.3% for enterocytes; 3.6% for Paneth cells; 14.7% for goblet cells; 2.4% for tuft cells; 3.2% for enteroendocrine cells. We note that our stringent removal of the villus fraction during sample preparation is likely to explain the smaller fraction of enterocyte lineage cells that are found compared to other reports[48,50,51]. While annotating epithelial, mesenchymal, and immune cells we found that, out of a total of 21,183 cells, 1,400 cells (6.6%) had a very low number of genes, and showed ambiguous and promiscuous expression. We considered them to be pseudo-cells, possibly contaminated with ambient RNA floating in single-cell suspension, and they were removed from further analysis.

Statistical analysis of cell type composition

To detect compositional change of cell types, the number of each cell type was modeled as a random count variable using a Poisson process. The rate of detection was modeled using the total number of cells profiled in each condition (RFP+ or YFP+) of an animal as an offset variable, with the condition of each animal (*Confetti* or *Red2Onco*) used as a covariate. We fitted the model using the glm function in the R package stats (v3.6.0). The p-value for the significance of the effect due to oncogene expression was estimated using a likelihood ratio test on the regression coefficient.

To interpret the fractional change of stem and progenitor cells in **Fig. 4d**, it is important to note that the mutant stem cell fraction may not correlate straightforwardly with the increased division rate observed in *Red2-Kras*^{G12D} and *Red2-PIK3CA*^{H1047R} conditions (**Extended Data Fig. 3h,i**). If oncogene expression drives an increased rate of differentiation[26], an increase in mutant stem cell number may be outweighed by an increase in the abundance of their differentiating progenies, leading to a net reduction in the mutant stem cell fraction. It is likely that such changes in differentiation bias are responsible for the significant drop in the fraction of mutant stem cells, as observed in **Extended Data Fig. 6i,j, k** as well as **Fig. 4d**.

Analysis of priming toward differentiation

To understand the origin of the altered relative proportions of mutant and wild-type epithelial cell types of the *Red2Onco* mice, we calculated the degree of fate priming of stem cells and their progenitors using the R package FateID (v0.1.9)[87]. We first identified marker genes for each differentiated sub-lineage, including enterocytes, Paneth cells, goblet cells, Tuft cells and enteroendocrine cells. To this end, we analyzed single-cell RNA-seq data generated from small intestinal crypts in a previous study[48]. We identified highly expressed genes in each of the differentiated sub-lineages using the findMarkers function from the R package scran (FDR < 0.05).

As a result, the numbers of the marker genes for differentiated sub-lineages were as follows: 2,497 genes for enterocyte; 4,941 genes for goblet cells; 2494 genes for Paneth cells; 3,416 genes for Tuft cells; 4660 genes for enteroendocrine cells. Using the marker genes for differentiated sub-lineages, we then calculated the fate bias scores of all epithelial cells for each differentiated sub-lineage using two functions, reclassify and fateBias, of the FateID package with default parameter values. We considered the fate bias scores to be the degree of fate priming. Then the distribution of the priming scores for stem cells and their progenitors in the *Red2Onco* mice was compared with that from the *Confetti* control using the Kolmogorov-Smirnov test in GraphPad Prism 8.

Gene set enrichment analysis (GSEA)

Based on prior knowledge, we selected three major signaling pathways, WNT, BMP and NOTCH, that significantly affect the stem cell and differentiation potential of intestinal stem cells[2,36,54]. To define gene sets for the pathways, we curated and referred to previous studies where the pathways of interest were considered to be specifically altered in intestinal crypts. Specifically, as the gene set for the BMP pathway, we used 293 genes that were highly expressed in BMP4-treated Lgr5+ intestinal organoids[74]. As the gene set for the WNT pathway, we used 113 genes (MSigDB id M1428) that were highly expressed in the intestinal crypts of *Apc* KO mice[88]. As the gene set for the NOTCH pathway, we used 315 genes highly expressed in the intestinal crypts of Atoh1 KO mice as compared to DBZ-treated mice[89].

Using the manually curated gene sets, we performed gene set enrichment analysis using the R package AUCell (v1.6.1). To identify “active” cells with high enrichment scores, the distribution of the enrichment scores were fitted using the AUCell_exploreThresholds function of the R

package AUCell and the cut-off ("Global_k1" value) for the high enrichment scores was selected among those suggested by the AUCell_exploreThresholds function. The fraction of active cells above the cut-off for each pathway is as shown in **Fig. 4i** and **Extended Data Fig. 7l**.

It is known that overexpression of oncogenes can lead to cellular senescence and secretion of senescence-associated secretory phenotype (SASP) factors in mutant cells[90,91]. Based on this, we wondered whether SASP factors may be involved in mediating the crosstalk between mutant and neighboring wild-type epithelial cells. Using the same method as described above, we performed gene set enrichment analysis to check whether oncogene-induced senescence and secretion of SASP factors occurs in epithelial cells of *Red2-Kras*^{G12D} and *Red2-PIK3CA*^{H1047R}. We collected 15 gene sets related to cell senescence from MSigDB (https://www.gsea-msigdb.org/gsea/msigdb/index.jsp) and performed GSEA for mutant and WT epithelial cells for *Confetti*, *Red2-Kras*^{G12D} and *Red2-PIK3CA*^{H1047R} animals. As a result, we found no increase in the senescence signature of mutant epithelial cells compared to *Confetti* in the majority of GSEA tests (12 gene sets out of 15), as represented in an example of **Supplementary Table 3** where MSigDB id M27190 was used as a gene set. In addition, we performed GSEA for mutant and wild-type epithelial cells of *Red2Onco* mice using 25 genes as a SASP gene set from a previous study[90]. As a result, enrichment of SASP genes in mutant epithelial cells was observed in neither *Red2-Kras*^{G12D} nor *Red2-PIK3CA*^{H1047R} conditions (**Supplementary Table 3**), implying that oncogene-induced senescence is unlikely to be involved in mediating the crosstalk between mutant and neighboring wild-type epithelial cells in *Red2-Kras*^{G12D} and *Red2-PIK3CA*^{H1047R} animals.

To examine potential inflammation due to the high induction of oncogene expression, we performed GSEA analysis for immune cells for *Confetti, Red2-Kras*^{G12D} and *Red2-PIK3CA*^{H1047R} mice using gene sets related to inflammation-related biological processes. We collected 11 gene sets from previous reports and public databases: 5 gene sets from other literatures[92,93] reporting differentially expressed in genes in human and mouse ulcerative colitis; 3 gene sets (GO:0031663, 0070098, 0071347) from Gene Ontology Biological Process; 3 gene sets (hsa04670, hsa04672, hsa04660) from KEGG pathways. As a result, gene set enrichment analysis of immune cells did not reveal any clear evidence for inflammation in the niche environment of the intestinal crypts in *Red2-Kras*^{G12D} and *Red2-PIK3CA*^{H1047R} mice, as represented in examples of **Supplementary Table 3**.

See **Supplementary Table 3** for the details of the gene sets used in **Fig. 4** and **Extended Data Fig. 7**.

Estimating degree of transcriptomic change

To estimate the degree of transcriptomic change for mesenchymal and immune cells, for each cell type we tested the statistical significance of the distance between the cell clusters in the *Confetti* and *Red2Onco* mice using two different methods:

In the first method, statistical significance was estimated based on how much larger inter-variability between cell clusters is than intra-variability. To this end, we defined cell-to-cell variability as 1 – (Pearson correlation) for any pair of cells. If two cells from the same model (either the *Confetti* control or *Red2Onco* mice) are selected, the cell-to-cell variability was

considered to be the intra-variability. On the other hand, if one cell is selected from the *Confetti* control and the other from a *Red2Onco* mice to form a pair, the cell-to-cell variability was considered to be the inter-variability. The dispersion and mean of the distributions of the inter-variability and intra-variability was summarised in the form of a t-statistic. To make a null hypothesis distribution for this statistic, we randomly sampled cells for each cell type and formed 'pseudo-confetti' and 'pseudo-Red2' samples, before calculating the t-statistics for the variability; this was repeated 20,000 times and generated an empirical null hypothesis distribution of the statistics. The significance of larger inter-variability than intra-variability was tested against this null hypothesis distribution, generating a p-value, P_{VAR}.

In the second approach, we used Augur, a method to rank cell types based on their degree of response to biological perturbations in single-cell data[94]. Augur employs a machine-learning framework to quantify the separability of perturbed and unperturbed cells within a high-dimensional space of single-cell measurements. To feed our dataset to Augur workflow, the *Confetti* cells were randomly selected and split into two groups, *Confetti* set A and B, for each cell type. Then condition-specific AUC values for each cell type were calculated by comparing *Confetti* set A vs. *Red2Onco* mice and *Confetti* set A vs. B using the calculate_auc function with subsample_size=6 and default values for other parameters. To calculate the null distribution of AUCs for each cell type and condition, calculate_auc function was executed again for *Confetti* set A vs. *Red2Onco* mice and for *Confetti* set A vs. B with subsample_size=6, augur_mode="permute", and default values for other parameters. Using the condition-specific AUCs and their null distributions, the statistical significance of differential prioritization between *Confetti* set A vs. *Red2Onco* mice and *Confetti* set A vs. B was calculated by running

calculate_differential_prioritization function with default parameter values. To guarantee robustness of our results, we repeated 50 times the random splitting of the *Confetti* cells followed by the calculation of the statistical significance of the differential prioritization, and chose the median p-values as the representative ones (P_{AUGUR}) for each cell type and condition. P_{VAR} and P_{AUGUR} for each cell type were compared, as shown in **Fig. 5e** for mesenchymal cells and **Fig. 5f** for immune cells.

Gene ontology analysis

Differentially expressed genes in the stromal cell STC2 cluster compared to other mesenchymal cell types were identified using the findMarkers function from the R package scran. 377 genes with p-value < 0.05 and absolute value of $\log_2$(fold-change) > α, where α is the 95th percentile of all $\log_2$(fold-change), were selected for gene ontology analysis. The gene ontology analysis was performed using DAVID (https://david.ncifcrf.gov/)[95].

Statistical analysis

GraphPad Prism 8 software was used to perform statistical analyses. Unless otherwise specified, statistical significance was determined by applying the Student *t* test or analysis of variance (ANOVA) to raw values from at least 3 independent experiments. No statistical methods were used to predetermine sample size. No method of randomization was followed and no animals were excluded from this study. The investigators were not blinded to sample allocation during the experiments and assessment of results.

Data Availability

The single-cell RNA-seq data have been deposited in ArrayExpress under E-MTAB-8656.

Code Availability

The statistical analysis of the clone fate data based on the established modeling scheme was performed using a FORTRAN code developed for this study. The single-cell RNA-seq data was analyzed using publicly available R packages. The codes will be made available from the corresponding authors on reasonable request.

Method references

79 Kinross, K. M. *et al.* An activating Pik3ca mutation coupled with Pten loss is sufficient to initiate ovarian tumorigenesis in mice. *J Clin Invest* **122**, 553-557, doi:10.1172/JCI59309 (2012).

80 Murtaugh, L. C., Stanger, B. Z., Kwan, K. M. & Melton, D. A. Notch signaling controls multiple steps of pancreatic differentiation. *Proc Natl Acad Sci U S A* **100**, 14920-14925, doi:10.1073/pnas.2436557100 (2003).

81 Orsulic, S. *et al.* Induction of ovarian cancer by defined multiple genetic changes in a mouse model system. *Cancer Cell* **1**, 53-62, doi:10.1016/s1535-6108(01)00002-2 (2002).

82 Zhao, J. J. *et al.* The oncogenic properties of mutant p110alpha and p110beta phosphatidylinositol 3-kinases in human mammary epithelial cells. *Proc Natl Acad Sci U S A* **102**, 18443-18448, doi:10.1073/pnas.0508988102 (2005).

83 Susaki, E. A. *et al.* Advanced CUBIC protocols for whole-brain and whole-body clearing and imaging. *Nat Protoc* **10**, 1709-1727, doi:10.1038/nprot.2015.085 (2015).

84 Snippert, H. J., Schepers, A. G., Delconte, G., Siersema, P. D. & Clevers, H. Slide preparation for single-cell-resolution imaging of fluorescent proteins in their three-dimensional near-native environment. *Nat Protoc* **6**, 1221-1228, doi:10.1038/nprot.2011.365 (2011).

85 Stzepourginski, I., Eberl, G. & Peduto, L. An optimized protocol for isolating lymphoid stromal cells from the intestinal lamina propria. *J Immunol Methods* **421**, 14-19, doi:10.1016/j.jim.2014.11.013 (2015).

86 Lun, A. T., Bach, K. & Marioni, J. C. Pooling across cells to normalize single-cell RNA sequencing data with many zero counts. *Genome Biol* **17**, 75, doi:10.1186/s13059-016-0947-7 (2016).

87 Herman, J. S., Sagar & Grun, D. FateID infers cell fate bias in multipotent progenitors from single-cell RNA-seq data. *Nat Methods* **15**, 379-386, doi:10.1038/nmeth.4662 (2018).

88 Sansom, O. J. *et al.* Myc deletion rescues Apc deficiency in the small intestine. *Nature* **446**, 676-679, doi:10.1038/nature05674 (2007).

89 Kim, T. H. *et al.* Broadly permissive intestinal chromatin underlies lateral inhibition and cell plasticity. *Nature* **506**, 511-515, doi:10.1038/nature12903 (2014).

90 Coppe, J. P. *et al.* Senescence-associated secretory phenotypes reveal cell-nonautonomous functions of oncogenic RAS and the p53 tumor suppressor. *PLoS Biol* **6**, 2853-2868, doi:10.1371/journal.pbio.0060301 (2008).

91 Coppe, J. P., Desprez, P. Y., Krtolica, A. & Campisi, J. The senescence-associated secretory phenotype: the dark side of tumor suppression. *Annu Rev Pathol* **5**, 99-118, doi:10.1146/annurev-pathol-121808-102144 (2010).

92 Czarnewski, P. *et al.* Conserved transcriptomic profile between mouse and human colitis allows unsupervised patient stratification. *Nat Commun* **10**, 2892, doi:10.1038/s41467-019-10769-x (2019).

93 Haberman, Y. *et al.* Ulcerative colitis mucosal transcriptomes reveal mitochondriopathy and personalized mechanisms underlying disease severity and treatment response. *Nat Commun* **10**, 38, doi:10.1038/s41467-018-07841-3 (2019).

94 Skinnider, M. A. *et al.* Cell type prioritization in single-cell data. *Nat Biotechnol* **39**, 30-34, doi:10.1038/s41587-020-0605-1 (2021).

95 Huang da, W., Sherman, B. T. & Lempicki, R. A. Systematic and integrative analysis of large gene lists using DAVID bioinformatics resources. *Nat Protoc* **4**, 44-57, doi:10.1038/nprot.2008.211 (2009).

Acknowledgements

We thank Stoyana Alexandrova and members of the Simons lab for valuable discussions, Dr. Christopher J. Hindley for critical reading of the manuscript and Sung-hwan Bae for graphic illustration. This work was supported by a CRUK Multidisciplinary Project Award to B.-K.K. and B.D.S. (C52767/A23363), as well as by studentships and fellowships to J.F. (Wellcome Trust), S.H. (HFSP LT000092/2016-L; Basic Science Research Program NRF-2014R1A6A3A01005675) and B.D.S. (Royal Society EP Abraham Research Professorship, RP\R1\180165), and grants to A.P. (Cancer Research UK grant A25636), B.-K.K. (ERC starting grant, Troy Stem Cells, 639050; the Austrian Academy of Sciences; Human Frontier Science Program; Interpark Bio-Convergence Center Grant Program) and B.D.S. (Wellcome Trust 098357/Z/12/Z). The research team also acknowledges core grant support from the Wellcome Trust and MRC to the WT–MRC Cambridge Stem Cell Institute, and to the Gurdon Institute from the Wellcome Trust (092096) and CRUK (C6946/A14492).

Author contributions

M.K.Y., S.H., J.F., B.D.S. and B.-K.K. designed the experiments. M.K.Y., S.H., J.F., C.D., T.T., S.W., R.M., L.C., R.A., I.P., F.E., D.E.S., and B.-K.K. performed animal experiments, tissue imaging and quantification, which were supervised by A.P., J-H.L., B.-K.K. and B.D.S. B.D.S.

analyzed clonal data, devised the biophysical model and performed stochastic simulations of clonal dynamics. S.H., M.K.Y., E.L., J.K.K., B.D.S., and B.-K.K. analyzed single-cell RNA-seq data. M.K.Y., S.H., B.-K.K. and B.D.S. wrote the manuscript.

Declaration of Interests

The authors declare no competing interests.

Supplementary information

Supplementary Video. Whole mount z-stack imaging of *Villin-CreERT2*; *Red2-KrasG12D* small intestine, Related to Figure 1

Supplementary Theory. Related to Figure 2, 3 and Extended Data Figure 2,3,4

Supplementary Table 1. Clone data statistical analyses, Related to Figure 2 and Extended Data Figure 2,4.

Supplementary Table 2. Cell type markers and differentially expressed genes of epithelial cells, Related to Figure 4

Supplementary Table 3. Gene sets for evaluating stem cell priming and Gene set enrichment analysis (GSEA) on BMP, WNT and NOTCH signaling pathways, Related to Figure 4 and Extended Data Figure 7

Supplementary Table 4. Cell type markers and differentially expressed genes of mesenchymal and immune cells, Related to Figure 5

Supplementary Table 5. Expressed ligands list for BMP and WNT signaling pathways, Related to Figure 5

Correspondence and requests for materials should be addressed to Benjamin D. Simons (bds10@cam.ac.uk) and Bon-Kyoung Koo (bonkyoung.koo@imba.oeaw.ac.at).

Figure 1

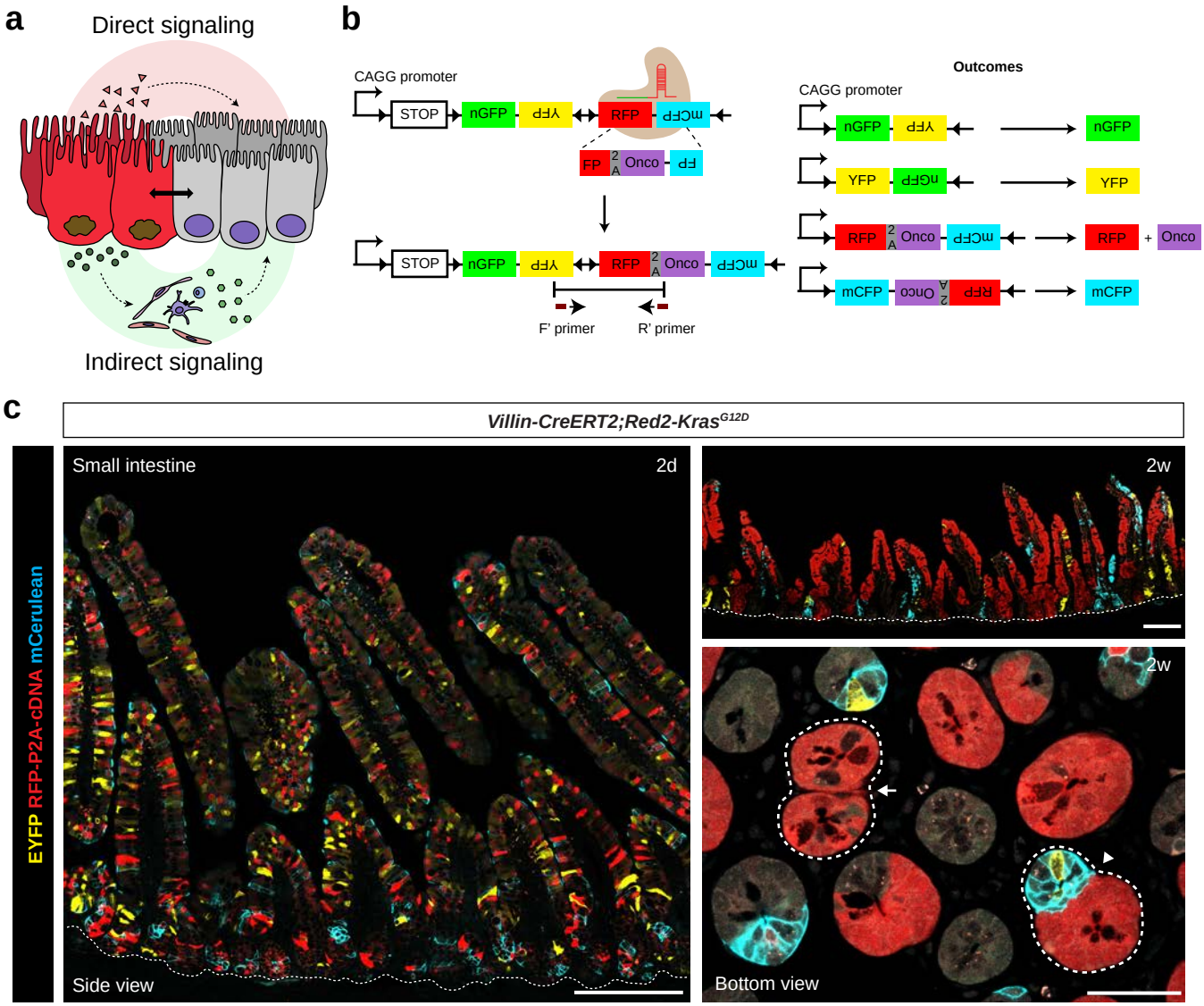
a
Direct signaling
Indirect signaling
b
CAGG promoter
STOP
nGFP
YFP
RFP
mCFP
FP
2A
Onco
F' primer
R' primer
Outcomes
YFP
mGFP
mCFP
+
c
Villin-CreERT2;Red2-Kras^G12D
EYFP RFP-P2A-cDNA mCerulean
Small intestine
2d
Side view
2w
Bottom view

Figure 1. Red2Onco system: an oncogene-associated multicolor reporter

a, Schematic illustration of possible routes for crosstalk between mutant and neighboring wild-type cells.

b, *Red2Onco* knock-in strategy. The 2A peptide sequence and oncogene cDNA (*Kras*^{G12D}, *PIK3CA*^{H1047R} or *Notch1ICD*) were cloned in-frame downstream of the *RFP* cDNA in the *R26R-Confetti* cassette[24], which encodes 4 fluorescent proteins.

c, Representative images from 100 µm-thick sections (left and upper right panel) or whole mounts (lower right panel) of small intestine from *Villin-CreERT2; Red2-Kras*^{G12D} mice at 2 days (d) or 2 weeks (w) post-tamoxifen administration. The white dashed line indicates the mucosal lining. In the lower right image, crypt fission and fusion event are visible, and indicated by a white arrow and arrowhead, respectively. Yellow: EYFP; Red: tdimer2 (RFP); Cyan: mCerulean. Scale bar: 200 µm for side views, 50 µm for bottom view.

Figure 2

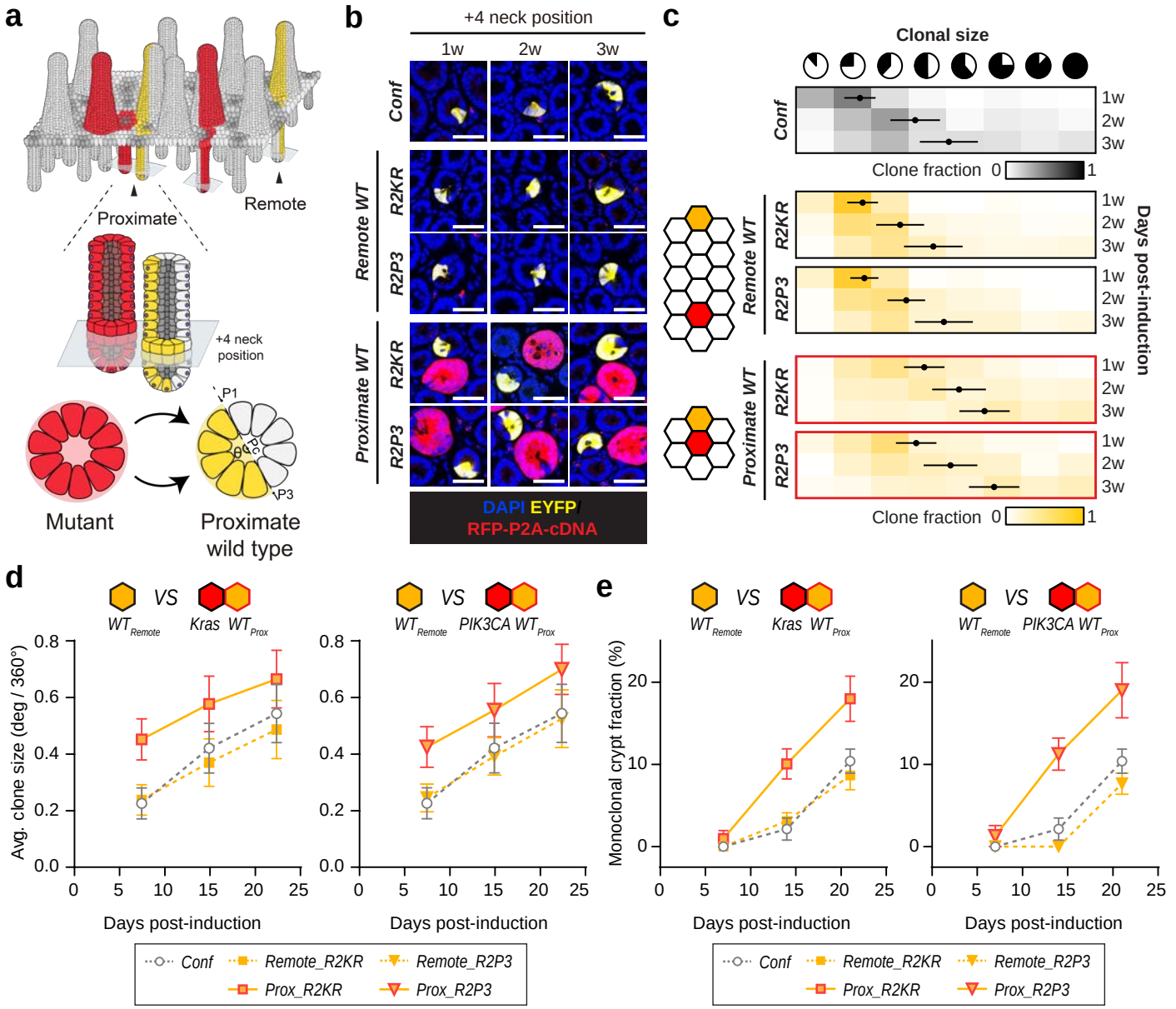
a
Remote
Proximate
+4 neck position
P1
P2
P3
Mutant
Proximate wild type
b
+4 neck position
1w
2w
3w
Conf
Remote WT
R2KR
R2P3
Proximate WT
DAPI EYFP
RFP-P2A-cDNA
c
Clonal size
Clone fraction 0 1
Days post-induction
d
VS
WT Remote
Kras WT Prox
PIK3CA WT Prox
Avg. clone size (deg / 360°)
Days post-induction
e
Monoclonal crypt fraction (%)
Conf
Remote_R2KR
Remote_R2P3
Prox_R2KR
Prox_R2P3

Figure 2. Mutant crypts perturb clonal dynamics of wild-type cells in neighboring crypts

a, Schematic illustration of a wild-type (YFP+) clone in proximity to a fixed mutant crypt (RFP+). Clone sizes quantified as in Extended Data Fig. 2f.

b, Representative confocal images of wild-type (WT; YFP+) clones remote from or proximate to fixed mutant crypts in whole mount small intestine from *Villin-CreERT2;R26R-Confetti* or *Red2Onco* mice at 1w, 2w and 3w post-tamoxifen administration. Conf: *R26R-Confetti*; R2N1: *Red2-Notch1ICD*; R2KR: *Red2-Kras*^{G12D}; R2P3: *Red2-PIK3CA*^{H1047R}. Scale bar: 50 μm.

c, Heat maps indicate the relative clone fractions of the indicated sizes (columns) at various time points post-induction (rows). Black dots denote mean ± SEM. $N = 6$ mice for each group and time point. For each condition, >50 clones were scored. Remote WT: wild-type clones located in crypts separated by >3 crypt diameters from mutant crypts. Proximate WT: wild-type clones located in crypts neighboring fixed mutant crypts.

d, e, Average clone size (**d**) and percentage of monoclonal crypts (**e**) of remote (Remote_R2KR or Remote_R2P3) and proximate (Prox_R2KR or Prox_R2P3) wild-type (YFP+) clones at different time points after tamoxifen administration. Data are presented as mean ± SEM. $N = 6$ mice for each group and time point. For each condition, >50 clones were scored. Grey circles and dashed line: clones from *R26R-Confetti* control; yellow symbols and dashed line: remote wild-type clones from *Red2Onco* mice; symbols with red outline and yellow line: proximate wild-type clones from *Red2Onco* mice.

R26R-Confetti and remote wild-type control data from Extended Data Fig. 2f are reproduced for comparison in heat maps (**c**) and graphs (**d** and **e**).

Figure 3

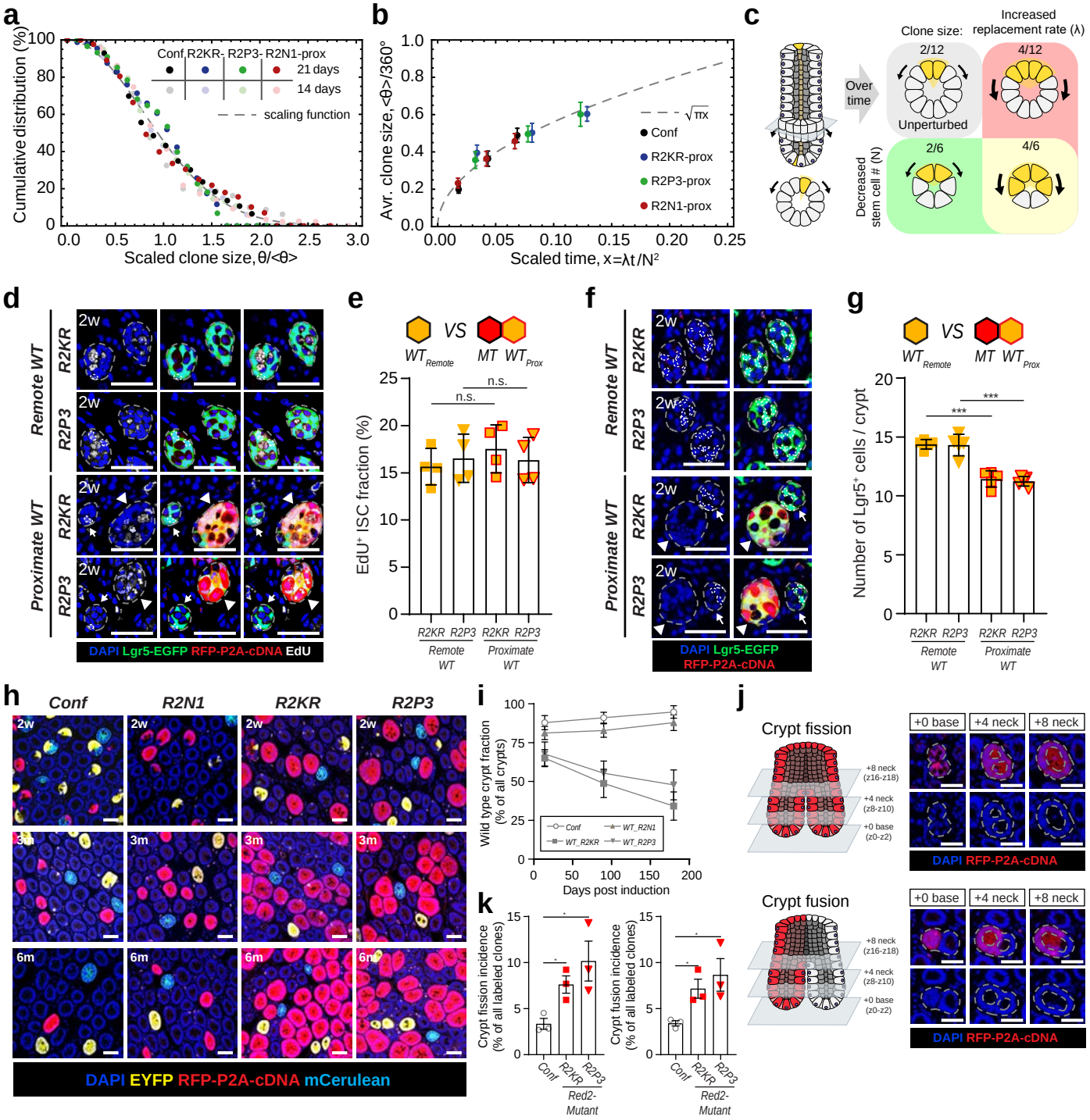
a
Cumulative distribution (%)
Conf R2KR- R2P3- R2N1-prox
21 days
14 days
scaling function
Scaled clone size, θ/<θ>
b
Avr. clone size, <Θ>/360°
√πx
Conf
R2KR-prox
R2P3-prox
R2N1-prox
Scaled time, x=λt/N²
c
Over time
Clone size:
Increased replacement rate (λ)
2/12
4/12
Unperturbed
2/6
4/6
Decreased stem cell # (N)
d
Remote WT
Proximate WT
R2KR
R2P3
2w
DAPI Lgr5-EGFP RFP-P2A-cDNA EdU
e
VS
WT Remote
MT
WT Prox
n.s.
EdU⁺ ISC fraction (%)
R2KR R2P3 R2KR R2P3
Remote WT
Proximate WT
f
DAPI Lgr5-EGFP RFP-P2A-cDNA
g
Number of Lgr5⁺ cells / crypt
***
h
Conf
R2N1
R2KR
R2P3
3m
6m
DAPI EYFP RFP-P2A-cDNA mCerulean
i
Wild type crypt fraction (% of all crypts)
Conf
WT_R2N1
WT_R2KR
WT_R2P3
Days post induction
j
Crypt fission
Crypt fusion
+8 neck (z16-z18)
+4 neck (z8-z10)
+0 base (z0-z2)
+0 base
+4 neck
+8 neck
DAPI RFP-P2A-cDNA
k
Crypt fission incidence (% of all labeled clones)
Crypt fusion incidence (% of all labeled clones)
Conf
R2KR
R2P3
Red2-Mutant

Figure 3. Reduced effective stem cell number leads to accelerated drift dynamics of wild-type clones in crypts neighboring mutant crypts

a, Cumulative size distribution of wild-type (YFP+) clones in crypts neighbouring crypts monoclonal for the given mutant together with Confetti control plotted against the angular clone size, θ, rescaled by the average, $\langle\theta\rangle$. Points show data from 2 time points and dashed line denotes parameter-independent scaling function predicted by neutral drift model (see main text and Supplementary Theory). *N*=6 mice for each group and time point. For each condition, >50 clones were scored. Conf: *R26R-Confetti*; R2N1: *Red2-Notch1ICD*; R2KR: *Red2-Kras*^{G12D}; R2P3: *Red2-PIK3CA*^{H1047R}.

b, Average clone size $\langle\theta\rangle/360^{o}$ of wild-type (YFP+) clones in crypts neighbouring crypts monoclonal for the given mutant together with Confetti control plotted as a function of time t post-induction scaled by the corresponding drift rates, $\Lambda \equiv \lambda/N^2$ (key as in a). Drift rates are obtained from a fit of the average clone size to the square root dependence (dashed line) predicted by the neutral drift model (Extended Data Fig. 4f and Supplementary Theory). Data presented as mean ± SEM.

c, Schematic of factors affecting rate of clonal drift. In the neutral drift model, an increased rate of stem cell loss-and-replacement or a decrease in the effective stem cell number leads to faster clonal drift around the crypt circumference (see Supplementary Theory).

d, e, Representative confocal images (**d**) and quantification (**e**) of EdU+ proliferating (Lgr5+) stem cells in wild-type crypts neighboring mutant crypts in whole mount small intestine from *Lgr5-EGFP-IRES-CreERT2;Red2Onco* mice at 2w post-tamoxifen administration. Data are presented as mean ± SD. *N* = 5 mice for each group. For each mouse, >100 crypts were analysed. p-values from unpaired t-test: n.s., statistically not significant (p > 0.1). Scale bar: 50 µm.

f, g, Representative confocal images (**f**) and quantification (**g**) of EGFP+ (Lgr5+) stem cells in whole mount small intestine from *Lgr5-EGFP-IRES-CreERT2;Red2Onco* mice at 2w post-tamoxifen administration. Proximate wild-type crypts and fixed mutant crypts are indicated by white arrows and arrowheads, respectively. Crypt borders are marked by dashed grey outlines. EGFP+ cells in wild-type crypts are outlined with a white dashed line. Data are presented as mean ± SD. *N* = 5 mice for each group. For each mouse, >100 crypts were analysed. p-values from unpaired t-test: ***, p < 1e-4. Scale bar: 50 µm.

h, Representative confocal images of whole mount small intestine from *Villin-CreERT2;R26R-Confetti* or *Red2Onco* mice at 2 weeks (2w), 3 months (3m) and 6 months (6m) post-tamoxifen administration. Conf: *R26R-Confetti*; R2N1: *Red2-Notch1ICD*; R2KR: *Red2-Kras*^{G12D}; R2P3: *Red2-PIK3CA*^{H1047R}. Scale bar: 50 µm.

i, Fractions of wild-type crypts from a single field of image (0.15 mm^2). Grey circles and line: *R26R-Confetti* control; Grey symbols and lines: wild-type (WT) crypts in *Red2Onco* mice. Data are presented as mean ± SD. N = 3 mice for each group. >10 images were analysed per mouse. Conf: *R26R-Confetti*; R2N1: *Red2-Notch1ICD*; R2KR: *Red2-Kras*^{G12D}; R2P3: *Red2-PIK3CA*^{H1047R}.

j, Schematic illustration (left) and representative images (right) of a crypt fission and fusion event in '8-shaped crypts'. Crypt borders are marked by dashed grey outlines. Scale bar: 50 µm.

k, Percentage of crypts undergoing crypt fission (left) or crypt fusion (right) (670 crypts for *R26R-Confetti*, 452 crypts for *Red2-Kras*^{G12D}, and 457 crypts for *Red2-PIK3CA*^{H1047R}). Data are presented as mean ± SEM. N = 3 mice for each group. >10 images were analysed per mouse. p-values from unpaired t-test: *, p < 0.05 Conf: *R26R-Confetti*; R2N1: *Red2-Notch1ICD*; R2KR: *Red2-Kras*^{G12D}; R2P3: *Red2-PIK3CA*^{H1047R}.

Figure 4

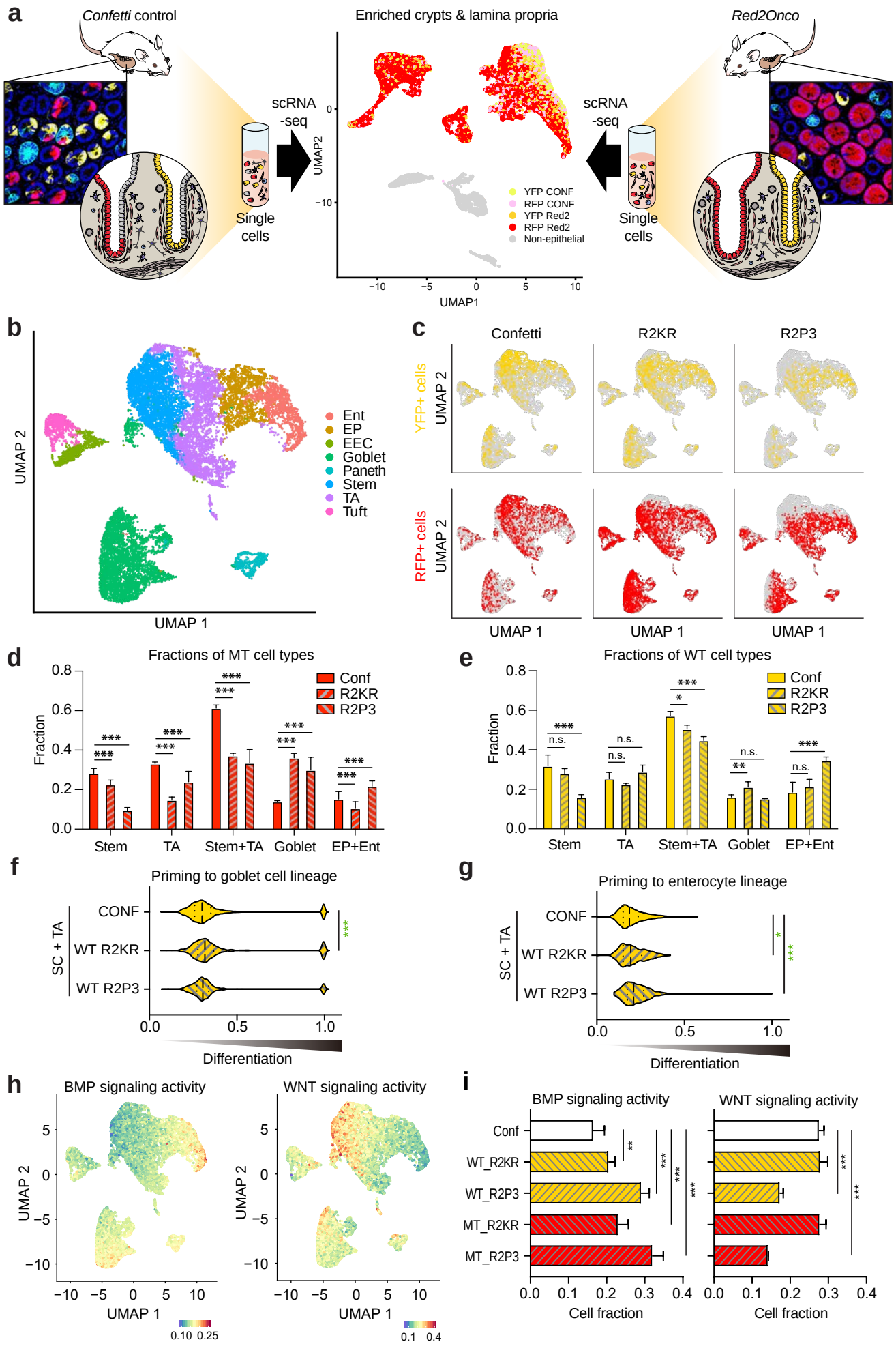
a
Confetti control
Enriched crypts & lamina propria
Red2Onco
scRNA -seq
Single cells
UMAP2
UMAP1
YFP CONF
RFP CONF
YFP Red2
RFP Red2
Non-epithelial
b
UMAP 2
UMAP 1
Ent
EP
EEC
Goblet
Paneth
Stem
TA
Tuft
c
Confetti
R2KR
R2P3
YFP+ cells
RFP+ cells
UMAP 2
UMAP 1
d
Fractions of MT cell types
Fraction
Conf
R2KR
R2P3
Stem
TA
Stem+TA
Goblet
EP+Ent
e
Fractions of WT cell types
f
Priming to goblet cell lineage
SC + TA
CONF
WT R2KR
WT R2P3
Differentiation
g
Priming to enterocyte lineage
h
BMP signaling activity
WNT signaling activity
i
Cell fraction
Conf
WT_R2KR
WT_R2P3
MT_R2KR
MT_R2P3

Figure 4. Comparative single-cell transcriptomic analysis identifies oncogene-driven changes in signaling pathways

a, Schematic illustration of comparative single-cell analysis using the Red2Onco system. Mutant and wild-type epithelial cells, together with niche cells including mesenchymal and immune cells, were isolated from individual animals and compared with *Confetti* control animals. By comparing the gene expression profiles of cells from all models, the effect of oncogene expression on mutant and neighboring wild-type epithelial cells, as well as the surrounding environment, can be resolved.

b, UMAP showing the clustering of epithelial cells from the intestinal crypts of *Red2-Kras*^{G12D}, *Red2-PIK3CA*^{H1047R} and *Confetti* control animals. Based on marker gene expression, epithelial cells were classified into 8 cell types: stem cells (Stem), TA cells (TA), enterocyte progenitors (EP), enterocyte (Ent), enteroendocrine cells (EEC), goblet cells (Goblet), Paneth cells (Paneth), and tuft cells (Tuft).

c, UMAPs showing the distribution of mutant (RFP+) and wild-type (YFP+) epithelial cells for each of the *Confetti*, *Red2-Kras*^{G12D} (R2KR) and *Red2-PIK3CA*^{H1047R} (R2P3) models. Mutant and wild-type epithelial cells from all models are spread throughout all clusters, indicating that batch effects are minimal and providing the basis for comparative analysis between conditions.

d, e, Fractions of cell types for mutant (**d**) and wild-type epithelial cells (**e**) in the *Red2Onco* models and the *Confetti* control. The fraction of each cell type was calculated by taking the number of that cell type normalised by the total number of cells for each animal. Data are presented as mean ± SEM. p-values from likelihood ratio test: *, $p < 0.05$; **, $p < 0.01$; ***, $p < 1e\text{-}4$; n.s., statistically not significant ($p > 0.05$).

f, g, Priming scores of wild-type (YFP+) stem cells and TA cells toward goblet (**f**) and enterocyte (**g**) lineages in the *Red2Onco* models and *Confetti* control. Higher priming scores were observed in wild-type cells from both *Red2Onco* models compared to those of the *Confetti* control. 25th and 75th percentile values are denoted with thin black dotted lines and 50th percentile value with thick black dotted line. p-values from Kolmogorov–Smirnov test: *, $p < 0.05$; ***, $p < 1e\text{-}4$. Green asterisk: higher in *Red2Onco* models compared to the *Confetti* control.

h, UMAPs showing the distribution of gene set enrichment scores for BMP (left) and WNT (right) pathways. BMP pathway scores are enriched toward differentiated cells, whereas WNT pathway scores are enriched toward stem cells. Color bars indicate the enrichment scores.

i, Fractions of "active" cells with high gene set enrichment scores for BMP (left) and WNT (right) pathways in mutant (MT) and wild-type (WT) epithelial cells from the *Red2Onco* models and *Confetti* control. The fraction of BMP pathway active cells increased in mutant and wild-type cells of both *Red2Onco* models relative to the *Confetti* control. The fraction of WNT pathway active cells decreased in mutant and wild-type cells of the *Red2-PIK3CA*^{H1047R} model relative to the *Confetti* control. Conf: *R26R-Confetti*; R2KR: *Red2-Kras*^{G12D}; R2P3: *Red2-PIK3CA*^{H1047R}. Data are presented as mean ± SEM. p-values from likelihood ratio test: **, $p < 0.01$; ***, $p < 1e\text{-}4$.

Figure 5

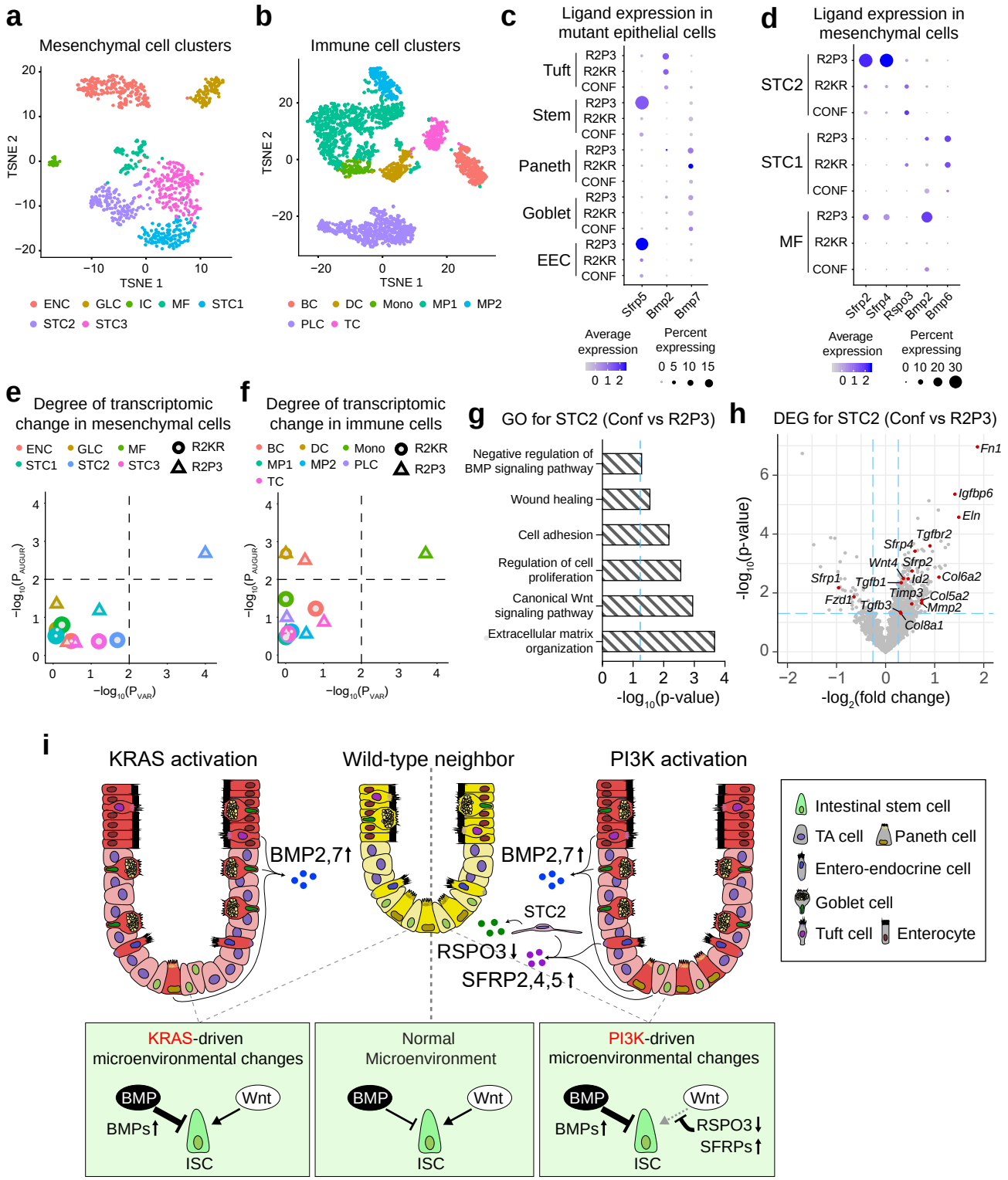
a
Mesenchymal cell clusters
TSNE 2
TSNE 1
ENC GLC IC MF STC1
STC2 STC3
b
Immune cell clusters
BC DC Mono MP1 MP2
PLC TC
c
Ligand expression in mutant epithelial cells
Tuft Stem Paneth Goblet EEC
R2P3 R2KR CONF
Sfrp5 Bmp2 Bmp7
Average expression
Percent expressing
d
Ligand expression in mesenchymal cells
STC2 STC1 MF
Sfrp2 Sfrp4 Rspo3 Bmp2 Bmp6
e
Degree of transcriptomic change in mesenchymal cells
f
Degree of transcriptomic change in immune cells
g
GO for STC2 (Conf vs R2P3)
Negative regulation of BMP signaling pathway
Wound healing
Cell adhesion
Regulation of cell proliferation
Canonical Wnt signaling pathway
Extracellular matrix organization
h
DEG for STC2 (Conf vs R2P3)
Fn1 Igfbp6 Eln Tgfbr2 Sfrp4 Wnt4 Sfrp2 Sfrp1 Tgfb1 Id2 Col6a2 Timp3 Col5a2 Fzd1 Tgfb3 Mmp2 Col8a1
i
KRAS activation
Wild-type neighbor
PI3K activation
BMP2,7↑
STC2
RSPO3↓
SFRP2,4,5↑
Intestinal stem cell
TA cell
Paneth cell
Entero-endocrine cell
Goblet cell
Tuft cell
Enterocyte
KRAS-driven microenvironmental changes
Normal Microenvironment
PI3K-driven microenvironmental changes
BMP
Wnt
BMPs↑
RSPO3↓
SFRPs↑
ISC

Figure 5. Mutant clones drive niche remodeling

a, b, t-SNE plots representing the clustering of mesenchymal (**a**) and immune (**b**) cells from *Red2-Kras*^{G12D} and *Red2-PIK3CA*^{H1047R} models as well as *Confetti* control. Based on marker gene expression, 7 cell types were identified in both mesenchymal and immune cell populations. ENC: endothelial cell; GLC: glial cell; IC: interstitial cell of Cajal; MF: myofibroblast; STC1, STC2, STC3: stromal cell 1, 2, 3; BC: B-cell; DC: dendritic cell; Mono: monocyte; MP1, 2: macrophage 1, 2; PLC: plasma cell; TC: T-cell.

c, d, Dot plots showing expression of secreted factors that are known to modulate BMP and WNT signaling in mutant epithelial cells from the *Red2Onco* models and wild-type cells from the *Confetti* control (**c**) and in mesenchymal cells of these models (**d**). The size of the dot denotes the percentage of cells expressing a given gene for that cell type and model, while the color denotes the average expression of the gene across all cells of that cell type in a given model. R2P3: *Red2-PIK3CA*^{H1047R}; R2KR: *Red2-Kras*^{G12D}; CONF: *R26R-Confetti*.

e, f, The degree of transcriptomic change estimated by two independent measures for each cell type of the mesenchymal (**e**) and immune (**f**) populations. One measure is based on cell-to-cell variability at the transcriptomic level, and another based on the separability of perturbed and unperturbed cells (see Methods for details). Based on the two measures, we performed statistical tests on how different each cell type of the *Red2Onco* mice is from that of the *Confetti* control at the level of the transcriptome. -$\log_{10}$-transformed p-values from the two tests are displayed along the x-axis (P_{VAR} = p-value for cell-to-cell variability test) and y-axis (P_{AUGAR} = p-value for separability test of perturbed and unperturbed cells). Note that P_{AUGUR} is not calculated for interstitial cell of Cajal (IC) in *Red2-Kras*^{G12D} and *Red2-PIK3CA*^{H1047R} and myofibroblast (MF) in *Red2-PIK3CA*^{H1047R} as their cell numbers are not sufficient to apply the Augur algorithm. Both tests show that the stromal STC2 cell population consistently underwent a statistically significant change in transcription. The dotted lines indicate -$\log_{10}$(0.01) as the cut-off for statistical significance of the p-values. The colors of the data points denote distinct cell types after the legends of (**a**) and (**b**). Circles and triangles denote cells from the *Red2-Kras*^{G12D} (R2KR) and *Red2-PIK3CA*^{H1047R} (R2P3) models, respectively.

g, Enriched biological processes from gene ontology (GO) analysis of differentially expressed genes in the STC2 population of the *Red2-PIK3CA*^{H1047R} model relative to those of the *Confetti* control. The dotted line represents 0.05 as the threshold for significance of the p-value.

h, Volcano plot representing differentially expressed genes in the STC2 population of the *Red2-PIK3CA*^{H1047R} model relative to that of the *Confetti* control. The $\log_2$-fold change in gene expression is displayed on the x-axis and the -$\log_{10}$-transformed p-value on the y-axis. Grey dots denote individual genes and red dots denote genes known to be involved in the enriched biological processes of (**g**). The vertical dotted lines indicate $\log_2$(fold-change) = 0.259, 95th percentile of absolute values of $\log_2$(fold-change). The horizontal dotted line represents -$\log_{10}$(0.05) as the threshold for differential expression using a pairwise t-test.

i, Schematic model of the crosstalk between mutant and wild-type crypts in *Red2-Kras*^{G12D} and *Red2-PIK3CA*^{H1047R} models upon oncogene expression, mediated directly or indirectly through niche environments. Overexpression of mutant KRAS or PI3K leads to an increase in BMP pathway agonists (e.g. BMP2 and BMP7) in the shared niche environment, while overexpression of mutant PI3K also results in a decrease in WNT pathway agonists (e.g. RSPO3) and increase in antagonists (e.g. SFRP2, SFRP4 and SFRP5).

Figure 6

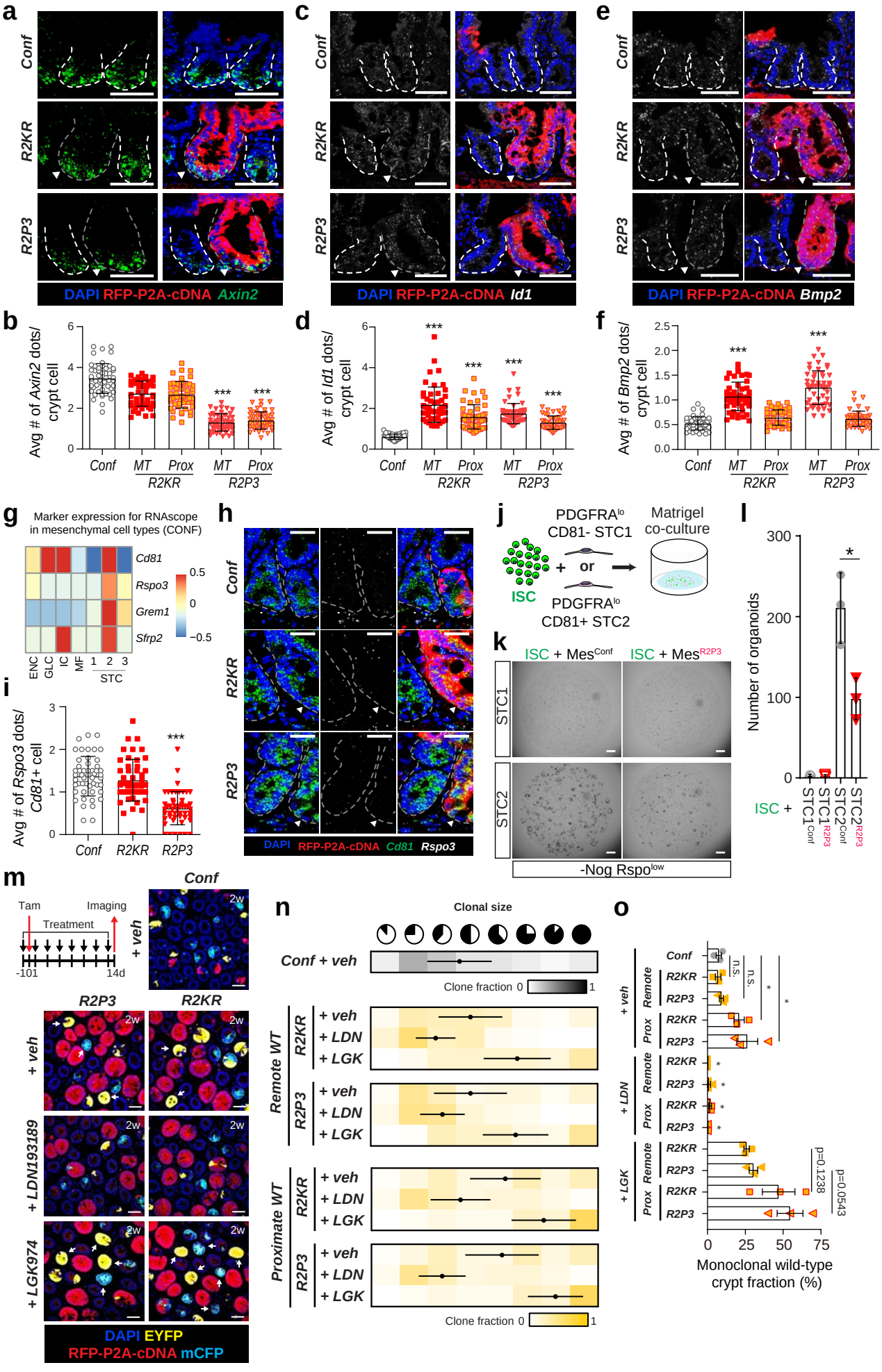
a
Conf
R2KR
R2P3
DAPI RFP-P2A-cDNA Axin2
b
Avg # of Axin2 dots/ crypt cell
Conf
MT
Prox
MT
Prox
R2KR
R2P3
c
DAPI RFP-P2A-cDNA Id1
d
Avg # of Id1 dots/ crypt cell
e
DAPI RFP-P2A-cDNA Bmp2
f
Avg # of Bmp2 dots/ crypt cell
g
Marker expression for RNAscope in mesenchymal cell types (CONF)
Cd81
Rspo3
Grem1
Sfrp2
ENC
GLC
IC
MF
STC
h
DAPI RFP-P2A-cDNA Cd81 Rspo3
i
Avg # of Rspo3 dots/ Cd81+ cell
j
PDGFRAlo CD81- STC1
+ or
PDGFRAlo CD81+ STC2
ISC
Matrigel co-culture
k
ISC + MesConf
ISC + MesR2P3
STC1
STC2
-Nog Rspolow
l
Number of organoids
ISC +
STC1Conf
STC1R2P3
STC2Conf
STC2R2P3
m
Tam
Imaging
Treatment
-101
14d
+ veh
+ LDN193189
+ LGK974
DAPI EYFP
RFP-P2A-cDNA mCFP
n
Clonal size
Conf + veh
Clone fraction 0
1
Remote WT
Proximate WT
+ LDN
+ LGK
o
Monoclonal wild-type crypt fraction (%)
p=0.1238
p=0.0543
n.s.

Figure 6. Functional validation of oncogene-driven niche remodeling

a-f, Representative *in situ* hybridization images and quantification of *Axin2* (**a** and **b**), *Id1* (**c** and **d**) and *Bmp2* (**e** and **f**) on sections of small intestine from *Villin-CreERT2;R26R-Confetti* or *Red2Onco* mice at 2w post-tamoxifen administration. Fixed mutant crypts are indicated by white arrowheads. Wild-type and mutant crypts are marked with a white and grey dashed outline, respectively. Conf: *R26R-Confetti*; R2KR: *Red2-Kras*^{G12D}; R2P3: *Red2-PIK3CA*^{H1047R}; MT: mutant crypts; Prox: proximate wild-type crypts. Data are presented as mean ± SD. N = 3 mice for each group. For each group, 50 crypts were analysed. p-values from ANOVA test: ***, p < 1e-4. Scale bar: 50 µm.

g, Heatmap showing expression of marker genes that were used to characterise STC2 population among mesenchymal cells. Color bar indicates averaged Z-scores of $\log_2$-transformed normalized UMIs over all cells within a given cell type in *Confetti* animals.

h, i, Representative multiplexed *in situ* hybridization images (**h**) and quantification (**i**) of *Rspo3* in *Cd81*+ cells on sections of small intestine from *Villin-CreERT2;R26R-Confetti* or *Red2Onco* mice at 2w post-tamoxifen administration. Fixed mutant crypts are indicated by white arrowheads. Crypts are marked with grey dashed outlines. Conf: *R26R-Confetti*; R2KR: *Red2-Kras*^{G12D}; R2P3: *Red2-PIK3CA*^{H1047R}. Data are presented as mean ± SD. N = 3 mice for each group. For each group, 50 crypt pairs were analysed. p-values from ANOVA test: ***, p < 1e-4. Scale bar: 25 µm.

j, Lgr5+ cells were sorted and cultured with either PDGFRA^{lo} CD81- STC1 cells or PDGFRA^{lo} CD81+ STC2 cells from *Confetti* or *Red2-PIK3CA*^{H1047R} intestine.

k, l, Representative bright-field images (**k**) and quantification (**l**) of intestinal organoids formed after 4 days of co-culturing. The number and size of organoids markedly reduced following co-culturing with STC2 cells from *Red2-PIK3CA*^{H1047R} intestine, compared to control. Mes^{Conf}: mesenchymal cells from *Confetti* mouse; Mes^{R2P3}: mesenchymal cells from *Red2-PIK3CA*^{H1047R} intestine. Scale bar: 500 µm.

m, Representative confocal images of whole mount small intestine from *Villin-CreERT2;R26R-Confetti* or *Red2Onco* mice at 2w post-tamoxifen administration. Specific drug (LDN193189: BMP type I receptor blocking agent; LGK974: Porcupine inhibitor) or vehicle was administered following the dosing regimen (Top left). Fixed (monoclonal) wild-type crypts are indicated by white arrows. Conf: *R26R-Confetti*; R2KR: *Red2-Kras*^{G12D}; R2P3: *Red2-PIK3CA*^{H1047R}. Scale bar: 50 µm.

n, Heat maps indicate the relative clone fractions of the indicated sizes (columns) at 2w after concomitant administration of indicated drug and tamoxifen (rows). Black dots denote mean ± SEM. N = 3 mice for each group. For each condition, >50 clones were scored. Remote WT: wild-type clones located in crypts separated by >3 crypt diameters from mutant crypts. Proximate WT: wild-type clones located in crypts neighboring fixed mutant crypts.

o, Fraction of monoclonal (YFP+) wild-type crypts remote from (Remote), or proximate to (Prox) mutant crypts in *Red2Onco* mice at 2w after concomitant administration of indicated drug and tamoxifen. Data are presented as mean ± SEM. N = 3 mice for each group. For each condition, >50 clones were scored. Grey circles: clones from *R26R-Confetti* control; Yellow symbols: remote wild-type clones from *Red2Onco* mice; Yellow symbols with red outline: proximate wild-type clones from *Red2Onco* mice.

Extended data figure 1

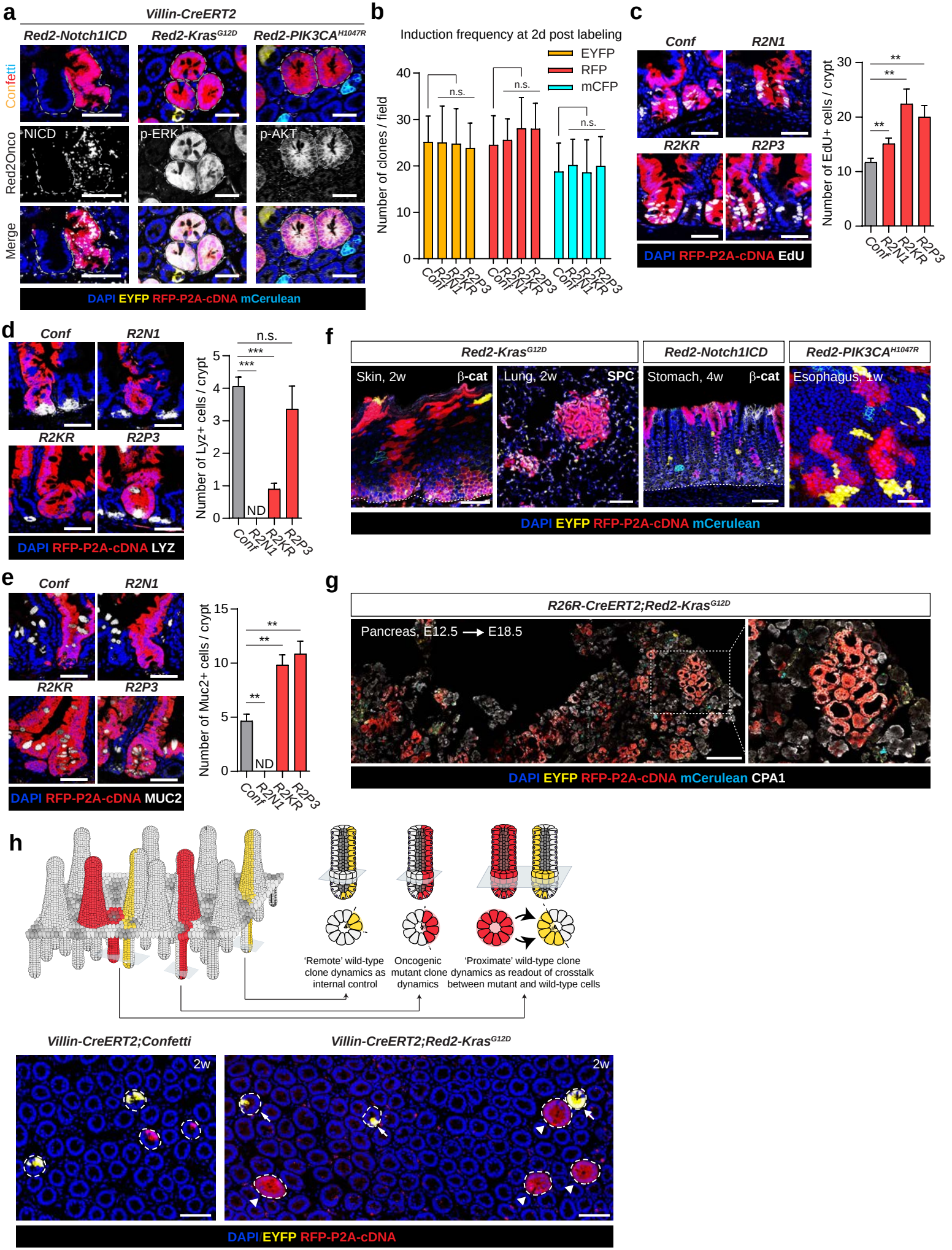

Extended Data Figure 1. Red2Onco system: an oncogene-associated multicolor reporter

a, Representative confocal images of mutant clones from sections (*Red2-Notch1ICD*) or whole mounts (*Red2-Kras^{G12D}* and *Red2-PIK3CA^{H1047R}*) of small intestine from *Villin-CreERT2;Red2Onco* mice at 2w post-tamoxifen administration. Staining for NICD, pErk and pAkt provides a functional readout of activated NOTCH1ICD, KRAS and PIK3CA respectively. Crypt borders are marked with a grey dashed outline. Scale bar: 50 μm.

b, Average clone numbers collected from a single field of image (0.15 mm^2) of whole mount small intestine from *Villin-CreERT2;R26R-Confetti* or *Red2Onco* mice at 2d post-tamoxifen administration. Data are presented as mean ± SD. *N* = 3 mice for each group. >10 images were analysed per mouse. Note the similar degree of induction between models, which enables comparative clonal analysis using the *R26R-Confetti* and *Red2Onco* mice. Conf: *R26R-Confetti*; R2N1: *Red2-Notch1ICD*; R2KR: *Red2-Kras^{G12D}*; R2P3: *Red2-PIK3CA^{H1047R}*. p-values from ANOVA test: n.s., statistically not significant (p > 0.1).

c, Representative confocal images and quantification of EdU+ proliferating crypt cells from sections of small intestine from *Villin-CreERT2;R26R-Confetti* or *Red2Onco* mice at 4w post-tamoxifen administration. Data are presented as mean ± SD. *N* = 5 mice for each group. For each mouse >100 crypts were analysed. p-values from ANOVA test: **, p < 0.01; ***, p < 1e-4. Scale bar: 50 μm.

d, Representative confocal images and quantification of LYZ+ Paneth cells from sections of small intestine from *Villin-CreERT2;R26R-Confetti* or *Red2Onco* mice at 4w post-tamoxifen administration. Data are presented as mean ± SD. *N* = 5 mice for each group. For each mouse, >100 clones were analysed. p-values from ANOVA test: **, p < 0.01; ***, p < 1e-4. Scale bar: 50 μm.

e, Representative confocal images and quantification of MUC2+ goblet cells from sections of small intestine from *Villin-CreERT2;R26R-Confetti* or *Red2Onco* mice at 4w post-tamoxifen administration. Data are presented as mean ± SD. *N* = 5 mice for each group. For each mouse, >100 clones were analysed. p-values from ANOVA test: **, p < 0.01; ***, p < 1e-4. Scale bar: 50 μm.

f, Representative confocal images of 100 μm-thick sections or whole mounts of tissues from adult *R26R-CreERT2; Red2Onco* mice (skin and stomach corpus), *Sftpc-CreERT2; Red2Onco* mice (lung) or *Krt5-CreERT2; Red2Onco* mice (esophagus) at 1w, 2w and 4w post-tamoxifen administration. The white dashed line indicates the epithelial lining. Scale bar: skin and esophagus: 50 μm; lung and stomach: 100 μm. β-catenin stained as a cell membrane marker. SPC marks lung alveolar type II cells in lung.

g, Representative confocal images of sectioned mouse embryonic pancreas tissue from the *R26R-CreERT2; Red2-Kras^{G12D}* model at embryonic day 18.5, 6d post-tamoxifen administration. Magnified panel to the right shows an example of acinar cell expansion in developing pancreas. Scale bar: 200 μm. CPA1 marks acinar cells in developing pancreas.

h, Schematic illustration of clonal events within the Red2Onco system (upper panel) and representative tile scan confocal images of clones from sections of small intestine from *Villin-CreERT2;R26R-Confetti* or *Red2-Kras^{G12D}* mice at 2w post-tamoxifen administration (lower panel). Proximate wild-type crypts and fixed mutant crypts are indicated by white arrows and arrowheads, respectively. Crypt borders are marked with a white dashed outline. Scale bar: 100 μm.

Extended data figure 2

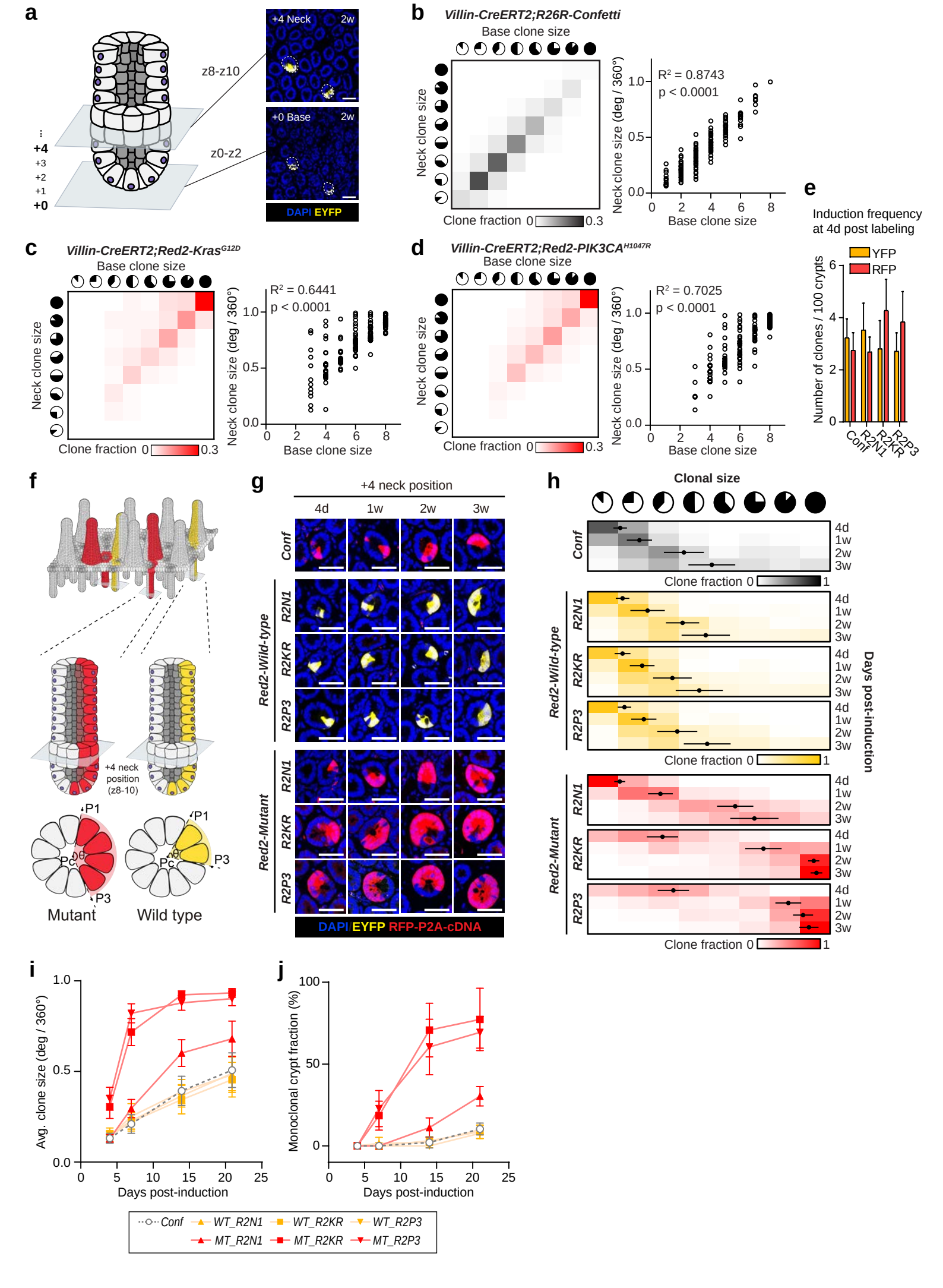

Extended Data Figure 2. Oncogenes drive non-neutral clone expansion in the mouse intestinal crypt

a, Representative confocal images of the base and neck of crypts. Crypt borders are marked with a white dashed outline. Scale bar: 100 μm.

b-d, Graph demonstrating strong correlation between clone size at the bottom (row +0) and neck (row +4) of a crypt from *Villin-CreERT2;R26R-Confetti* (2 weeks post-tamoxifen administration) or *Red2Onco* mice (1 week post-tamoxifen administration). Clone sizes at the crypt bottom are denoted as eighths of the crypt circumference: 1 indicates that a fraction of 1/8 of the crypt circumference is occupied by a single clone, etc. Clone sizes at the crypt neck are determined as the total circumferential angle spanned by the clone. As clone size determination at the crypt neck is considerably more reliable, we used neck quantification for our analysis. Scale bar: 50 μm. p-value determined by Pearson correlation. N = 3 mice for each group. *R26R-Confetti*: 211 clones. *Red2-Kras*^{G12D} :171 clones. *Red2-PIK3CA*^{H1047R} :143 clones.

e, Average number of clones per 100 crypts for whole mount small intestine from *Villin-CreERT2;R26R-Confetti* or *Red2Onco* mice at 4 d post-tamoxifen administration. Data are presented as mean ± SD. N = 3 mice for each group. >10 fields of images (2.41mm^2) were analysed per mouse. Conf: *R26R-Confetti*; R2N1: *Red2-Notch1ICD*; R2KR: *Red2-Kras*^{G12D}; R2P3: *Red2-PIK3CA*^{H1047R}.

f, Schematic illustration of mutant (RFP+) and wild-type (YFP+) clones in crypts which are remote from each other. Clone sizes are quantified by their angular span, θ, at row +4, as illustrated. P1 and P3 indicate the left and right ends, respectively, of the circular arc made by the clone and Pc indicates the center of the crypt.

g, Representative confocal images of clones in whole mount small intestine from *Villin-CreERT2; R26R-Confetti* or *Red2Onco* mice at 4d, 1w, 2w and 3w post-tamoxifen administration. Red2-Wild-type: remote YFP+ clones; Red2-Mutant: RFP+ clones. Conf: *R26R-Confetti*; R2N1: *Red2-Notch1ICD*; R2KR: *Red2-Kras*^{G12D}; R2P3: *Red2-PIK3CA*^{H1047R}. Scale bar: 50 μm.

h, Heat maps indicate the relative clone fractions of the indicated sizes (columns) at various time points post-induction (rows). Black dots denote mean ± SEM. N = 6 mice for each group and time point. For each condition, >50 clones were scored.

i, **j**, Average clone size (**i**) and percentage of monoclonal crypts (**j**) at different time points post-tamoxifen administration. Data are presented as mean ± SEM. N = 6 mice for each group. For each condition, >50 clones were scored. Grey circles and dashed line: *R26R-Confetti* control; yellow symbols and lines: remote wild-type (WT) clones in *Red2Onco* mice; red symbols and lines: mutant (MT) clones in *Red2Onco* mice.

Extended data figure 3

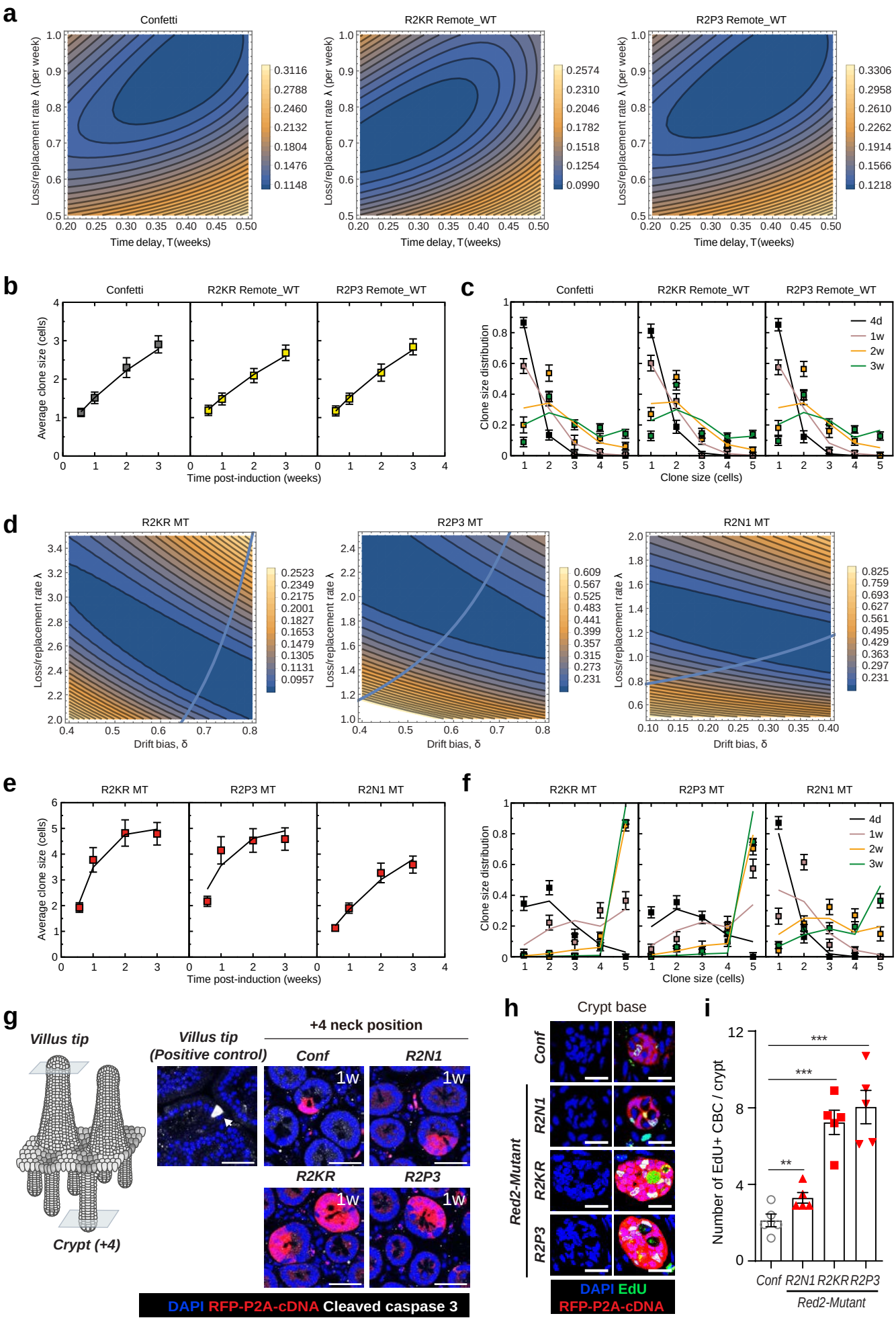

Extended Data Figure 3. Biophysical modeling of non-neutral clone expansion of mutant clones

a, Contour plots showing the mean-square differences between the neutral one-dimensional drift model and the YFP clone data from *Confetti* control animals (left) as well as wild-type (WT) crypts remote from mutant crypts in the R2KR (middle) and R2P3 (right) animals. The plots show a scan of the loss/replacement rate vs. a time delay between injection and clone induction. Confetti: *R26R-Confetti*; R2KR: *Red2-Kras*^{G12D}; R2P3: *Red2-PIK3CA*^{H1047R}.

b, Average clone size (defined in terms of effective cell number) as a function of time post-induction for the three models from (**a**). Points show data (mean ± SEM) and line shows model prediction. In each case, the total effective stem cell number is taken as $N=5$, so that an average clone size of, e.g., 2 corresponds to a circumferential angle of 360º x 2/5.

c, Distribution of clone sizes (defined in terms of effective cell number) at the different time points for the three models from (**a**). Lines indicate the clone size distribution defined in terms of effective stem cell number from the model prediction, and dots indicate experimental data from Extended Data Fig. 2.

d, Contour plots showing the mean-square differences between the biased one-dimensional drift model and the RFP mutant (MT) clone data from R2KR (left), R2P3 (middle) and R2N1 (right) animals. The plots show a scan of the loss/replacement rate λ vs. drift bias δ with a time delay of 0.29 weeks for R2KR, 0 weeks for R2P3 and 0.43 weeks for R2N1. The blue lines show the constraint $\lambda(1-\delta) = \lambda_{\mathrm{WT}}$, where λ_{WT} denotes the loss/replacement rate inferred from the Confetti control (for details, see Supplementary Thoery). R2KR: *Red2-Kras*^{G12D}; R2P3: *Red2-PIK3CA*^{H1047R}; R2N1: *Red2-Notch1ICD*.

e, Average clone size (defined in terms of effective cell number) as a function of time post-induction for the three models from (**d**). Points show data (mean ± SEM) and line shows model prediction. In each case, the total effective stem cell number is taken as $N=5$.

f, Distribution of clone sizes (defined in terms of effective cell number) at the different time points for the three models from (**d**). Lines indicate the clone size distribution defined in terms of effective stem cell number from the model prediction, and dots indicate experimental data from Extended Data Fig. 2.

g, Representative confocal images of cleaved caspase-3+ apoptotic cells in whole mount small intestine from *Villin-CreERT2;R26R-Confetti* or *Red2Onco* mice at 1w post-tamoxifen administration. A single cleaved caspase-3+ apoptotic cell in the villus tip is indicated by a white arrow as a positive control. Scale bar: 50 µm.

h, i, Representative confocal images (**h**) and quantification (**i**) of EdU+ proliferating crypt base columnar cells in whole mount small intestine from *Villin-CreERT2;R26R-Confetti* or *Red2Onco* mice at 2w post-tamoxifen administration. Data are presented as mean ± SEM. N = 5 mice for each group. For each mouse, >100 clones were analysed. p-values from ANOVA test: **, $p < 0.01$; ***, $p < 1e\text{-}4$. Scale bar: 25 µm.

Extended data figure 4

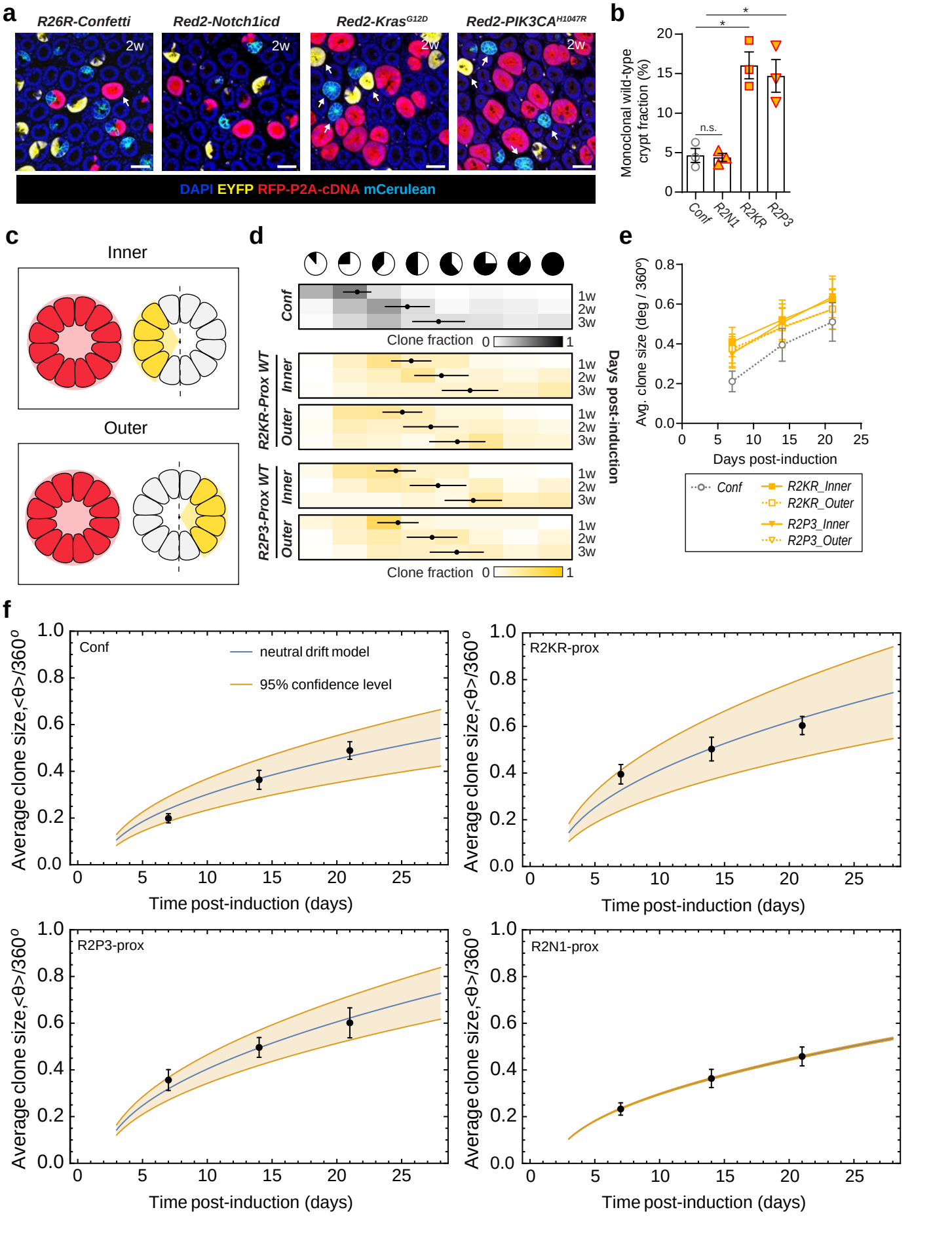

Extended Data Figure 4. Mutant crypts perturb clonal dynamics of wild-type cells in neighboring crypts

a, Representative confocal images of whole mount small intestine from *Villin-CreERT2;R26R-Confetti* or *Red2Onco* mice at 2w post-tamoxifen administration. Fixed (monoclonal) wild-type crypts are indicated by white arrows. Scale bar: 50 μm.

b, Percentage of monoclonal wild-type small intestinal crypts at 2w post-tamoxifen administration. Conf: *R26R-Confetti*; R2N1: *Red2-Notch1ICD*; R2KR: *Red2-Kras*^{G12D}; R2P3: *Red2-PIK3CA*^{H1047R}. Data are presented as mean ± SEM. N = 3 mice for each group. >10 images were analysed per mouse. p-values from ANOVA test: n.s., statistically not significant ($p > 0.1$); *, $p < 0.05$.

c, Schematic illustrating proximate wild-type clones in relation to fixed mutant crypts and defining inner vs. outer clones.

d, Heat maps indicate the relative clone fractions of the indicated sizes (columns) at various time points post-induction (rows). Black dots denote mean ± SEM. Note that here we regrouped the experimental data of proximate wild-type clones from Fig. 3c into inner and outer clones.

e, Average clone size of proximate (R2KR_In and R2KR_Out for *Red2-Kras*^{G12D}; R2P3_In and R2P3_Out for *Red2-PIK3CA*^{H1047R}) wild-type (YFP+) clones at different time points post-tamoxifen administration. Data are presented as mean ± SEM. N = 5 mice for each group and time point. For each condition, >30 clones were analysed. Grey circles and dashed line: *R26R-Confetti* control; yellow lines and yellow symbols: inner proximate wild-type clones from *Red2Onco* mice; yellow dashed lines with yellow symbols: outer proximate wild-type clones from *Red2Onco* mice.

f, Average clone size $\langle\theta\rangle/360^{o}$ of wild-type (YFP+) clones in crypts neighbouring crypts monoclonal for the given mutant together with Confetti control plotted as a function of time t post-induction. Points show data and blue line shows a fit to the square root dependence predicted by the neutral drift model (for details of the model fit, see Supplementary Theory). Orange line shows the 95% confidence interval for fit. N=6 mice for each group and time point. For each condition, >50 clones were scored. Data presented as mean ± SEM. Conf: *R26R-Confetti*; R2N1: *Red2-Notch1ICD*; R2KR: *Red2-Kras*^{G12D}; R2P3: *Red2-PIK3CA*^{H1047R}.

R26R-Confetti control data are reproduced from Extended Data Fig. 2 for comparison in heat maps (**d**) and graph (**e**).

Extended data figure 5

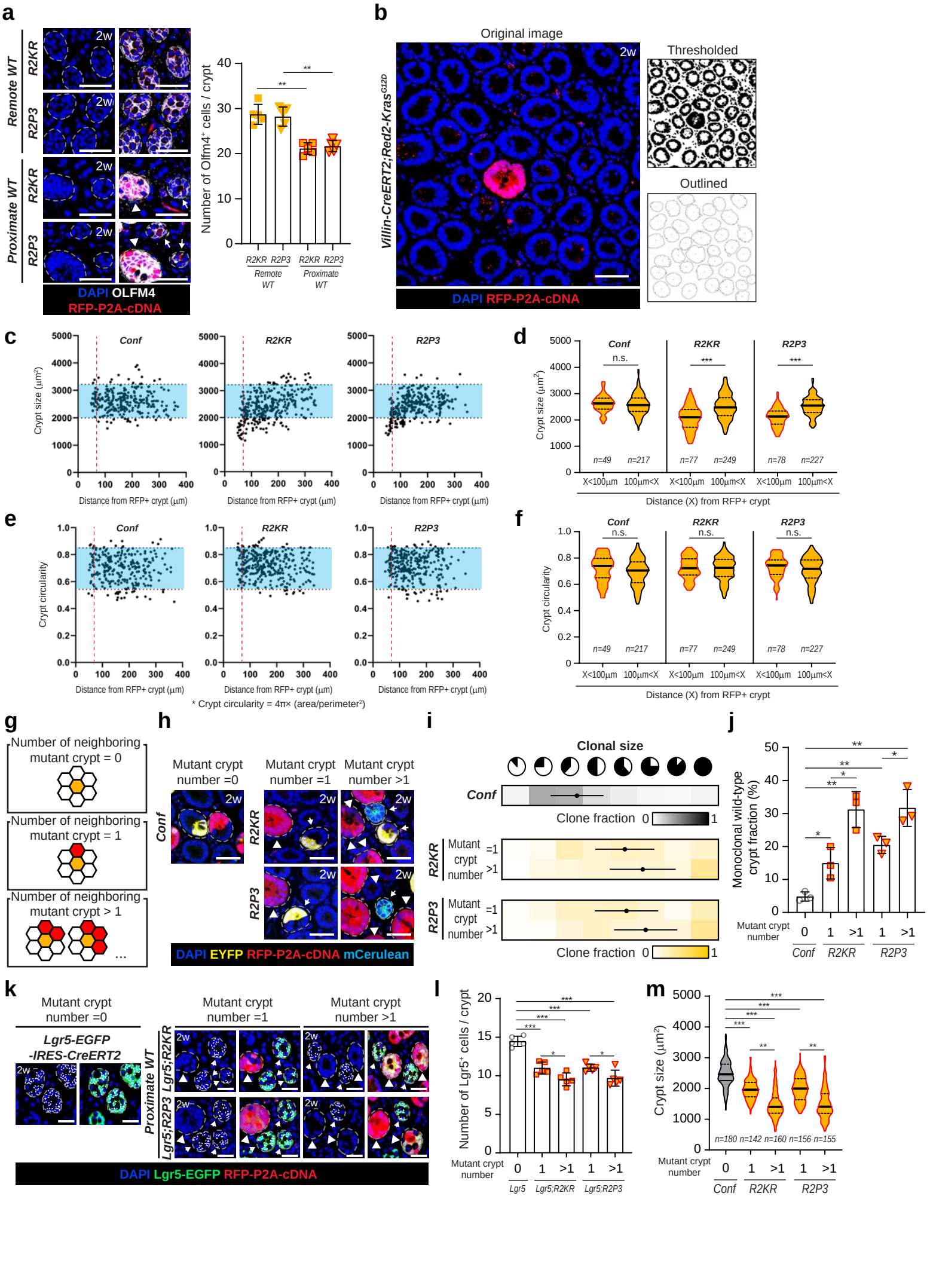

Extended Data Figure 5. Reduced effective stem cell number leads to accelerated drift dynamics of wild-type clones in crypts neighboring mutant crypts

a, Representative confocal images (left panel) and quantification (right panel) of intestinal stem cells in whole mount small intestine from *Lgr5-EGFP-IRES-CreERT2;Red2Onco* mice at 2w post-tamoxifen administration. Olfm4 staining shows a reduced number of stem cells in proximate wild-type crypts. Proximate wild-type crypts and fixed mutant crypts are indicated by white arrows and arrowheads, respectively. Crypt borders are marked with a grey dashed outline. Data are presented as mean ± SD. $N = 5$ mice for each group. For each mouse, >100 crypts were analysed. p-values from unpaired t-test: n.s., statistically not significant ($p > 0.1$); **, $p < 0.01$; ***, $p < 1e\text{-}4$. Scale bar: 50 µm.

b, Crypt size and circularity were quantified using ImageJ. An original image (left panel) was thresholded (upper right panel) and outlined (lower right panel) in order to measure each factor. The original image was collected from whole mount small intestine from the *Villin-CreERT2;Red2-Kras^{G12D}* model. Scale bar: 50 µm.

c, d, Dot (**c**) and violin (**d**) plots display the size of wild-type crypts in relation to distance from the nearest fixed mutant (RFP+) crypt. >200 crypts were analysed per model. In (**c**), the black dotted lines and blue shaded area indicate the 95% confidence interval of *R26R-Confetti* controls. The red dashed line indicates average distance between the center of a fixed mutant crypt and proximate neighboring crypts. In (**d**), data from (**c**) are regrouped and displayed as a violin plot. The *n* number for each group is shown. Conf: *R26R-Confetti*; R2KR: *Red2-Kras^{G12D}*; R2P3: *Red2-PIK3CA^{H1047R}*.

e, f, Dot (**e**) and violin (**f**) plots display the circularity (perfect circle = 1; <1 represents departure from circularity) of wild-type crypts in relation to distance from the nearest fixed mutant (RFP+) crypt. >200 crypts were analysed per model. In (**e**), the black dotted lines and blue shaded area indicate the 95% confidence interval of control *R26R-Confetti* samples. The red dashed line indicates average distance between the center of a fixed mutant crypt and its proximate neighboring crypt. In (**f**), data from (**e**) are regrouped and displayed as a violin plot. The *n* number for each group is shown. Conf: *R26R-Confetti*; R2KR: *Red2-Kras^{G12D}*; R2P3: *Red2-PIK3CA^{H1047R}*.

g, h, Schematic illustration (**g**) and representative confocal images (**h**) of clones in whole mount small intestine from *Villin-CreERT2;R26R-Confetti* or *Red2Onco* mice at 2w post-tamoxifen administration. Proximate wild-type crypts and fixed mutant crypts are indicated by white arrows and arrowheads, respectively. Crypt borders are marked by dashed grey outlines. Conf: *R26R-Confetti*; R2KR: *Red2-Kras^{G12D}*; R2P3: *Red2-PIK3CA^{H1047R}*. Scale bar: 50 µm.

i, Heat maps indicate the relative clone fractions of the indicated sizes (columns) at 2w post-induction (rows). Black dots denote mean ± SEM. N = 3 mice for each group and time point. For each condition, >50 clones were scored.

j, Percentage of monoclonal crypts of proximate wild-type (YFP+) clones at 2w post-tamoxifen administration. Data are presented as mean ± SD. N = 3 mice for each group. For each condition, >50 clones were scored. p-values from unpaired t-test: *, $p < 0.05$; **, $p < 0.01$. Conf: *R26R-Confetti*; R2KR: *Red2-Kras^{G12D}*; R2P3: *Red2-PIK3CA^{H1047R}*.

k, l, confocal images (**k**) and quantification (**l**) of EGFP+ (Lgr5+) stem cells in whole mount small intestine from *Lgr5-EGFP-IRES-CreERT2;Red2Onco* mice at 2w post-tamoxifen administration. Proximate wild-type crypts and fixed mutant crypts are indicated by white arrows and arrowheads, respectively. Crypt borders are marked by dashed grey outlines. EGFP+ cells in wild-type crypts are outlined with a white dashed line. Data are presented as mean ± SD. N = 5 mice for each group. For each mouse, >100 crypts were analysed. p-values from unpaired t-test: *, $p < 0.05$; **, $p < 0.01$., ***, $p < 1e\text{-}4$. Scale bar: 50 µm.

m, Violin plots display the size of wild-type crypts in relation to the multiplicity of neighboring mutant crypts. >100 crypts were analysed per model. The n number for each group is shown. p-values from unpaired t-test: **, $p < 0.01$., ***, $p < 1e\text{-}4$. Conf: *R26R-Confetti*; R2KR: *Red2-Kras^{G12D}*; R2P3: *Red2-PIK3CA^{H1047R}*.

Extended data figure 6

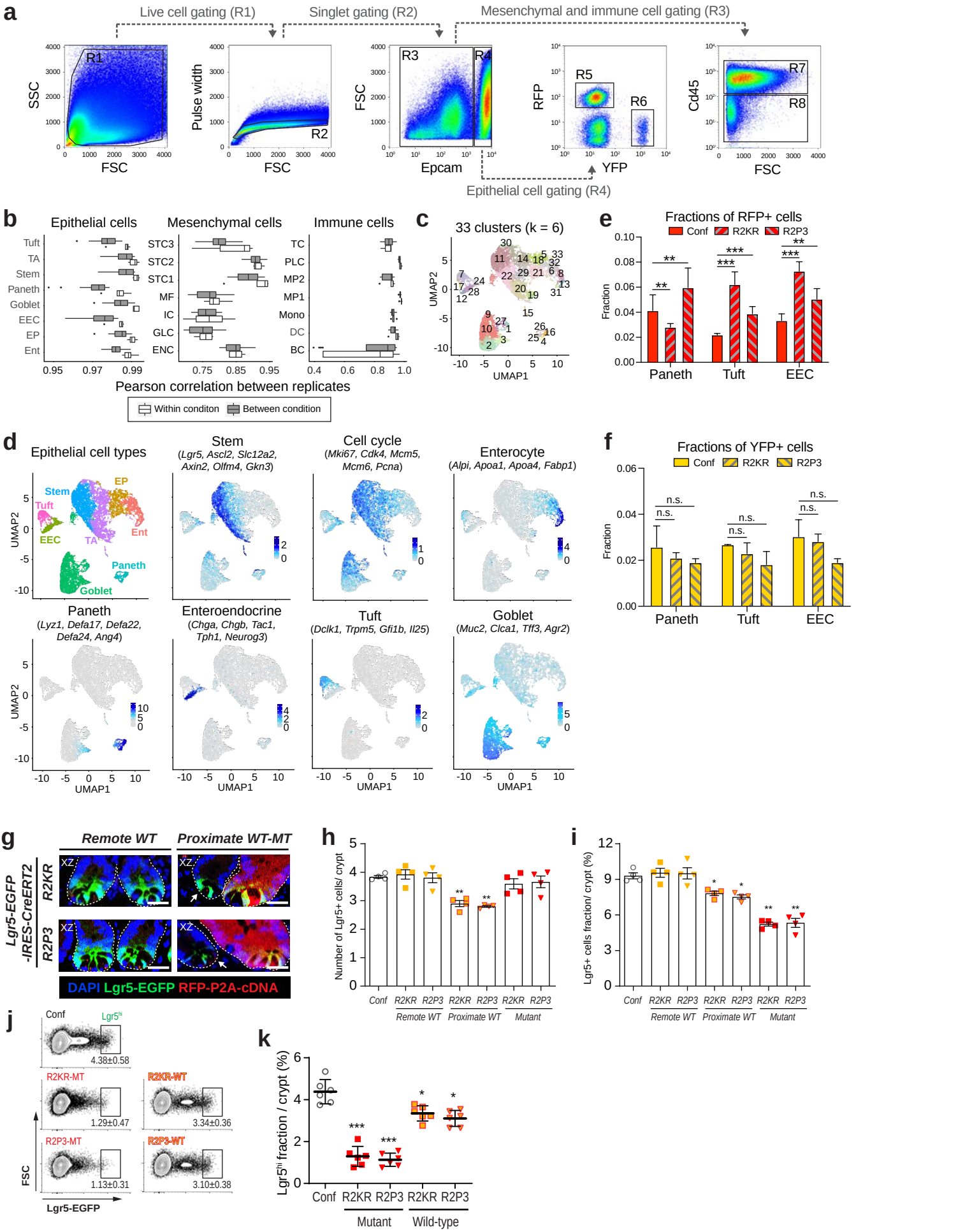

Extended Data Figure 6. Comparative single-cell transcriptomic analysis identifies oncogene-driven changes in signaling pathways

a, Sorting strategy to isolate and separate epithelial cells from intestinal crypts, stromal cells and immune cells from the *Confetti*, *Red2-Kras*^{G12D}, and *Red2-PIK3CA*^{H1047R} models by FACS. R1: gating for the live cell population. R2: singlet gating. R3: gating for mesenchymal and immune cells (EPCAM-). R4: gating for intestinal epithelial cells (EPCAM+). R5: gating for mutant epithelial cells (RFP+). R6: gating for wild-type epithelial cells (YFP+). R7: gating for immune cells (CD45+). R8: gating for mesenchymal cells (CD45-). For each biological replicate, all cells sorted from the gates R5, R6, R7 and R8 were pooled together and used to make one library.

b, Box and whisker plots showing the distributions of Pearson correlation coefficients in average expression profiles (average $\log_2$(UMI+1)) for cells in each cell type of epithelial, mesenchymal, and immune populations across all pairs of mice from the same conditions (white box plot) and between different conditions (grey box plot). Black bar, median; box edges, 25th and 75th percentiles.

c, 33 clusters of epithelial cells from intestinal crypts detected by Louvain algorithm. k means k nearest-neighbor (kNN) value. High kNN value decreases clustering resolution, resulting in smaller number of clusters.

d, UMAPs showing the distribution of averaged expression of a few known marker genes for a particular cell type or state (as indicated above each plot). These marker genes were collected from Extended Data Figure 1 of a previous study[41]. Color bars denote averaged normalised log2(UMI+1). UMAP on the upper left shows distinct epithelial cell types from the intestinal crypts from Fig. 4b for comparison.

e, Fractions of cell types other than those in Fig. 4d for mutant epithelial cells in the *Red2Onco* mice and the *Confetti* control. The fraction of each cell type was calculated by taking the number of that cell type normalised by the total number of cells for each animal. Conf: *R26R-Confetti*; R2KR: *Red2-Kras*^{G12D}; R2P3: *Red2-PIK3CA*^{H1047R}. Data are presented as mean ± SEM. p-values from likelihood ratio test: *, $p < 0.05$; **, $p < 0.01$; ***, $p <$ 1e-4; n.s., statistically not significant ($p > 0.05$).

f, Fractions of cell types other than those in Fig. 4e for wild-type epithelial cells in the *Red2Onco* mice and the *Confetti* control. The fraction of each cell type was calculated by taking the number of that cell type normalised by the total number of cells for each animal. Conf: *R26R-Confetti*; R2KR: *Red2-Kras*^{G12D}; R2P3: *Red2-PIK3CA*^{H1047R}. Data are presented as mean ± SEM. p-values from likelihood ratio test: n.s., statistically not significant ($p > 0.05$).

g, Representative confocal images of EGFP+ (Lgr5+) stem cells in small intestine from *Lgr5-EGFP-IRES-CreERT2;Red2Onco* mice at 2w post-tamoxifen administration (clonal dosage: 0.2 mg/20 g body weight). Wild-type (WT) crypts proximate to mutant (MT) crypts are indicated by white arrows. Crypts are marked with a white dashed outline. R2KR: *Red2-Kras*^{G12D}; R2P3: *Red2-PIK3CA*^{H1047R}. Scale bar: 25 μm.

h, i, Quantification of EGFP+ (Lgr5+) stem cell number (**h**) or fraction (**i**) from sectioned small intestine from Lgr5-EGFP-IRES-CreERT2;Red2Onco mice at two weeks (2w) post-tamoxifen administration. Conf: *R26R-Confetti*; R2KR: *Red2-Kras*^{G12D}; R2P3: *Red2-PIK3CA*^{H1047R}. Remote WT: wild-type clones located in crypts separated by >3 crypt diameters from mutant crypts. Proximate WT: wild-type clones located in crypts neighboring fixed (monoclonal) mutant crypts. Data are presented as mean ± SEM. N = 4 mice for each group. For each mouse, >100 crypts were analysed. p-values from unpaired t-test: *, $p < 0.05$; **, $p < 0.01$.

j, k, FACS plots (**j**) and quantification (**k**) of EGFP^{hi} stem cell fractions in small intestine from *Lgr5-EGFP-IRES-CreERT2;Red2Onco* mice at 2w post-tamoxifen administration (mosaic dosage: 4 mg/20 g body weight). MT: mutant; WT: wild-type; Conf: *R26R-Confetti*; R2KR: *Red2-Kras*^{G12D}; R2P3: *Red2-PIK3CA*^{H1047R}. Data are presented as mean ± SD. *N* = 6 mice for each group. p-values from ANOVA test: *, $p < 0.05$; ***, $p <$ 1e-4.

Extended data figure 7

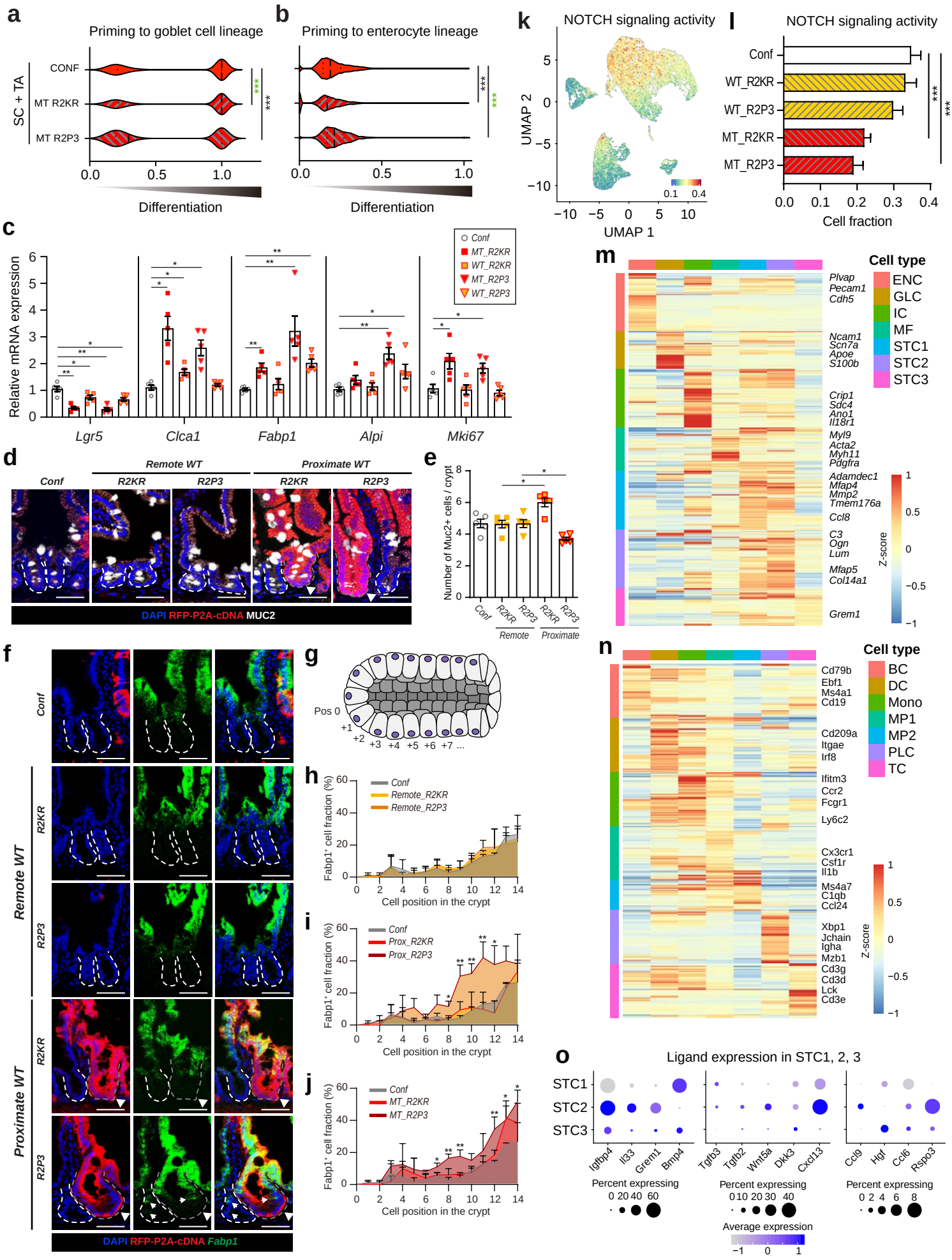

Extended Data Figure 7. Mutant crypt induces primed differentiation

a, b, Priming scores of mutant (MT; RFP+) stem cells (SC) and TA cells toward goblet (**a**) and enterocyte (**b**) lineages in the *Red2Onco* mice and the *Confetti* control. Higher priming scores were observed in the mutant cells from both *Red2Onco* mice compared to those of the *Confetti* control. 25th and 75th percentile values are denoted in thin black dotted lines and 50th percentile with thick black dotted line. p-values from Kolmogorov–Smirnov test: ***, p < 1e-4. Green asterisk: higher in *Red2Onco* mice compared to the *Confetti* control. Black asterisk: lower in *Red2Onco* mice compared to the *Confetti* control.

c, qPCR analysis of lineage markers (*Lgr5*: ISC; *Clca1*: Goblet cell; *Fabp1* and *Alpi*: Enterocyte; *Mki67*: proliferating cell) using sorted RFP+ or YFP+ cells from *Villin-CreERT2;R26R-Confetti* or *Red2Onco* mice at 2w post-tamoxifen administration. Conf: *R26R-Confetti*; R2KR: *Red2-Kras^{G12D}*; R2P3: *Red2-PIK3CA^{H1047R}*. Data are presented as mean SEM. N = 5 mice for each group. p-values from unpaired t-test: *, p < 0.05, **, p < 0.01.

d, e, Representative confocal images (**d**) and quantification (**e**) of MUC2+ goblet cells from sections of small intestine from *Villin-CreERT2;R26R-Confetti* or *Red2Onco* mice at two weeks (2w) post-tamoxifen administration. Wild-type and mutant crypts are marked with a white and grey dashed outline, respectively. Remote WT: wild-type clones located in crypts separated by >3 crypt diameters from mutant crypts. Proximate WT: wild-type clones located in crypts neighboring fixed (monoclonal) mutant crypts. Conf: *R26R-Confetti*; R2KR: *Red2-Kras^{G12D}*; R2P3: *Red2-PIK3CA^{H1047R}*. Data are presented as mean ± SEM. N = 5 mice for each group. For each mouse, >100 crypts were analysed. p-values from ANOVA test: *, p < 0.05. Scale bar: 50 µm.

f, RNA in situ hybridization of enterocyte lineage marker, *Fabp1* on sections of small intestine from *Villin-CreERT2;R26R-Confetti* or *Red2Onco* mice at 2w post-tamoxifen administration. *Fabp1* positive cells in lower crypts (below +8) are marked by white arrow. Fixed mutant crypts are indicated by white arrowheads. Wild-type and mutant crypts are marked with a white and grey dashed outline, respectively. Remote WT: wild-type clones located in crypts separated by >3 crypt diameters from mutant crypts. Proximate WT: wild-type clones located in crypts neighboring fixed (monoclonal) mutant crypts. Scale bar: 50 µm.

g, Schematic illustration of cellular localization along the crypt axis. Position 0 (Pos 0) indicates the cell at the crypt base.

h-j, Quantification of *Fabp1* expression in remote wild-type crypts (Remote_R2KR or Remote_R2P3) (**h**), proximate wild-type crypts (Prox_R2KR or Prox_R2P3) (**i**) and mutant crypts (MT_R2KR or MT_R2P3) (**j**) along the crypt axis. Conf: *R26R-Confetti*; R2KR: *Red2-Kras^{G12D}*; R2P3: *Red2-PIK3CA^{H1047R}*. Data are presented as mean ± SD. N = 3 mice for each group. For each group, 50 crypts were analysed. p-values from unpaired t-test: *, p < 0.05; **, p < 0.01.

k, UMAP showing the distribution of gene set enrichment scores for the NOTCH pathway. As shown in the UMAP, NOTCH pathway scores are enriched in stem cells and absorptive cells. Color bar indicates the gene set enrichment scores.

l, Fractions of "active" cells with high gene set enrichment scores for the NOTCH pathway in mutant (MT) and wild-type (WT) epithelial cells from the *Red2Onco* mice and the *Confetti* control. The fraction of NOTCH pathway active cells decreased in mutant cells of both *Red2Onco* mice relative to the *Confetti* control, implying that the NOTCH pathway is unlikely to be involved in the crosstalk between mutant and wild-type cells in the *Red2Onco* mice. Conf: *R26R-Confetti*; R2KR: *Red2-Kras^{G12D}*; R2P3: *Red2-PIK3CA^{H1047R}*. Data are presented as mean ± SEM. p-values from likelihood ratio test: ***, p < 1e-4.

m, n, Heatmaps representing differential expression (DE) patterns for distinct cell types of mesenchymal (**m**) and immune (**n**) populations from the intestinal crypts of *Red2Onco* mice and *Confetti* control. The DE genes for each cell type are the top 300 genes or less with FDR < 0.05 from a pairwise t-test. Colored panels on the left indicate differentially expressed genes for cell types as per the legend. ENC: endothelial cell; GLC: glial cell; IC: intestitial cell of Cajal; MF: myofibroblast; STC1, STC2, STC3: stromal cell 1, 2, 3; BC: B-cell; DC: dendritic cell; Mono: monocyte; MP1, 2: macrophage 1, 2; PLC: plasma cell; TC: T-cell. Key marker genes are indicated on the right for each cell type. Color bar indicates averaged Z-scores of $\log_2$-transformed normalized UMIs over all cells within a given cell type.

o, Dot plots of expression of secreted factors in stromal cell clusters for *Confetti* mice. The size of the dot denotes the percentage of cells of one cell type expressing a given gene, while the color denotes the average expression of the gene across all cells of that cell type.

Extended data figure 8

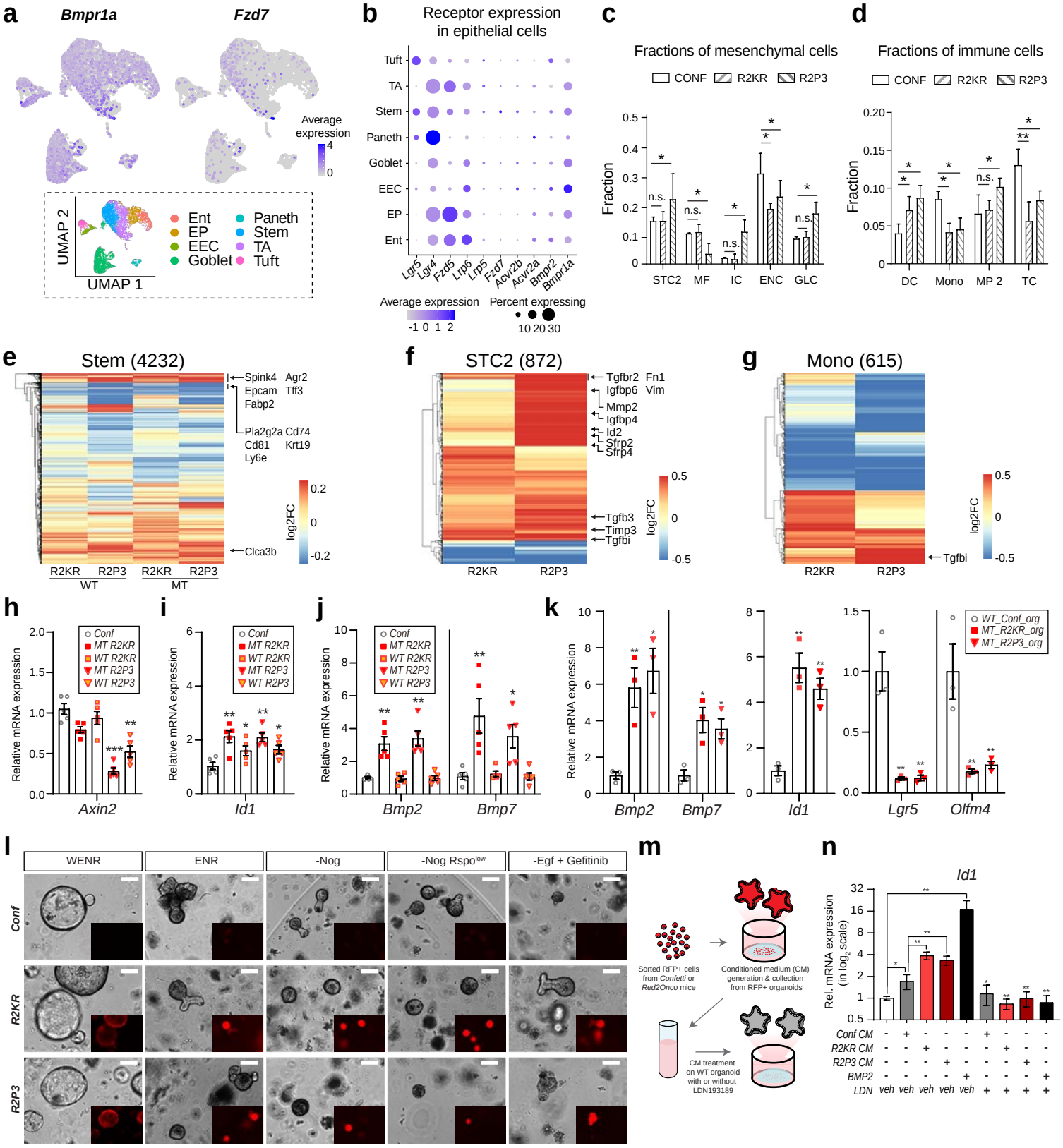

Extended Data Figure 8. Mutant epithelial cells secrete functional BMP ligands

a, UMAPs showing expression of *Bmpr1a* (left) and *Fzd7* (right), representative receptors for the BMP and WNT pathways, respectively, in epithelial cells. The color bar indicates log_2-transformed normalized UMIs. The UMAP in the inset details the clustering of the different epithelial cell types from Fig. 4b for comparison.

b, Dot plots showing expression of receptors that are upstream of BMP and WNT pathways for each epithelial cell type found in intestinal crypts. Tuft: tuft cell; TA: transit-amplifying cell; Stem: stem cell; Paneth: Paneth cell; Goblet: goblet cell; EEC: enteroendocrine cell; EP: enterocyte progenitor; Ent: enterocyte. The size of the dot denotes the percentage of cells of one cell type expressing a given gene, while the color denotes the average expression of the gene across all cells of that cell type.

c, d, Fractions of cell types for mesenchymal (**c**) and immune (**d**) cells in the *Red2Onco* models and *Confetti* control. The fraction of each cell type was calculated by taking the number of that cell type normalised by the total number of cells for each animal. Data are presented as mean ± SEM. p-values from likelihood ratio test: *, $p < 0.05$; **, $p < 0.01$; n.s., statistically not significant ($p > 0.05$). STC1, STC3, BC, MP1 and PLC do not show significant fractional change (data not shown).

e-g, Heatmaps representing differential gene expression for stem cell (**e**), STC2 (**f**), and monocyte (**g**) in *Red2Onco* mice compared to the *Confetti* control. Number within parenthesis: number of differentially expressed genes. Stem: stem cell, STC2: stromal cell 2, Mono: monocyte.

h-j, qPCR analysis of WNT target gene, *Axin2* (**h**), BMP target gene, *Id1* (**i**) and BMP ligands (*Bmp2* and *Bmp7*) (**j**) using sorted RFP+ or YFP+ cells from *Villin-CreERT2;R26R-Confetti* or *Red2Onco* mice at 2w post-tamoxifen administration (4mg/ 20g body weight, mosaic dosage). Conf: *R26R-Confetti*; R2KR: *Red2-Kras*^{G12D}; R2P3: *Red2-PIK3CA*^{H1047R}. Data are presented as mean ± SEM. N = 5 mice for each group. p-values from unpaired t-test: *, $p < 0.05$, **, $p < 0.01$, ***, $p < 1e\text{-}4$.

k, qPCR analysis of intestinal stem cell markers (*Lgr5* and *Olfm4*), BMP ligands (*Bmp2* and *Bmp7*) and BMP target genes (*Id1*) using wild-type and mutant organoids cultured in ENR medium. Conf: *R26R-Confetti*; R2KR: *Red2-Kras*^{G12D}; R2P3: *Red2-PIK3CA*^{H1047R}. Data are presented as mean ± SEM. Quantification graphs show data from 3 independent experiments. p-values from unpaired t-test: *, $p < 0.05$; **, $p < 0.01$.

l, Bright-field images of intestinal organoids from *Villin-CreERT2;R26R-Confetti* or *Red2Onco* mice at 1 month post-tamoxifen administration. Organoids were initially formed and treated with the following conditions: WENR: Wnt3a CM, Egf, Noggin and R-spondin1 CM; ENR: Egf, Noggin, and R-spondin1 CM; -Nog: withdrawal of Noggin from the ENR medium; -Nog Rspo^{low}: withdrawal of Noggin and lowered R-spondin1 CM concentration (10% to 1%) from the ENR medium; -Egf + Gefetinib: withdrawal of Egf and addition of Gefitinib (EGFR inhibitor). Note that organoids from both mutants are sensitive to growth factor withdrawal while they are resistant to Egf removal. Images were collected 5 days after treatment. Insets show RFP expression of the mutant organoids. Scale bar: 100 µm.

m, Experimental setup for (**n**). Sorted RFP+ cells from *Villin-CreERT2;R26R-Confetti* or *Red2Onco* mice were seeded in Matrigel supplemented with WENR medium to establish RFP+ organoids. The organoids were then cultured in -Nog medium for 7 more days to generate conditioned medium (CM). Wild-type organoids were treated with or without CM, BMP2 or BMP type I receptor inhibitor, LDN193189, to analyse the effect of the CM on BMP signalling activation.

n, qPCR analysis of BMP target genes (*Id1*) using wild-type organoids after the CM treatment. BMP type I receptor inhibitor, LDN193189-treated group are compared to corresponding vehicle-treated group to directly confirm whether the effect is dependent on BMP ligands. Data are presented as mean ± SD. Quantification graphs show data from 3 independent experiments. p-values from unpaired t-test: *, $p < 0.05$, **, $p < 0.01$.

Extended data figure 9

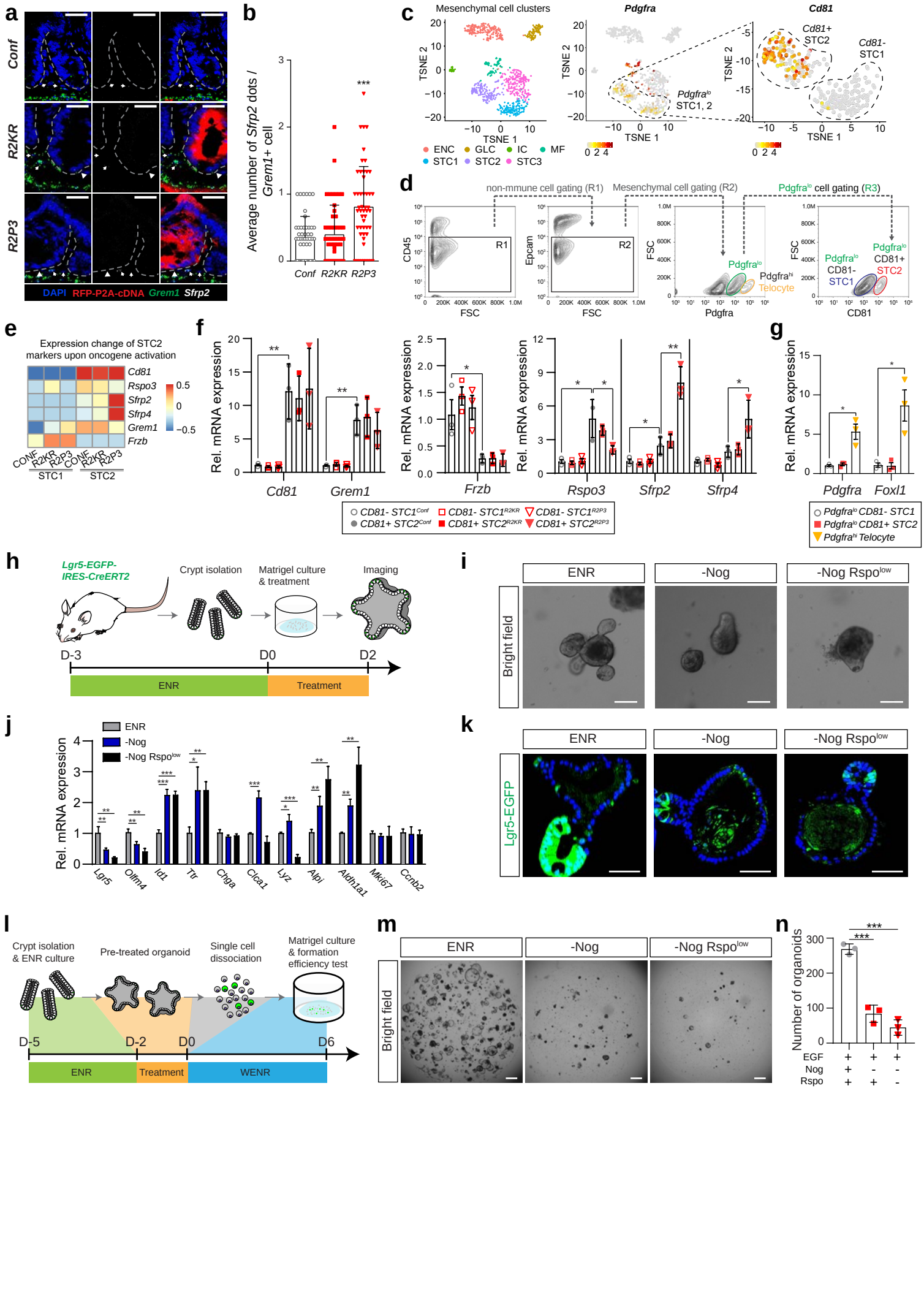

Extended Data Figure 9. Mutant clones drive niche remodeling

a, b, Representative multiplexed *in situ* hybridization images (**a**) and quantification (**b**) of *Sfrp2* in *Grem1*+ cells on sections of small intestine from *Villin-CreERT2;R26R-Confetti* or *Red2Onco* mice at 2w post-tamoxifen administration. Fixed mutant crypts are indicated by white arrowheads. Crypts are marked with grey dashed outlines. *Grem1* positive STC2 cells are indicated by white arrow. Conf: *R26R-Confetti*; R2KR: *Red2-Kras*^{G12D}; R2P3: *Red2-PIK3CA*^{H1047R}. Data are presented as mean ± SD. N = 3 mice for each group. For each group, 50 crypt pairs were analysed. p-values from ANOVA test: ***, p < 1e-4. Scale bar: 25 µm.

c, UMAP showing the distributions of all mesenchymal cells (Left). Projection of *Pdgfra* transcript density onto the UMAP (middle). *Pdgfra*^{lo} cell clusters are magnified (right). Projection of *Cd81* transcript density onto the *Pdgfra*^{lo} cell clusters shows that *Cd81* distinguishes robustly STC2 from STC1 cells within *Pdgfra*^{lo} cell clusters.

d, Sorting strategy to isolate STC2 from intestinal mesenchymal cells by FACS. R1: gating for non-immune cells (CD45-). R2: gating for mesenchymal cells (EPCAM-). R3: gating for PDGFRA^{lo} population. Telocytes: gating for PDGFRA^{hi} population; STC1: gating for CD81- cells from PDGFRA^{lo} population (R3); STC2: gating for CD81+ cells from PDGFRA^{lo} population (R3).

e, Heatmap showing differential expression of marker genes and secreted factors from STC1 and STC2 from three conditions (CONF: *R26R-Confetti*; R2KR: *Red2-Kras*^{G12D}; R2P3: *Red2-PIK3CA*^{H1047R}). Color bar indicates averaged Z-scores of $\log_2$-transformed normalized UMIs over all cells within a given cell type and condition.

f, qPCR analysis of STC2 marker (*Cd81* and *Grem1*), STC1 marker (*Frzb*) and secreted WNT modulators (*Rspo3*, *Sfrp2* and *Sfrp4*) using sorted CD45- EPCAM- PDGFRA^{lo} CD81- cells (STC1) or CD45- EPCAM- PDGFRA^{lo} CD81+ cells (STC2) from *Villin-CreERT2;R26R-Confetti* or *Red2Onco* mice at 2w post-tamoxifen administration. Conf: *R26R-Confetti*; R2KR: *Red2-Kras*^{G12D}; R2P3: *Red2-PIK3CA*^{H1047R}. Data are presented as mean ± SD. N = 3 mice for each group. p-values from unpaired t-test: *, p < 0.05, **, p < 0.01.

g, qPCR analysis of Telocyte markers (*Pdgfra* and *Foxl1*) using sorted STC1, STC2 and Telocytes. Data are presented as mean ± SEM. N = 3 mice for each group. p-values from unpaired t-test: *, p < 0.05.

h, Experimental setup for (**i**)–(**k**). Organoids were initially formed in full medium (ENR) for 3 days, then treated with the following conditions: -Nog: withdrawal of Noggin from the ENR culture medium; -Nog Rspo^{low}: withdrawal of Noggin and lowered R-spondin concentration (10% to 1%) from the ENR medium. Samples were collected 2 days after treatment.

i, Bright-field images of intestinal organoids after 2 days of treatment. The number and size of crypt-like budding structures are reduced in treated organoids. Scale bar: 50 µm.

j, qPCR analysis of lineage markers (*Lgr5* and *Olfm4*: ISC; *Chga*: Enteroendocrine; *Clca1*: Goblet; *Lyz*: Paneth; *Alpi* and *Aldh1a1*: Enterocyte; *Mki67* and *Ccnb2*: proliferation) and BMP target genes (*Id1* and *Ttr*) following treatment. Data are presented as mean ± SD. Quantification graphs show data from 3 independent experiments. p-values from unpaired t-test: *, p < 0.05, **, p < 0.01; ***, p < 1e-4.

k, Representative GFP fluorescence images of Lgr5-EGFP organoids show that the number of Lgr5+ cells decreases following treatments. Scale bar: 100 µm.

l, Experimental setup for (**m**)–(**n**). Organoids were formed and treated as described in panel (**h**). After treatment, organoids were dissociated and 2×10^4 single cells were seeded in Matrigel supplemented with WENR medium (ENR + Wnt conditioned medium) to quantify the organoid formation efficiency.

m, n, Bright-field images (**m**) and quantification (**n**) of intestinal organoids after 6 days of culture in WENR medium. The number of organoids markedly reduced following treatment. Data in (**n**) are presented as mean ± SD. Quantification graphs show data from 3 independent experiments. p-values from unpaired t-test: ***, p < 1e-4. Scale bar: 500 µm.

Extended data figure 10

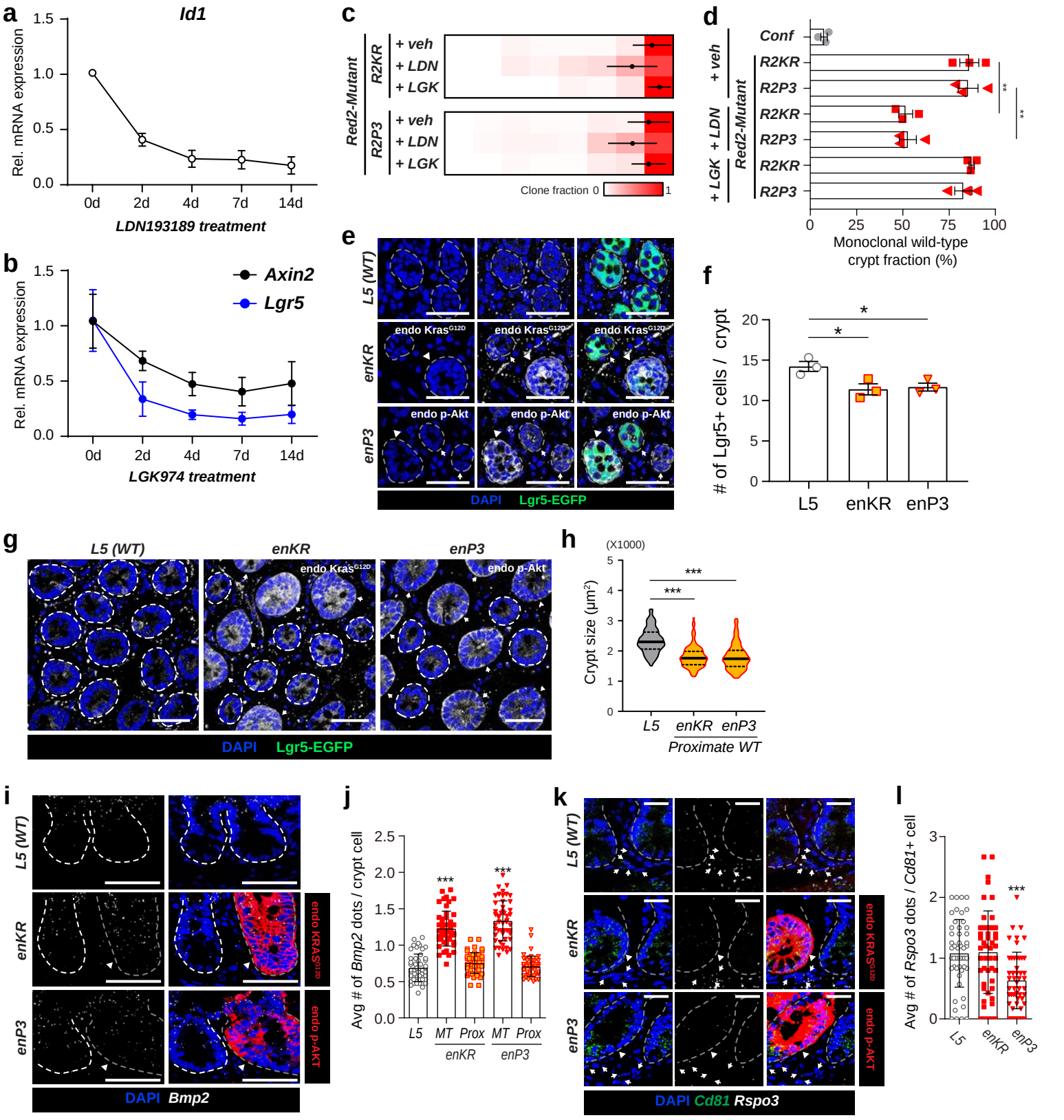

Extended Data Figure 10. Functional validation of oncogene-driven niche remodeling

a, b, qPCR analysis of BMP target gene (*Id1*) (**a**), WNT target gene (*Axin2*) and intestinal stem cell marker (Lgr5) (**b**) using intestinal crypts isolated from mice administered with specific drug (LDN193189: BMP type I receptor blocking agent; LGK974: Porcupine inhibitor). Data are presented as mean ± SD. N = 3 mice for each group.

c, Heat maps indicate the relative clone fractions of the indicated sizes (columns) at 2w after concomitant administration of indicated drug and tamoxifen (rows). Black dots denote mean ± SEM. N = 3 mice for each group. For each condition, >50 clones were scored. R2KR: *Red2-Kras*^{G12D}; R2P3: *Red2-PIK3CA*^{H1047R}

d, Fraction of monoclonal (RFP+) mutant crypts in *Red2Onco* mice at 2w after concomitant administration of indicated drug and tamoxifen. Data are presented as mean ± SEM. N = 3 mice for each group. For each condition, >50 clones were scored. Grey circles: clones from *R26R-Confetti* control; Red symbols: mutant clones from *Red2Onco* mice

e, f, Representative confocal images (**e**) and quantification (**f**) of EGFP+ (Lgr5+) stem cells in whole mount small intestine from *Lgr5-EGFP-IRES-CreERT2* control (L5), *Lgr5-EGFP-IRES-CreERT2;LSL-Kras*^{G12D} (enKR) or *Pik3ca*$^{Lat\text{-}H1047R}$ (enP3) mice at 2w post-tamoxifen administration. Proximate wild-type crypts and mutant crypts are indicated by white arrows and arrowheads, respectively. Crypt borders are marked by dashed grey outlines. White: immunostaining for mutant KRAS^{G12D} in enKR, or p-AKT in enP3. Data are presented as mean ± SD. N = 3 mice for each group. For each mouse, >100 crypts were analysed. p-values from unpaired t-test: *, $p < 0.05$. Scale bar: 50 µm.

g, Representative confocal images of whole mount small intestine from *Lgr5-EGFP-IRES-CreERT2;LSL-Kras*^{G12D} (enKR) or *Pik3ca*$^{Lat\text{-}H1047R}$ (enP3) mice at 2w post-tamoxifen administration. Mutant crypts are indicated by white arrows. Proximate wild-type crypts are marked by dashed white outlines. White: immunostaining for mutant KRAS^{G12D} in enKR, or p-AKT in enP3. Scale bar: 50 µm.

h, Violin plot displaying the size distributions of proximate wild-type crypts in *Lgr5-EGFP-IRES-CreERT2;LSL-Kras*^{G12D} (enKR) or *Pik3ca*$^{Lat\text{-}H1047R}$ (enP3) mice at 2w post-tamoxifen administration. 100 crypts were analysed per group. p-values from unpaired t-test: ***, $p < 1e\text{-}4$.

i, j, RNA in situ hybridization (**i**) and quantification (**j**) of *Bmp2* on sections of small intestine from *Lgr5-EGFP-IRES-CreERT2;LSL-Kras*^{G12D} (enKR) or *Pik3ca*$^{Lat\text{-}H1047R}$ (enP3) mice at 2w post-tamoxifen administration. Mutant crypts are indicated by white arrowheads. Wild-type and mutant crypts are marked with a white and grey dashed outline, respectively. MT: mutant crypts; Prox: proximate wild-type crypts. Red: immunostaining for mutant KRAS^{G12D} in enKR, or p-AKT in enP3. Data are presented as mean ± SD. N = 3 mice for each group. For each group, 50 crypts were analysed. p-values from ANOVA test: ***, $p < 1e\text{-}4$. Scale bar: 50 µm.

k, l, Representative multiplexed *in situ* hybridization images (**k**) and quantification (**l**) of *Rspo3* in *Cd81*+ cells on sections of small intestine from *Lgr5-EGFP-IRES-CreERT2;LSL-Kras*^{G12D} (enKR) or *Pik3ca*$^{Lat\text{-}H1047R}$ (enP3) mice at 2w post-tamoxifen administration. Mutant crypts are indicated by white arrowheads. *Cd81* positive STC2 cells are indicated by white arrow. Crypts are marked with grey dashed outlines. Red: immunostaining for mutant KRAS^{G12D} in enKR, or p-AKT in enP3. Data are presented as mean ± SD. N = 3 mice for each group. For each group, 50 crypt pairs were analysed. p-values from ANOVA test: ***, $p < 1e\text{-}4$. Scale bar: 25 µm.